CHARACTERIZATION of HIGH STRAIN RATE BEHAVIOR of TAC/CNTs/SIC CMCs PREPARED by SPARK PLASMA SINTERING

by

Qiaoyun Xie

BS, Nanjing University of Technology, 2007

MS, Nanjing University of Technology, 2010

Submitted to the Graduate Faculty of

Swanson School of Engineering in partial fulfillment

of the requirements for the degree of

Doctor of Philosophy

University of Pittsburgh

2015

UNIVERSITY OF PITTSBURGH

SWANSON SCHOOL OF ENGINEERING

This dissertation was presented

by

Qiaoyun Xie

It was defended on

March 23, 2015

and approved by

Hong Koo Kim, Ph.D, Professor
Department of Electrical and Computer Engineering

Albert CF To, Ph.D, Associate Professor
Department of Mechanical Engineering and Materials Science

William S Slaughter, Ph.D, Associate Professor
Department of Mechanical Engineering and Materials Science

Dr. Jorg M Wiezorek, Ph.D, Professor
Department of Mechanical Engineering and Materials Science

Dissertation Director: Sylvanus N Wosu, Ph.D, Associate Professor
Department of Mechanical Engineering and Materials Science

CHARACTERIZATION OF HIGH STRAIN RATE BEHAVIOR OF TAC/CNTS/SIC CMCS PREPARED BY SPARK PLASMA SINTERING

Qiaoyun Xie, Ph.D

University of Pittsburgh, 2015

Silicon carbide (SiC) ceramics are one of the best candidates for high temperature structural applications. However, due to the inherent drawbacks of hardness, porosity, and brittleness for ceramic materials and the specific application environment involving exposure to oxidation fuels, or aero heating, reinforcements of carbon nanotubes (CNTs) and tantalum carbide (TaC) are considered to improve the overall material properties; of particular interest are the fracture toughness, energy absorption ability, and oxidation resistance. Conventional fabrication of CNTs reinforced ceramic matrix composites (CMCs) involves hot pressing techniques, which are characterized by high pressure and a long processing time, but can destroy CNTs. The current research utilizes a rapid consolidation technique of spark plasma sintering (SPS) which densifies the ceramics at a relatively lower temperature and a much shorter holding time with improved bonding quality and finer microstructure.

A two-stage SPS of TaC and/or CNTs reinforced SiC CMCs was developed to investigate the sintering parameters, such as pressure, heating rate, and temperature on the densification behavior and mechanical properties. The oxidation mechanism of CNTs/SiC ceramics, as well as the TaC additives effect on the thermal oxidation resistance of the TaC/CNTs/SiC systems were examined up to 1500 $^\circ$C. The influences of sample thickness,

impact energy (loading rates), temperature and moisture on the compressive dynamic response of TaC and/or CNTs reinforced SiC CMCs were conducted by a penetration split Hopkinson pressure bar (P-SHPB). The fracture mechanics of TaC/CNTs/SiC CMCs were studied both quasi-statically and dynamically by Vickers indentation and a three point bending test on the modified SHPB with a pulse shaper. The possible toughening mechanisms provided by the CNTs reinforcement were directly observed. Wave propagation in SHPB was validated numerically and the prediction of damage evolution was carried out through user-defined material subroutine VUMAT in ABAQUS/explicit. The above investigations provide new perspectives which could impact a wide range of understandings and applications for the TaC/CNTs/SiC CMCs.

TABLE OF CONTENTS

LIST OF TABLES

LIST OF FIGURES

xii

ACKNOWLEDGEMENTS

The completion of this dissertation would not have been accomplished without the support and guidance of my advisor, Dr. Sylvanus N Wosu. I am very grateful to Dr. Wosu, who has consistently provided the opportunities and drives for this research work, expanded my critical thinking skills, and opened my mind to new ideas, which I would not have acoomplished otherwise. I would also like to take this opportunity to thank those who support my research experiments and give me helpful academic advices.

I am very thankful to the members of CalNano Company for guiding me during the process of Spark Plasma Sintering, which played a key role in my research. I would like to thank Dr. Gleeson and his student Wei Zhao, for helping with the thermal gravimetric analysis. I would also like to thank Dr. Deardo, and his student Bin Ma, for helping with the preparation of specimens. Many thanks to my friends Siqi Chen and Jian Feng for supporting and encouraging me all the way through finishing my Ph.D dissertation.

Sincere thanks to my family— you are all the reason for which I am fighting.

1.0   INTRODUCTION

1.1   MOTIVATION AND BACKGROUND

Composite materials offer engineers an ability to create a limitless number of new material systems which have unique properties that cannot be obtained using a single monolithic material. By definition, composite materials consist of two or more constituents, and have characteristics derived from the individual ones. The constituent that is continuous and which is often, but not always, present in the greater quantity in the composite is referred as the matrix, while the second or the remaining constituents are regarded as the reinforcements, as they enhance the properties of the matrix [1]. By combining the high temperature ceramic matrix with good toughness, oxidation, and thermal shock resistance reinforcements, there is a high potential for creating new CMCs with high performance applicability in aerospace. This research work will focus on developing SiC CMCs according to the intended application for space systems.

The increasing growth of CMCs in aerospace and defense sectors has provided a large impetus for the development of high temperature structural CMCs applied in aeroengines, gas turbines, and other aircraft parts in the temperature range from 1100 ^{o}C to above 1500 ^{o}C [2]. Since the late 1960s, the world of high performance structural materials has focused primarily on SiC and Si_3N_4 as the materials of choice, due to their high temperature strength, low coefficient of thermal expansion, and high thermal conductivity. Moreover, SiC and Si_3N_4 possess the

highest oxidation resistance among the non-oxide structural ceramics. Si_3N_4 exhibits excellent strength and creep resistance at elevated operating temperatures, but may be limited by its vulnerability to oxidation at temperatures exceeding 1000 ^{o}C, while SiC has a high temperature of decomposition approximate to 2500 ^{o}C, and possesses high thermal conductivity and good thermal shock resistance [3]. There are more than 200 materials with melting temperatures over 2000 ^{o}C, including SiC, refractory metals (Hf, Nb, Ir, Re, Ta, W), oxides (HfO_2, ZrO_2, UO_2, ThO_2), and a variety of transition metal carbides, nitrides, and borides, as well as other compounds [4]. For the real aerospace engineering application, the melting temperature is only one of the many properties used in the materials selection process. A potentially high performance ceramic material, to withstand high temperatures, should possess the following combined factors in determining the optimal materials: 1) Oxidation resistance, 2) Fracture toughness, 3) Thermal-mechanical fatigue resistance, 4) Thermal shock resistance, 5) Energy absorption ability, 6) Light weight, 7) Fabricability, and 8) Cost.

As the applications of CMCs involve exposure to oxidation fuels or aero heating, non-oxide materials have a tendency to be oxidized, forming some solid, liquid, or gaseous reaction products. It seems that the oxides are a reasonable choice for use in the oxidizing environment. However, such materials have poor thermal shock resistance and low thermal conductivity. The borides and carbides of group IV-V metals such as Tantalum, Niobium, and Titanium have high hardness, high melting points and good corrosion resistance [5]. These compounds and their composites are particularly used to increase the high temperature strength and the resistance to creep and fatigue for high temperature application [6-7]. Tantalum carbide is given particular attention because it has the highest melting point (3800 ^{o}C) among the binary compounds and a relatively low thermal expansion coefficient (4.1e-6/K), which is close to that of SiC (4.0e-6/K).

Most importantly, silicon based ceramics were found to be less porous in tantalum-containing composites [8]. Thus, TaC shows great promise as an additive to SiC CMCs, with the purpose of improving the oxidation resistance property.

SiC is a strong covalent compound and may be either crystalline or amorphous in structure. Because of this type of electronic bonding, SiC CMCs tend to fracture before undergoing plastic deformation, often resulting in a low tensile strength and poor materials toughness. Moreover, SiC has microscopic pores in its structure which could act as stress concentrators, further decreasing the toughness and strength of the composites [9]. Since SiC CMCs are hard, porous, and brittle, their applications are limited due to the lack of suitable reinforcement to mitigate these shortcomings. Carbon Nanotubes (CNTs), first observed under an electron microscope by Sumio Iijima in 1991 [10], have received close scrutiny in vast research areas, which include nanoscale reinforcements in composites in order to improve their mechanical, thermal, and even electrical properties. Basically, there are two types of CNTs: single-walled carbon nanotubes (SWNTs) and multi-walled carbon nanotubes (MWNTs). SWNTs exhibit semiconducting or metallic behavior depending on their chiralities [11]. MWNTs consist of two or more concentric cylindrical shells of graphene sheets coaxially arranged around a central hollow core, and held together with van der Waals forces between adjacent layers, where each layer has different chiralities. The morphology and properties of MWNTs are similar to those of SWNTs, but MWNTs have a much better and improved resistance to chemicals and thermal shock. Also, MWNTs are much less entangled and easier to process, which makes them more widely considered for mechanical improvement and other applications as reinforcement. CNTs improve the fracture toughness of the composites through a range of toughening mechanisms, such as the CNTs pull out, crack bridging, and crack

deflection. Although the focus of research work in CNTs based composites has mostly been on polymer composites, the exceptional resilience of CNTs can be a desirable reinforcement in ceramic composites [12-14].

Therefore, the combination of the characteristics of excellent fracture toughness are improved by CNTs and good oxidation resistance as enhanced by TaC with the intrinsic advances of SiC ceramic, such as high temperature stability, high corrosion resistance, and their being light weight, makes TaC/CNTs/SiC CMCs very attractive as functional and structural materials for application in aerospace systems. For the successful development of TaC/CNTs/SiC CMCs, two key challenges must be met during the fabrication [15].

First, the CNTs must be processed in such a way as to ensure a homogeneous dispersion to the matrix and also an appropriate degree of interfacial bonding. It is important that the individual CNTs are distributed uniformly throughout the matrix, and well separated from each other. In this case, each CNT is loaded over a maximum interfacial area and can contribute directly to the mechanical properties and toughening mechanisms. Unlike carbon fibers, however, CNTs tend to form bundles due to van der waals forces, and are very hard to separate individually. This agglomeration is extremely undesirable, especially in ceramic matrices, as they can act as defects leading to stress concentration and premature failure. The primary way of combating this is to modify CNTs by using dispersants or acid treatment to make them more stable in the solvent or compatible with the matrix, and then mix them with the ceramic powers by using high shear mixer, ultrasonic probes, or ball mills [16].

Second, to obtain a high degree of matrix densification without damaging the CNTs is another challenging issue. For conventional sintering techniques, which are characterized by the requirement of extended holding time at high temperature and pressure, CNTs are reported as

4

being damaged [17-18]. Spark plasma sintering (SPS) is a new consolidation technique for ceramics that uses high pulsed direct current and uniaxial pressure to densify the materials. Rapid heating and cooling rates with a low holding time, usually within a few minutes, to densify ceramics makes SPS an interesting consolidation technique. SPS also provides a means of precious modification for the kinetics of densification, reactions and grain growth that are involved in an entire sintering cycle [19]. SPS has been applied with success to a wide range of ceramics (oxides, nitrides, carbides, and composites) [20-22]. However, limited work was found on the parametric study for CNTs reinforced SiC ceramic composites. The motivation of this research work is to lay a fundamental foundation for the assessment of TaC/CNTs/SiC CMCs fabricated by SPS. The composites would be investigated for their densification behavior, microstructure, fracture toughness, and oxidation resistance in order to obtain a more sophisticated knowledge of SPS on the manufacturing of nanotube reinforced CMCs.

Dynamic loading is one of the concerns for composite materials used in aerospace applications where the high velocity impact, ballistic, and shock impact are more likely to cause structural damage which could therefore reduce the strength and life of the composites. Available experimental and theoretical studies have demonstrated that most of the impacts which induce inelastic deformations occur at high strain rates. Although the high strain rate behavior has been extensively studied for many materials, such as metals, ceramics, and polymers [23-27], the contribution of CNTs to the high strain rate characteristics under high temperature is still poorly understood. Therefore, correlating the material behavior with varying high strain rate, temperature, and impact loading conditions is of great interest [28]. Generally, strain rates above 10^2 s^{-1} are classified as high strain rates, and the split Hopkinson pressure bar (SHPB) is among one of the most common methods for testing the mechanical properties of various materials in

the strain rate range of 10^2-10^4 s^{-1}. Compared to the drop weight or the conventional ballistic impact tests, which do provide high strain rate loading and deal with energy absorption in composites, SHPB examines the effects of stress wave propagation, which is a source of damage initiation. Furthermore, in the cases where projectile penetration have been considered, the composites' energy absorption during the penetration process and the projectile's velocity, contact force, and duration of impact are difficult to measure. SHPB testing could eliminate these restrictions [29].

Significant efforts have been made to model the failure and damage propagation of composite materials for high strain rate dynamic impact loading. Since the composite structure doesn't completely lose its loading carrying capacity when the failure occurs at a materials point before it eventually fails, it is important to qualify the damage through a progressive failure model. The use of appropriate user-defined material models provides a good way of modeling the impact damage, and controlling the extent of damage, energy absorption, stiffness reduction and the final dynamic structural behavior. Presently, the simulation of dynamic impact on composites by SHPB, as well as the prediction of resulting degradation in strength, has not been matured to be employed by designers. Therefore, another motivation of this research work is to validate the one-dimensional stress wave propagation in SHPB and examine the user-defined material model for the prediction of damage initiation and propagation.

1.2   RESEARCH GOALS AND OBJECTIVES

The primary goal of this proposed research is to develop and characterize a new hybrid high performance composite material using a ceramic matrix, with particular application to

aerospace turbine and energy combustion systems. Properties such as light weight, good toughness, high temperature stability, high temperature oxidation resistance, thermal shock resistance, a good energy absorption capacity, and long life serviceability are desirable for such applications. TaC/CNTs/SiC CMCs can potentially be the high temperature performance structural composites that meet these demands. The specific objectives of this study are the following:

(1) Understand the effects of processing parameters, such as heating rates, sintering temperature, and pressure during SPS on the microstructural and mechanical properties of the TaC/CNTs/SiC CMCs. Study the densification behavior of TaC, CNTs, sintering aids, and ceramic powder mixtures, and reveal how the stability of the CNTs is affected by the electric field and high temperature.

(2) Identify the effect of TaC on the oxidation behavior of the composites and gain a better understanding of how the TaC additives help to resist the SiC CMCs from oxidation.

(3) Investigate the dynamic behavior of TaC/CNTs/SiC CMCs under different impact energy, temperature and moisture conditions, and understand the impact energy absorption mechanism and the failure modes in order to obtain a comprehensive knowledge of the dynamic response of this new hybrid system.

(4) Examine the fracture toughness of the composites and identify the toughening mechanisms of CNTs in CMCs. Develop a better understanding of the mechanics of fracture of ceramic composites in impact from quasi-static to dynamic, as well as the possibility of toughening with CNTs reinforced silicon carbide ceramics.

(5) Validate the one-dimensional wave propagation in SHPB and examine the user-defined material model for the prediction of damage initiation and propagation.

1.3   FRAMEWORK AND TASKS

1.3.1   Spark plasma sintering of TaC and/or CNTs reinforced SiC CMCs

To obtain the SiC CMCs with high performance, the powder mixtures of reinforcements and ceramic matrix, as well as the sintering aids, are homogeneously blended by ultrasonic agitation. SPS will be utilized to consolidate the TaC/CNTs/SiC and CNTs/SiC powders. Sintering parameters should be carefully designed to maintain the fine microstructure of the composites. Due to the low self-diffusion coefficient, B_4C is applied to aid the sintering process. Microstructures, densification behavior, and materials properties of SiC CMCs will be examined. It is expected that both the CNTs and B_4C would enhance diffusion and suppress grain growth of the composites.

1.3.2   The effect of TaC reinforcement on the oxidation of CNTs/SiC CMCs

The oxidation resistance of SiC in the CMCs is attributed to the growth of a protective silicon dioxide (SiO_2) glassy film which covers the interior oxide layer. When expose to air, high temperatures, or high pressure, high velocity combustion gases can volatilize the SiO_2, which leaves the silicon based ceramic exposed to form additional SiO_2 and then after volatilization, building a cycle that results in surface recession [30]. The purpose of this chapter is to describe how the TaC additives influence the CNTs/SiC CMCs oxidation behavior. A comparison group of CNTs/SiC CMCs without TaC will be made to undergo the same oxidation process. Structural quality of CNTs, weight changes of bulk specimen and microstructure of oxidized layers are examined.

1.3.3 Dynamic response of TaC/CNTs/SiC CMCs under high strain rate loading with elevated temperatures or moist environment

The penetration Split Hopkinson Pressure Bar (P-SHPB) will be employed to carry out the high strain rate dynamic impact test. The effects of sample thickness, impact energy (loading rates), temperature, and moisture on the compressive dynamic response of TaC/CNTs/SiC CMCs are studied. Dynamic material properties in terms of ultimate stress, ultimate strain, strain rate, compressive modulus, energy absorption, and particle velocity are investigated. Damage patterns induced by the dynamic indentation, and fragmentation size correlation with strain rate, are studied.

1.3.4 Dynamic fracture toughness of TaC/CNTs/SiC CMCs

CNTs hold a great promise as reinforcements in advanced materials, especially for the improved fracture toughness. Toughness in CMCs is typically achieved by a weak fiber/matrix interface coupling that permits debonding and sliding of the fibers within the matrix [31]. This chapter will employ Vickers indentation to measure the static fracture toughness on the polished surface of ceramic samples, SEM to directly observe the crack propagation after indentation, and SHPB to determine the dynamic fracture toughness within the ceramic samples subjected to impact in a three-point bending configuration.

1.3.5 Numerical and experimental analysis of SHPB

The impact events of laminated composites under dynamic loading are studied both experimentally and numerically. A 3-D model of SHPB will be developed and a parametric stress pulse taken as the impact loading onto the impact surface of the incident bar. Through the powerful user-defined materials subroutine interface VUMAT, the Hashin failure constitutive model is implemented within ABAQUS/Explicit. The application of progressive damage in the VUMAT subroutine is related to the material stiffness degradation. Contributions of this chapter will serve as verification of wave propagation in SHPB and prediction of the damage evolution by user defined material properties. Future work will be directed on the development of an appropriate material model for the TaC/CNTs/SiC CMCs to predict damage initiation and propagation under P-SHPB loading.

1.4   LITERATURE REVIEW

1.4.1   SPS of CNTs reinforced CMCs

In practice, sintering is the control of both densification and grain growth. Densification is the act of reducing porosity in a sample, thereby making it more dense. Grain growth is the process of grain boundary motion and Ostwald ripening to increase the average grain size. The mechanical properties of the sintered product benefit a great deal from both a high relative density and a small grain size. Therefore, being able to control these factors during processing is of high technical importance. To obtain the high performance material with high density and fine

grains, influences needing to be taken into account involve: powder characteristics (morphology, dimension of the grains, purity), processing parameters (temperature, heating rate, pressure, dwell time) and atmosphere (vacuum, oxidizing or inert) [32].

SPS is one of the powder consolidation methods, with simultaneously applied pressure and pulsed DC current. Using a DC pulse as the electrical current, spark plasma, spark impact press, joule heating, and an electrical field diffusion effect are created. The powders are directly fed into the graphite die, and then DC current is passed through the die to promote the sinterization, and pressure is loaded by the punchers to enhance the densification. Compared to conventionally hot pressing sintering, SPS is characterized by a fast heating rate, as high as 1000 ^{o}C/min, and a short dwelling time from 5-20 minutes, making it possible to sinter nanometric powders to full densification with little grain growth.

The sintering mechanism of covalent SiC based ceramic is different from that of ionic one due to the low diffusion of atoms and the high energy of grain boundaries. For this reason, sintering additives and pressure are needed to aid the sintering process. In solid-phase sintering, the temperature of the thermal treatment is slightly above two-thirds of the melting point which easily results in exaggerated grain growth. B_4C is a promising sintering aid applied by many researchers [33- 37]. In the case of sintering of TaC and SiC CMCs, B_4C helps to reduce the grain boundary energy and react with Si, Ta forming carbide ceramics, diboride ceramics and free carbon to cover the ceramic particle surfaces [38]. Recent emergences of CNTs as reinforcements are also reported to have the effect of suppressing grain growth and keeping a nanosize structure [5, 39-40].

Earlier studies on SPS of CNTs reinforced ceramics have been carried out in AL-CNT systems. Zhan et al. [41- 43] fabricated SWCNTs reinforced alumina composites with 0, 5.7, 10

and 15 vol.% SWNTs by SPS sintered at the temperatures of 1150 and 1200 ^{o}C for just 3 minutes, and found that the relative density reached over 98%. Sun et al. [44] consolidated their SWCNT-Al powders with 0.1 wt.% of CNTs by SPS under 1300 ^{o}C, 50 MPa for 5 minutes, and reported a fracture toughness improvement from 3.7 to 4.9 MPa·m$^{1/2}$. With the increasing need for high performance materials in aerospace, SPS has been conducted on high temperature ceramic composites sintering. Balazsi [45] compared the sintering methods of SPS and HIP for Si$_3$N$_4$ reinforced with 6 wt.% MWNTs, and revealed that higher density and better mechanical properties were achieved by SPS with the sintering parameter of 1500 ^{o}C, 3 minutes and 50 MPa. Bakshi et al. [5] studied the effect of pressure on the microstructure and mechanical properties of TaC-4 wt.% CNT ceramics by SPS in an Argon atmosphere at 1850 ^{o}C with the heating rate of 200°C/min for 10 minutes. They concluded that 100 MPa led to the increase of relative density from 89% to 95% while 255 MPa would damage the CNTs. Yadhukulakrishnan et al. [46] manufactured ZrB$_2$ reinforced with 10-40 vol.% SiC and 4-6 vol.% MWNTs using SPS under 1900 ^{o}C, 70 MPa, and 15 minutes, achieving a near-full densification (>99% relative density).

It is generally accepted that, in solid-phase sintering, the sintering temperature is slightly above two thirds of the melting temperature [47]. According to the research work done on SiC based ceramic by SPS, the temperature ranges from 1700 to 2200 ^{o}C, and has a dwelling time within 10 minutes [48-51]. Thus, the major interest in the sintering parameters will be in heating rate and pressure. Kodera et al. [51] consolidated the nano-metric SiC/BN without any sintering aid under the pressure of 50-70 MPa and heating rate of 100 ^{o}C/min, achieving the final density of approximately 90-99%. Lara et al. [52] carried out the SPS of additive-free SiC with pressure from 50 through 150 and a heating rate of 200 ^{o}C/min, reaching 97.0±06% theoretical density. Lomello et al. [53] obtained a 96% densification of nano SiC by SPS under the pressure of 73

12

MPa and heating rate of 185 ^{o}C/min. Recently, Shidona et al. [54] analyzed SiC ceramic with Al$_2$O$_3$-TiO$_2$ as additives by SPS, and achieved a density of 96% with the pressure of 50 MPa and heating rate of 50 ^{o}C/min. As limited work has been done on the SiC-TaC-MWNT system by SPS, heat rate and pressure should be chosen carefully since a high heating rate will decrease the grain size, and the application of pressure will reduce the pores and enhance the diffusion.

1.4.2   Oxidation resistance of Ta additives in SiC based ceramic

SiC is a potential ceramic for structural applications at high temperatures, which exhibits excellent oxidation resistance and high thermal shock resistance. It is not surprising that SiC has been chosen as an additive or coating to improve oxidation resistance [52-54]. The oxidation property of SiC is strongly dependent on the formation of dense SiO$_2$ film separating the oxygen in gas flow from the ceramic base. When exposed to high temperature in a flowing environment, the SiO$_2$ will be lost through evaporation or active oxidation [55-56]. Another issue worthy of mention is the phase transformation coupled with the thermal expansion coefficient difference, which can easily lead to cracking under thermal transient conditions.

Tantalum carbides form a family of binary compounds of tantalum and carbon with the empirical formula TaC$_x$, where x usually varies between 0.4 and 1, and are stable for a large range of 0.76-1. Because of the strong covalent-ionic bond, TaC has the high hardness greater than 20 GPa and the elastic modulus of up to 550 GPa [33]. The melting point of TaC is among the highest for binary compounds, and peaks at about 3880 ^{o}C, which exceeds the combustion flame temperature of most propellants [57]. This combination of properties makes TaC potentially useful in the application for thermal protection systems in aerospace thermal

protection systems. Many attempts have been made to enhance the oxidation resistance of different composites by adding TaC as reinforcement [58-60], and good results were achieved.

Due to the similar thermal expansion coefficients and good chemical compatibility of TaC and SiC, the combination of these two compounds as a choice for oxidation resistance additives is not new [61]. Opila et al. [62] carried out detailed research on the oxidation resistance effect of Ta additions. According to their work on 20 vol.% TaC additives for ZrB_2-SiC oxidized under 1627 ^{o}C for 10 minutes, no effective improvement was detected. However, Wang et al. [63] examined the oxidation behavior of ZrB_2-SiC-TaC ceramics with various TaC content in the temperature range of 1200-1500 ^{o}C, and reported that 10 vol.% of TaC exhibited the deteriorated oxidation resistance, while 30 vol.% of TaC showed the enhanced oxidation resistance. To date, the oxidation resistance behavior of TaC with SiC to CNTs has not been studied as extensively as other transition metal diborides such as ZrB_2 and HfB_2. Thus, it would be of great significance to investigate the oxidation resistance of the TaC-CNTs-SiC system.

1.4.3 High strain rate dynamic behavior of CNT reinforced CMCs

Impact failure of CMCs is a complex phenomenon involving a multitude of simultaneous microcrack initiation, growth, and coalescence into macrocracks. Intact fibers in a CMC will not always arrest a propagating crack in the ceramic matrix, where the propagating crack is known to tunnel around the fibers with little resistance. The crack propagation absorbs much more energy than crack initiation, resulting in different failure modes, such as matrix crack, fiber breakage, and fiber pull out [64]. From a mechanics viewpoint, the consequences of an impact are threefold: stress waves or shock waves are propagated inside the impact bodies; large inelastic deformations might be developed, typically at high rates of deformation; and the entire impacted

14

structure might be excited by the impact, leading to structural dynamics and vibration problems. Our focus is associated with the propagation of the nonelastic waves and with the measurement of high strain rate behavior [65].

Zukas et al. [66] pointed out that the failure of material from penetration depends on such variables as material properties, impact velocity, projectile nose geometry, target thickness, relative mass of projectile and target, etc. Wen [67] examined the effect of nose shapes for the perforation of thick FRP laminates, and obtained good theoretical predictions of the ballistic limits by analytical equations. The effect of laminate stacking sequence subjected to projectile impact was tested by Hitchen et al. [68] and Will et al. [69]. The influence of target thickness on the perforation process can be found in the works of Gellert et al. [70] and Borvik et al. [71]. The penetration response as a function of impact velocity has been studied by Orphal et al. [72] and Charles et al. [73]. Hashin failure criteria was considered in the finite element model to analyze the dynamic impact loading by Fan et al. [74]. The influence of target size, projectile size, projectile shape, and striking location was investigated, and the results showed that perforation energy increases rapidly with target thickness. A recent work on the hygrothermal effect on the response of graphite/epoxy laminates to high strain rate penetration was undertaken by Wosu et al. [75]. They reported that failure strain and displacement increased linearly with temperature and moisture, and that particle velocity also increased linearly with temperature, but was independent of moisture content. Compared with large data on the dynamic impact response of polymer matrix composites, limited studies are available on the ceramic based composites [76-78]. Lankford [76] studied the influence of hydrostatic pressure and the corresponding failure mechanisms for SiC-reinforced glass-ceramics at different strain rates, and observed the dilatational fracture within the matrix dominated composite failure at low pressure, and the shear

dominated mechanisms based on fiber kinking under high pressure. Hohler et al. [77] presented the oblique penetration performance for ceramic composites, and investigated the effect of configuration on the penetrator scale and velocity on ballistic limit and penetration depth. Shokrieh and Javadpour [78] applied Ansys/Lsdyna software to determine the ballistic limit velocity of the ceramic composite armor, and showed that the strain rate was very important for the simulation of the penetration process.

With the discovery and application of CNTs, interest has been attracted in the investigation of high strain rate behavior of CNTs reinforced composites [79- 84]. Grujicic et al. [79, 80] studied the ballistic performance optimization of the CNTs/E-Glass reinforced composite mats. By varying the location and thickness of the CNTs reinforced composite mats, they concluded that both the position and the thickness of CNTs reinforced composite mats affected ballistic performance of the armor. Makeev et al. [81] examined the dynamic response of CNTs reinforced a-SiC matrix composites. They found that the presence of aligned nanotubes leads to a reduction of shock-wave velocity and modifies the shock-wave front structure in a wide range of impact velocities. Morka and Jackowska [82] numerically investigated the ballistic resistance of CNT reinforced composites with the finite element method implemented in LS-DYNA code and indicated that CNT fibers play an important role in the ballistic resistance of the composites. Coppola et al. [83] reported that, by combining the CNT and GRP with cement composites the energy strength is increased under dynamic conditions, and the higher the CNT content, the higher are both fracture energy and tensile strength due to the nanoparticles opposed to wave and crack propagation that increase the high strain rate strength. Pandya et al. [84] presented the ballistic impact behavior of CNT dispersed resin and composites. By studying the damage and energy absorbing mechanisms for the composites, they observed that the damage

16

size on the target around the point of impact decreases with the addition of nanoparticles. Deobald et al. [85] developed a bar impact test to study the dynamic fracture responses of the precracked ceramic composites. Laurenzi et al. [86] studied the impact resistance of multi-walled CNTs reinforced epoxy through the Charpy test, with projectile velocity ranging from 490 to 950 m/s, and showed that the nano-reinforced panel had better ballistic behavior compared with the reference one. Wang et al. [87] recently carried out a temperature-dependent impact test on CNTs reinforced composites, in which the influences of material property gradient, volume fraction distribution, temperature change, initial stress, initial velocity, and contact force were discussed.

1.4.4 Fracture toughness for CNTs reinforced CMCs

CNTs have been considered one of the most promising nanoscale materials due to their superior structural, mechanical, and electronic properties [88-89]. CNTs have found a wide application as reinforcements in various matrix materials to impart stiffness, strength, and toughness. Among which, the fracture toughness of CNTs/ceramic composites have been scrutinized a great deal, as CNTs additives make the ceramic matrix much tougher and stronger than that of the conventional grain size one.

Ma et al. [90] prepared CNTs/SiC composite powder via mixing nanosize SiC particles with 10 vol.% CNTs and then hot pressing it. They reported a 10% enhancement on both the strength and the fracture toughness, as compared to the monolithic ceramics. Jiang et al. [91] prepared the MWNTs reinforced SiC composites by non aqueous tape casting and hot pressing. An improved fracture toughness of 8.7 ± 0.5 MPa·m$^{1/2}$ was obtained for SiC ceramic composites with 0.25% MWNTs. Chang et al. [92] fabricated the alumina and alumina matrix composite

17

with 5-20 vol.% MWNTs by hot pressing, and found an improvement of 24% on fracture toughness, compared with the single phase alumina. Zhan, et al. [41], however, employed SPS to prepare the SWNTs reinforced alumina-based nanocomposites, and showed great improvement in fracture toughness. Bakshi et al. [5] concluded that longer CNTs were more effective in increasing the fracture toughness and observed an increase of 60% for TaC-4 wt.% CNT by SPS.

Fracture is, in essence, the formation and propagation of matrix cracks followed by successive fiber failure. The most common toughening mechanism associated with fiber reinforced CMCs is debonding, crack deflection, crack bridging, fiber pull out, etc. Toughness in CMCs is typically achieved through a weak fiber/matrix interface coupling that permits debonding and sliding of the fibers within the matrix. The interfacial debonding results from a weak interface in comparison to the matrix and fiber, and is a moderate energy dissipation mechanism that resists crack growth. Crack deflection is the crack propagating further in front of the debonded interface along the same or a different plane with respect to the initial notch. Crack bridging is in reference to the fibers stretching freely along the separating crack faces, but along the debonded length. With further loading, the energy stored with individual stretching bridging fibers will eventually reach a critical level resulting in fiber failure [93].

Most work on CNTs reinforced CMCs focuses on the measurement of toughness by different methods. Due to the small volumes of material, the indentation/crack-length method has been chosen to measure the fracture toughness. Zhan et al. [43] reported a three times improvement of fracture toughness for CNTs reinforced alumina, based on indentation measurements. Wang et al. [94], however, questioned the validity of this method for measure of CNT reinforced CMCs by using a macroscopic method, i.e. the single edge V-notched beam test (SEVNB). Though only showing modest [95-96] or no increase at all [97-98] for the

18

measurement of fracture toughness by SEVNB, compared with indentation, it is suggested that the toughness for CNT reinforced CMCs should be measured by SEVNB due to the high resistance to damage contact [99]. Except for the quantitative study of fracture toughness, direct observation of the toughening mechanism was also carried out. Xia et al. [100-102] fabricated a highly ordered array of parallel MWNTs in an alumina matrix, using the in situ CVD method, and for the first time demonstrated the toughening mechanisms found in micron-scale fiber composites: crack deflection, crack bridging, and CNT pull out. Gu et al. [103] also observed the CNTs pull out, breaking, and slipping during failure for CNT/SiC composites fabricated by the chemical vapor infiltration (CVI) technique. They reported an order of magnitude higher for the fracture strength, improved by the fracture mechanisms for the CNTs/SiC as compared with the bulk SiC.

1.4.5 Failure and damage models for composite materials

Failure and damage models of composite materials for high-strain rate dynamic impact responses have developed both analytically and numerically. Some analytical solutions for particular impact induced damage can be found in the literature [104-106]. These solutions are limited to simple impact cases where the transverse shear deformation and rotary inertia are not considered, and the contact is assumed to be localized. Also, the geometries of the projectile and plates are not described, which makes the calculation inaccurate. In order to overcome these restrictions, generalized numerical models are required [107]. Different commercial finite element codes, such as ABAQUS/Explicit, MSC/DYTRAN, LS-DYNA, and PAM-Shock, have been found to be capable of creating a composite damage model, running a damage induced loading event, and post-processing the failure information [108]. These codes have advanced

contact algorithms to deal with the contact problems in the dynamic impact process, and moreover, they allow for the implementation of user-defined subroutines to customize the specific material models.

The use of appropriate user-defined material models plays a crucial role in modeling the impact damage, controlling the extent of damage, energy absorption, stiffness reduction, and the final dynamic structural behavior. Most composite failure models embedded in a finite element analysis tool perform the stress analysis at a materials point, evaluate the failure initial criteria and the possible progressive material properties, and then continue to the next increment [109-111]. The constitutive models relate the state of strain to the state of stress, and these relations may be different depending on the kinematic assumptions of the formulation.

The failure initial criteria are defined in a manner based on the available laminate level material data. The current user subroutine implementation for failure initiation involves four common criteria, namely, the maximum stress criteria, the maximum strain criteria, the Tsai-Wu failure polynomial, and the Hashin criteria. The maximum stress or strain criteria are simple non-interacting failure criteria that compare each stress or strain component with the corresponding material ultimate strength allowable value. The Tsai-Wu failure polynomial [112] is an interacting failure criterion since all stress components are used simultaneously to determine whether or not a failure at a materials point has occurred. It provides only a single condition for local materials failure and cannot identify the mode of failure. The Hashin failure criteria [113] are also interacting failure criteria, as the failure criteria use more than a single stress component to evaluate different failure modes. The Hashin criteria were originally developed for unidirectional fiber composites in terms of quadratic stress polynomials, and then applied to other laminate types or non-polymeric composites for approximation. The advantage of using

20

Hashin failure criteria is that, it identifies the failure modes independently, and namely, the tensile and compressive fiber failure, the tensile and compressive matrix failure, and the interlaminar tensile failure, resulting in a piecewise smooth failure.

Since the composite structure doesn't completely lose its load carrying capacity and can still support additional load when the failure or damage occurs at a material point, before it eventually fails, it is important to quantify damage caused by the initiation of a failure mode and study its progressive behavior during the event. Various material degradation models have been proposed and demonstrated for numerical modeling in composite structures, and they can be divided into three categories: heuristic models based on a ply-discounting material degradation, continuum damage mechanics (CMD) using internal state variables, and peridynamics applied in a non-local mathematical framework. Ply-discounting materials degradation models are based on the degradation of the elastic materials' stiffness coefficients, or directly degrading the elastic mechanical properties and then re-computing the local materials' stiffness coefficients. Examples of the ply-discounting approach and related computational details can be found in the literature [114-116]. The CMD approach generally describes the materials as a continuum, having a smooth and homogenized field. This method was first applied to composite materials by Talreja [117] and it has the potential to predict different composite failure modes involving matrix cracking, fiber fracture, and delamination. Recent works of CMD regarding impact damage on composite plates refer to literature [118-122]. Nearly all governing equations of the FEM are based on the partial differential equations (PDEs) of classical continuum mechanics requiring that the spatial derivatives of the PDEs exist at crack tips and along cracked surfaces, which is impossible. The Perydynamic model, first proposed by Silling [123], treats the crack nucleation and propagation with arbitrary paths without any special numerical techniques or criteria. It

presents a unique capability of predicting damage and the progressive failure of materials at both a macro- and micro-scale. The application to damage and fracture in composite materials is discussed in literature [124-126].

2.0 SPARK PLASMA SINTERING OF TAC AND/OR CNTS REINFORCED SIC CMCS

2.1 INTRODUCTION

The processing parameters play an important role in the densification, microstructure, mechanical, and thermoelectric properties of samples. Based on framework 1.3.1, this chapter will investigate these running parameters, such as pressure, heating rate, and temperature, on the densification behavior and mechanical properties of TaC and/or CNTs reinforced SiC ceramic composites. It will also be of great interest to learn how the sintering process is affected by the presence of reinforcements such as CNTs and TaC, and how the stability of CNTs is affected by the electric field and high temperatures.

SiC ceramics are one of the best candidates for high temperature structural applications, due to the strong covalent bonds that limit dislocations, and therefore plastic deformation, as compared with metallic materials [127-128]. However, with increase of temperature, grain boundary sliding takes place, resulting in a time dependent plastic deformation [129]. Such a thermal-activated effect is not desirable in SiC ceramics for structural applications. Carbon nanotubes (CNTs), which have been shown to possess excellent mechanical, thermal, and electrical properties, are expected to improve the overall quality of the SiC matrix. In order to get the full benefits of CNTs, it is crucial to distribute CNTs throughout the matrix material

homogenously and ensure that CNTs remain undamaged during high temperature and high pressure processing, and optimize the interfacial bonding between CNTs and the ceramic grains.

Conventional fabrication of CNTs reinforced CMCs involves hot pressing techniques [90, 130-131]. These techniques are characterized by high pressure and long processing time, but can destroy CNTs [17, 132]. In contrast, spark plasma sintering (SPS) is attracting significant interest due to rapid consolidation with almost full densification of materials at a relatively lower temperature and a much shorter holding time. It is reported that samples sintered with the aid of SPS tend to have cleaner grain boundaries, improved bonding quality, and a finer microstructure [133-135].

Sintering, in practice, is the control of both densification and grain growth. Densification is the act of reducing porosity in a sample, thereby making it denser. Grain growth is the process of grain boundary motion and Ostwald ripening to increase the average grain size. The exact densification mechanism of SPS is still under debate, but it is widely accepted that Joule heating at the particle contacts and/or sparks at the gaps between particles are widely involved. A preload sintering pressure is applied to rearrange particles, which will remove porosity of the powder. Further densification results from simultaneously applying temperature and pressure, which will cause the surface energy reduction and diffusion of atoms through the microstructure. High localized temperature created by Joule heating and sparks production lead to the evaporation and subsequent surface diffusion. This evaporation and melting on the surface of particles cause necking of particles, leading to volume diffusion, while the expansion of necks forms grain boundaries through plastic deformation [133].

The high covalency of Si-C bonds and the low self-diffusion coefficient of SiC make densification more difficult. To obtain a high density sintered SiC ceramics, mechanisms that can

provide the high amount of energy required for the formation and migration of defects are necessary. Prochazka [136] achieved a near theoretical density of submicron size beta SiC with the additives of boron and carbon. His work revealed that very fine SiC particle size, along with B and C additives, would promote sinterability by enhancing volume diffusion and retarding surface diffusion. Hausner [137] also studied the effect of B and C addition on the sintering of beta-SiC, and pointed out that a high grain boundary to surface energy ratio (γ_{GB}/γ_{SV}) hinders that densification process, and the addition of B decreases the grain boundary energy (γ_{GB}) while C increases the effective surface energy (γ_{SV}). Another mechanism which enhances the sintering effect of sintering aids is achieved by reaction of the oxygen content of SiC powder. B_4C has been reported in the literature [138,139] as an effective sintering aid to eliminate surface oxides presented in SiC and TaC particles toward enhancing densification.

2.2   EXPERIMENTAL PROCEDURE

2.2.1   Powder preparation for SPS

Commercially available high purity sub-micron beta SiC powder, TaC powder and B_4C powder were obtained from US Research Nanomaterials Inc., TX, USA. The MWCNTs employed in this study were obtained from Cheap Tubes Inc., VT, USA. More detailed information of the materials used is listed in Table 2-1.

Table 2-1 Specification of materials used

Material	Density (g/cm3)	Average size	Purity, %
SiC	3.216	800 nm	>99
TaC	13.9	1000 nm	>99
MWCNTs	2.1	Do<20 nm, Di: 4 nm, L: 1-12 um	>99 wt
B_4C	2.51	45-55 nm	>99

It is critical that the CNTs are distributed uniformly into the matrix. Being the most popular technique today, ultrasonic agitation exposes CNTs to ultrasonic waves and transfers shear forces to individual nanotubes, which break them from agglomerates [140, 141]. First, the non-functionalized multi-walled carbon nanotubes were added to the ethanol solvent at a concentration of 1.0% weight per volume, forming a nanotube suspension, and then ultrasonicated for 45 minutes to disperse the nanotubes in the ethanol solvent. Subsequently, appropriate weight percentages of SiC, B_4C and/or TaC were added and fully stirred by ultrasonication again for 90 minutes. In the last step, the homogeneous suspension was baked for about 10 hours until completely dry, and then crushed to form the SiC-4 wt% CNTs-4 wt% TaC-1 wt% B_4C (Blend #1) and SiC-4 wt% CNTs-1 wt% B_4C (Blend #2) powders. SEM images of the as mixed Blend #1 powders are shown in Fig. 2-1. As can be seen in Fig. 2-1(c) and (d), the CNTs were well distributed within the SiC powders.
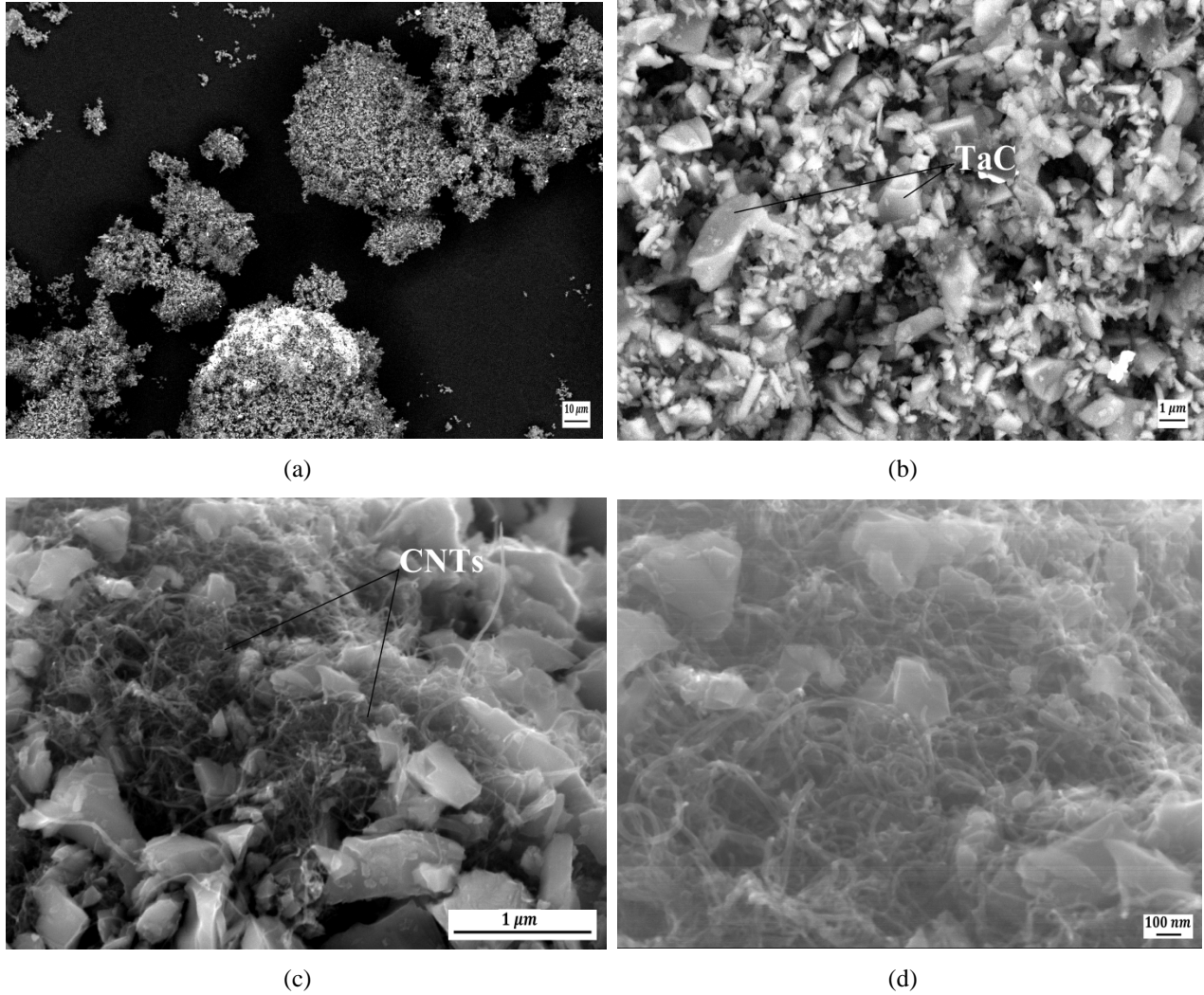
Fig. 2-1 SEM images showing the powder mixtures of SiC-4 wt% CNTs-4 wt% TaC-1 wt% B_4C

2.2.2 Spark plasma sintering

The DR. SINTER spark plasma sintering system from Fuji Electronic Industrial Co., Ltd was utilized to sinter the SiC ceramic composite samples at California Nanotechnologies (CalNano) (Cerritos, CA, USA). The SPS system consists of the heating furnace, the power unit, and the computer acquisition unit, as shown in Fig. 2-2. Fig. 2-3 shows the exterior of the heating furnace and the interior of the furnace chamber. The vacuum chamber is the main part of the heating furnace, with the graphite spacers, graphite die and punch, and the electrodes. The

powder is placed in between the cylindrical graphite die and punch, while the graphite cloth is wrapped around this assembly to provide thermal insulation. It is required that the die and punch holding the powder are centered vertically within the spacers. A digital radiation thermometer (IR-AHS) was aimed at the outer surface of die to monitor the sample temperature during sintering. The minimum temperature detected by the thermometer was $550^{o}C$. After loading the powder, the chamber was evacuated, and then purged three times with nitrogen gas to ensure a full inert operating atmosphere. The sintering current, voltage, pressure, temperature and vacuum valve were controlled with the power unit. The computer acquisition unit captured all the above mentioned parameters' time history for each of the samples.
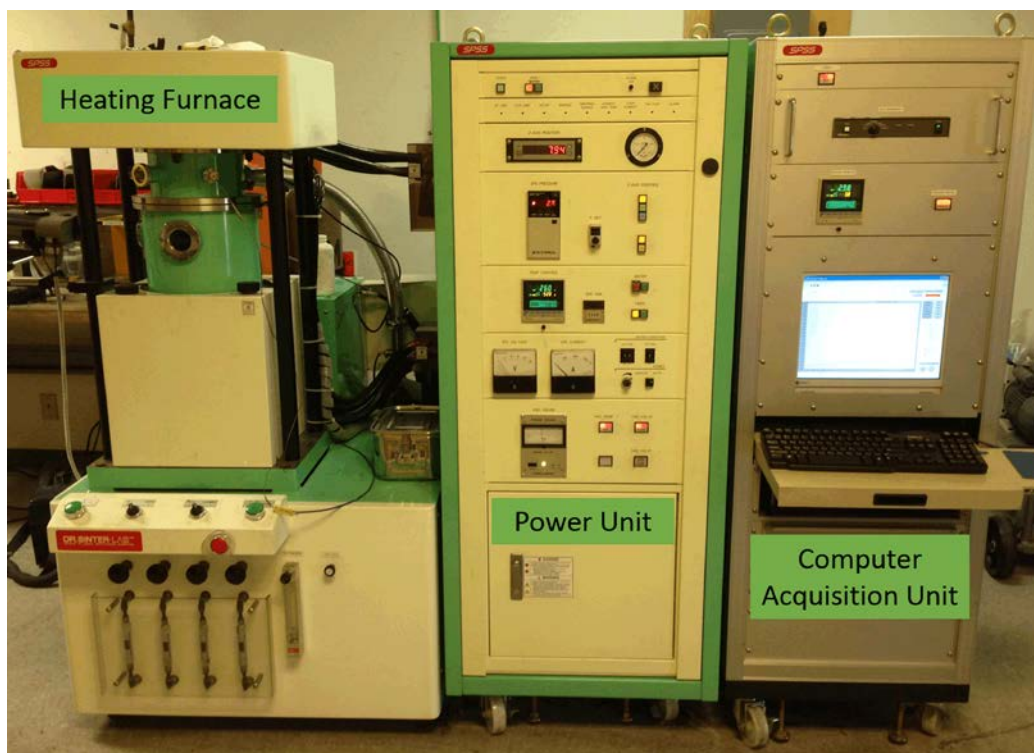
Fig. 2-2 SPS system at CalNano showing three main units: heating furnace, power unit and computer acquisition unit

<div align="center">(a)   (b)</div>
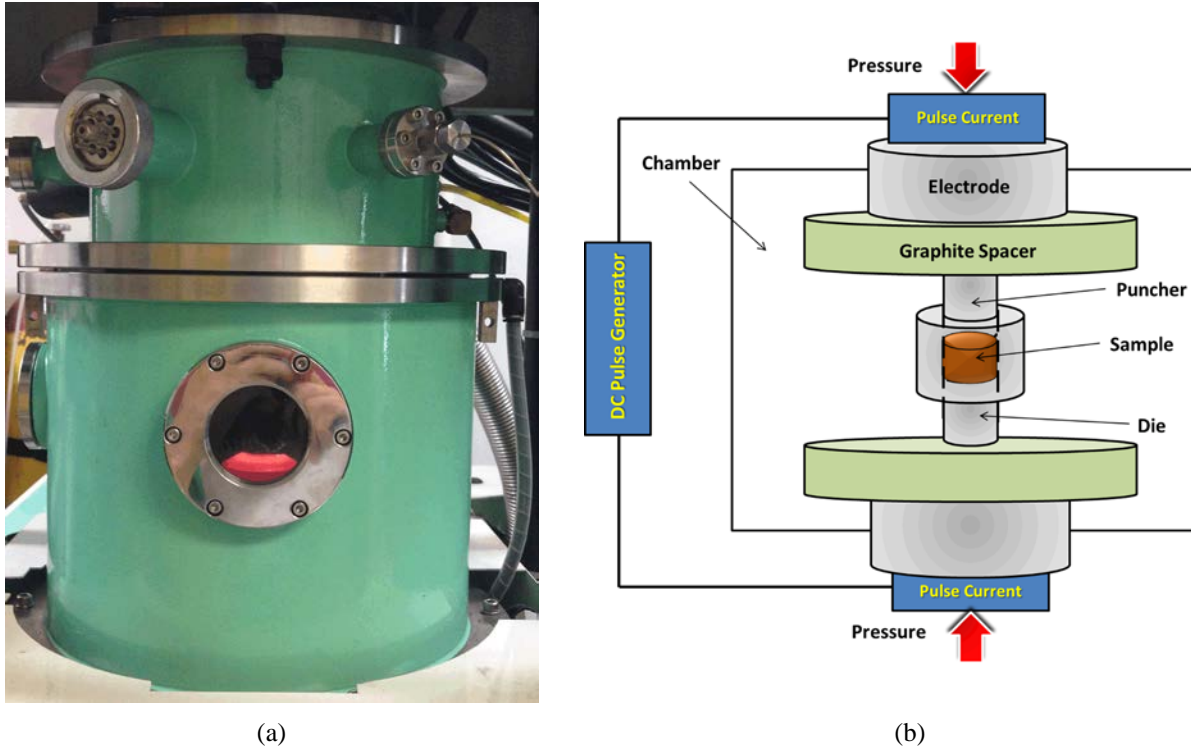
Fig. 2-3 (a) Exterior view of sample sintering in the furnace; (b) Schematic of SPS process inside the furnace

2.2.3 Fabrication of SiC based CMCs by SPS

Silicon Carbide and Silicon Carbide composites (SiC-1 wt% B_4C, SiC-4 wt% CNTs-4 wt% TaC-1 wt% B_4C and SiC-4 wt% CNTs -1 wt% B_4C) were sintered in the vacuum by spark plasma sintering. Fig. 2-4 presents the processing parameters as a function of time during SPS processing. Pulsed direct current was passed through the powder by electrodes, and was increased until the final temperature was reached. The sintering process was initiated with simultaneous increases in temperature and pressure. A heating rate of 133 ^{o}C/min was used for the first 9 minutes until the temperature reached 1200 ^{o}C, and then with a holding time of 3 minutes for increasing the pressure, the temperature was adjusted to 1800 ^{o}C in 5 minutes and maintained for 10 minutes at the given temperature of 1800 ^{o}C. A two stage uniaxial pressure

<div align="center">29</div>

with an initial value of 30 MPa was applied during the first stage of temperature climbing, and the maximum value of 90 MPa was reached before the second stage of temperature increase, through the upper electrode by the hydraulic system. The sintering behavior was monitored by measuring the change in the axial displacement of the punch. The current and loading were ceased at the end of sample soaking time, with a total time of 27 minutes. After cooling down naturally, samples were removed from the die and the final product was a dense disk with a diameter measuring about 20.8 mm and a thickness ranging from 3-6 mm.
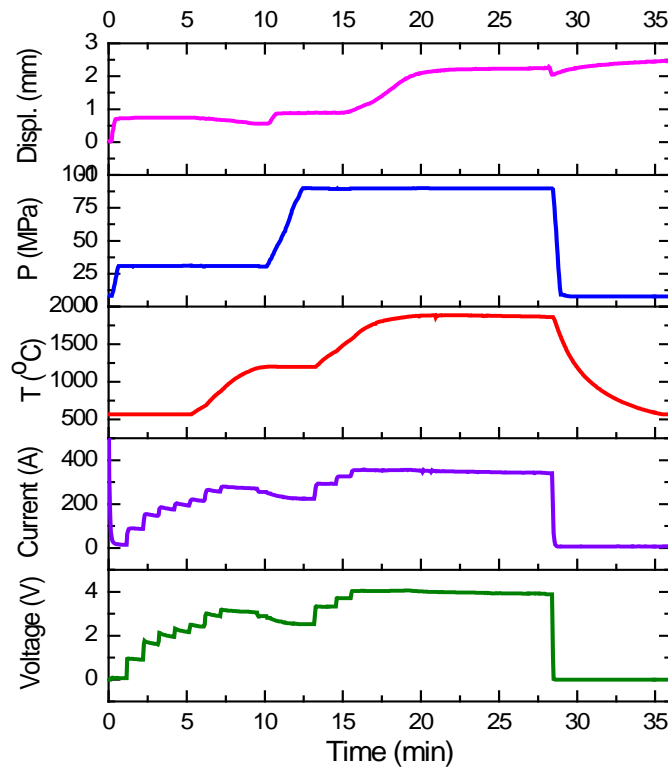
Fig. 2-4 Evolution of sintering parameters as a function of time

2.2.4 Materials Characterization

2.2.4.1 Relative density and grain size measurement

The theoretical density of the SiC based composites was calculated according to the rule of mixtures, while the absolute densities were measured by the Archimedes method. Samples were placed in a drying furnace at about 200 $^{\circ}$C for 2 hours, and then weighed in air (m_1). Next, the samples were immersed in water for 24 hours to fill open porosity, and then weighed hanged in the water (m_2, which corresponds to Archimedes buoyancy). The relative density RD (%) was calculated according to Eq. (1):

$$RD = \frac{m_1}{m_2} \frac{\rho_{flu}}{\rho_{mat}} \tag{1}$$

where ρ_{flu} is the wetting fluid density (in this study is water, ρ_{flu}= 1 g/cm^3 at 20 $^{\circ}$C), and ρ_{mat} is the material's theoretical density.

Using a simple rule of mixtures and taking the density of 3.216 g/cm^3 for SiC, 2.1 g/cm^3 for MWCNTs, 13.9 g/cm^3 for TaC, and 2.51 g/cm^3 for B$_4$C (shown in Table 2-1), the theoretical densities of SiC-4 wt% CNTs-4 wt% TaC-1 wt% B$_4$C (Blend #1), SiC-4 wt% CNTs-1 wt% B$_4$C (Blend #2) and SiC-1 wt% B$_4$C (Blend #3) should be 3.237 g/cm^3, 3.140 g/cm^3 and 3.207 g/cm^3, respectively.

The grain size was measured from the SEM (Philips XL 30 FEG) image at different magnifications, using the software Image J. Since SEM images are two-dimensional projections and the shapes of the particles are not completely regular spheres or polyhedrons, more than 100 grains were counted and measured to arrive at the results of effective grain size information.

2.2.4.2 Mechanical properties characterization

A Hysitron TriboIndenter (Hysitron Inc., Minneapolis, MN, USA) was used to measure young's modulus and hardness for the sintered samples on the polished sections. The nanoindentation test was carried out at a load of 5 mN applied in 10 seconds and then unloaded in 10 seconds. The reduced young's modulus E_r is related to the young's modulus E_s of sample in the following expression:

$$\frac{1}{E_r} = \frac{1-v_i^2}{E_i} + \frac{1-v_s^2}{E_s} \tag{2}$$

where the subscript i indicates a property of the indenter material, the subscript s indicates a property of the sample material, and v is Poisson's ratio. For a diamond indenter tip used in this test, E_i is 1140 GPa and v_i is 0.07. The Poisson's ratio of SiC v_s is taken equal to 0.14 [142].

2.2.5 The effect of sintering parameters on the microstructure and mechanical properties of SiC-based ceramics

Typically, there are three ways to improve the densification and microstructure of SiC-based ceramics. The first way is to use sintering aids of small quantities of C and B or Al and their compounds, such as B_4C and Al_2O_3 [143]. The second way is to explore innovative sintering techniques, including SPS, which is known as the field assisted sintering technique. The third way is to adjust the sintering parameters, which plays an important role in the final densification and properties of the sintered material [144]. The various SPS sintering parameters involve heating rate, maximum hold temperature, cooling rate, pressure application rate, maximum hold pressure, and pressure release rate. Since the SPS equipment in this research

work employs a natural cooling system, and the pressure was turned off at the end of the maximum temperature holding time, cooling rate and pressure release will not be considered.

One major concern of the SPS technique employing one-stage heating temperature and loading pressure is that it would develop temperature gradients at the cross sections of samples, which degrades the densification and mechanical properties [145-146]. Thus, the two-stage sintering technique, as shown in Fig. 2-4, was developed to achieve the improved densification and mechanical properties, which involved holding samples for certain durations before reaching the final temperature and pressure.

2.3 RESULTS AND DISCUSSION

2.3.1 Effect of CNTs and TaC additives on SiC-based ceramics

Backscattered electron images in the SEM display compositional contrast resulting from different atomic number elements and their distribution for Blend #1, reinforced by both the CNTs and TaC. EDS analysis allows one to identify each element and their intensities as presented in Fig. 2-5. It can be identified that the grayish white phase is SiC, while the white and dark phases are TaC and B_4C, respectively.
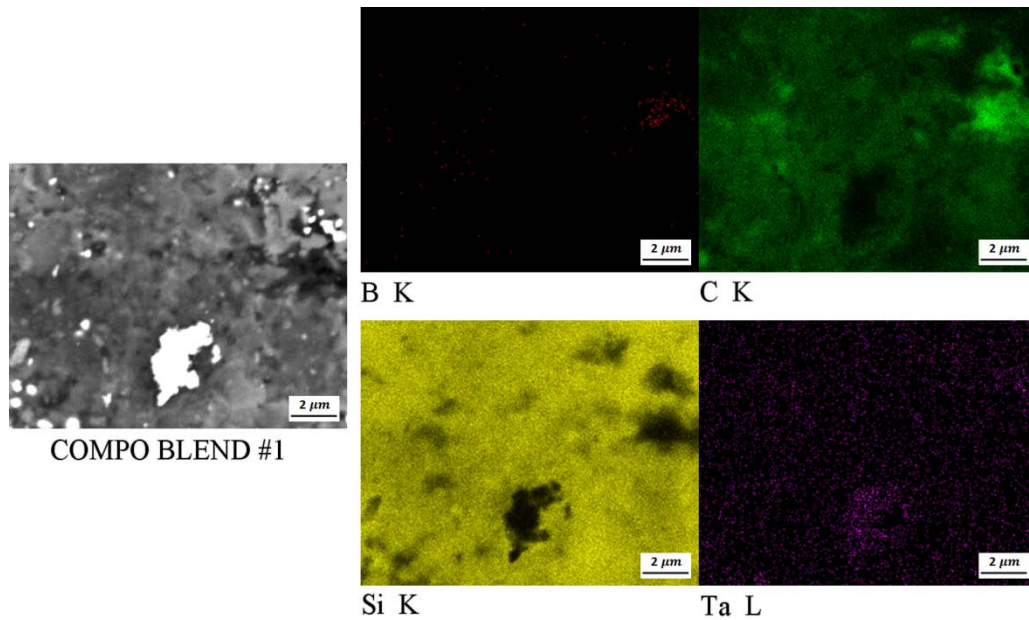
Fig. 2-5 EDS mapping of the distribution and intensity of elements over the scanned area from Blend #1

Microstructural development from the fracture surfaces of Blend #1, 2 and 3, prepared using a heating rate of 133°C/min, a maximum temperature of 1800°C and a maximum pressure 90 MPa, was observed in SEM and presented in Fig. 2-6. The fracture surface of Blend #1 showed generally well distributed CNTs and TaC between SiC particles with minor porosity and slight grain size uniformity. Observation from the fracture of Blend #2 revealed a high dense grain structure with most CNTs located at SiC boundaries and some inside the grains. The pure SiC fracture surface exhibited a porous structure with grain size nearly equivalent to the starting particles. Fig. 2-7 presents a high magnification SEM micrograph from the fracture surface of Blend #2, showing the CNTs' networks located at the SiC boundaries and inside the grains. It can be clearly seen that the CNTs were retained in the SiC composites processed with the SPS. The rapid heating rate and short holding time involved in the SPS eliminated the risk of CNT degradation or strong interfacial reaction between the CNTs and ceramic matrix [147].
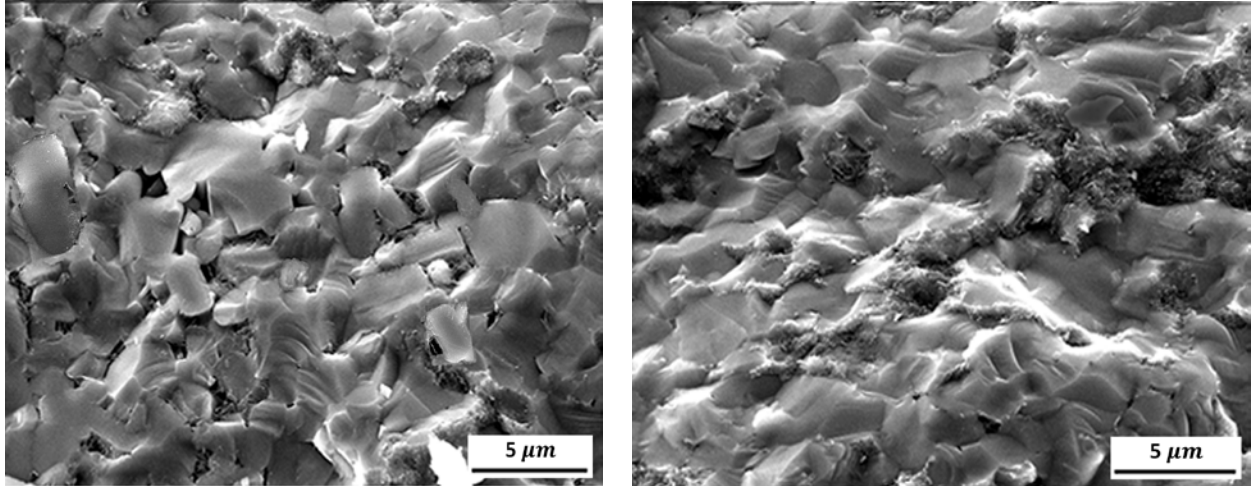
(a)   (b)
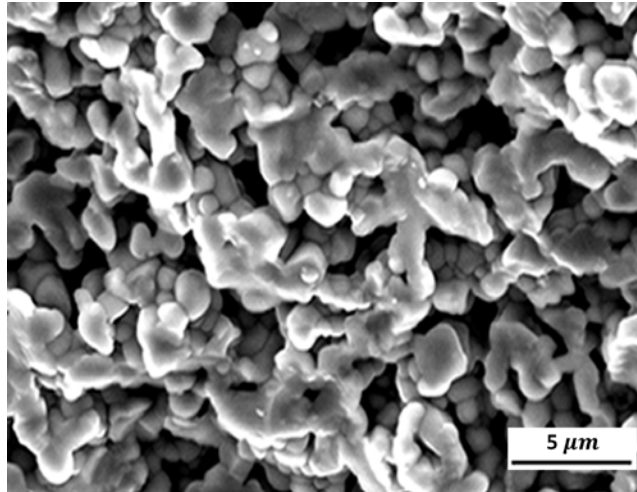
(c)

Fig. 2-6 SEM micrograph of fracture surfaces of SiC-based ceramics prepared by SPS (a) Blend #1, (b) Blend #2,

and (c) Blend #3
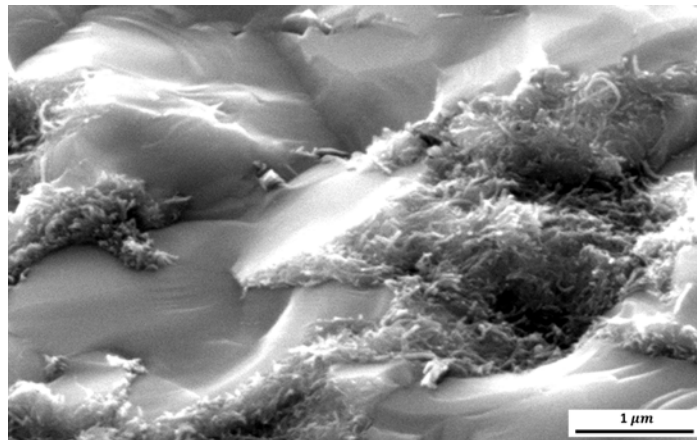
Fig. 2-7 A high magnification SEM micrograph from the fracture surface of Blend #2

Fig. 2-8 shows the variation of relative density and grain size of the SiC-based powders. The error bars represent the standard deviation. For the given SPS sintering parameters, the relative density of monolithic SiC (Blend #3) was about 86%, while the TaC and/or CNT reinforced SiC composites (Blend #1 and #2) achieved higher densification around 98.4% and 99.5%, respectively. Obviously, the addition of CNTs reinforcement favored the densification for both TaC/SiC and SiC ceramics, and a very small amount of CNTs (4 wt.%) could achieve almost full densification of SiC composites. In comparison of Blend #1 and Blend #2, it seemed that reinforcement of TaC inhibited the densification of CNT/SiC composites. The average grain size for pure SiC ceramics was 1.33, and increased to 2.20 and 2.11 when reinforced with TaC and/or CNTs. This could be attributed to the excellent thermal conductivity of CNTs which helps to improve the heat transfer and hence enhance the diffusion, but would cause the interparticle necks to grow. The relatively higher standard deviation of grain size in Blend #1, compared to Blend #2, may come from the larger starting particles of TaC (1000 nm) than SiC (800 nm), and also the fewer CNTs distributed around some larger grain interfaces, as can be observed in Fig. 2-6(a). Without CNTs acting as grain inhibitors to restrict the mobility, grain boundaries see exaggerated growth.

Young's modulus and the nanohardness of SiC-based ceramics measured by nanoindentation are plotted in Fig. 2-9. The average values of young's modulus measured for Blend #3 is 349 GPa, which was smaller than that of the published value (~410 GPa) [148], owing to the poor densification of monolithic SiC. With the addition of TaC and/or CNTs, the young's modulus of SiC composites increased to 436 GPa and 462 GPa for Blend #1 and Blend #2, respectively. The notable improvement in young's modulus (25-32%) was attributed to the high elastic modulus possessed by CNTs (~1 TPa) [149]. The lower value in young's modulus of

Blend #1, in relation to that of Blend #2, may come from the relative low elastic modulus of TaC (~283 GPa) [150], as well as the less densified structure of Blend #1 with porosity. As can be observed from the hardness curve, the average hardness for sintered pure SiC was 28.1 GPa. The values of hardness dropped to 26.9 GPa and 26.7 GPa for the Blend #1 and Blend #2 composites respectively, which indicated that CNTs had negative strengthening in hardness in CNTs/SiC ceramics. The slight higher value of hardness in Blend #1 than in Blend #2 composites seemed due to the hard TaC particles.
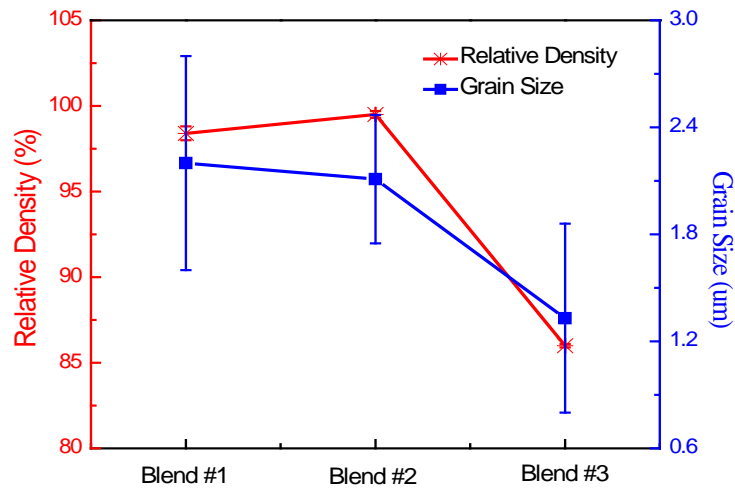
Fig. 2-8 Variation of relative density and grain size for Blend #1, Blend #2, and Blend #3 samples
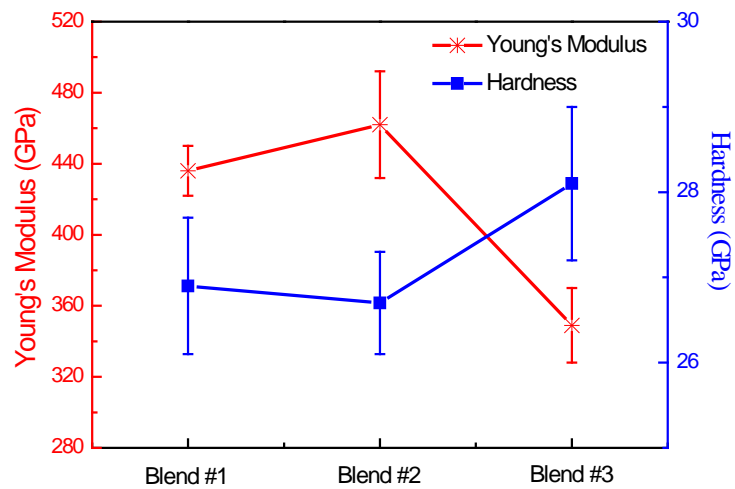
Fig. 2-9 Variation of young's modulus and hardness for Blend #1, Blend #2, and Blend #3 samples

To better understand the densification behavior of SiC-based composites with different additives (TaC and/or CNTs) during the SPS process, punch displacement was recorded for analysis. Fig. 2-10 shows the variation of punch displacement with sintering time, and reveals five distinct stages based on the timed application of pressure and temperature: initial increase due to pressure (stage I), slight decrease caused by surface diffusion (stage II), intermediate increase corresponding to the densification with higher pressure (stage III), further increase dominated by lattice diffusion and boundary diffusion (stage IV), and a final marginal increase during soaking time (stage V).

In order to achieve a more homogeneous temperature gradient and understand how the pressure and heating temperature affect the densification of samples separately during the sintering process, the two-stage pressure and heating temperature techniques were employed. Stage I and III involved increasing pressure only, stage II and IV related to temperature increases only, and the two parameters were maintained in stage V. A uniaxial pressure of 30 MPa was applied before increasing the temperature in the initial stage. The punch displacement in this stage was attributed to the rearrangement of particles and the clearing of agglomerates by the vertical pressure. Blend #1 and #2, with the reinforcements, achieved higher punch displacement (0.75 mm for both) than that of Blend #3 without (0.4 mm). When DC pulse passed through the powder in stage II, localized spark plasma discharge was generated between the particle contacts. This local high temperature activated surface diffusion energy, and caused interparticles neck growth leading to particle coarsening instead of shrinkage. It was deduced that the reinforcing phase of CNTs lubricated the particle surfaces and mitigated grain coarsening in stage II, as the punch displacement for Blend #2 changed much less compared with that of Blend #3. The reason that punch displacement for Blend #1 dropped more than Blend #2 may come from the size

difference and thermal expansion between TaC additives and the SiC matrix. In stage III, powders were driven to densify significantly under a rapid increase of pressure from 30 MPa to 90 MPa. There appears to be two stages in stage IV: in the stable first stage, neck growth continued and pores reached their equilibrium shapes, sitting along the grain edges; in the later stage, sintering mechanisms were dominated by lattice diffusion and grain boundary diffusion, which permitted neck growth as well as densification. Punch displacement increased dramatically during stage IV with a magnitude of 1.1 mm, 0.92 mm and 0.61 mm for Blend #1, #2 and #3, respectively. Note that the transition point between the two stages in stage IV shifted left for Blend #1 and #2 with additives, as compared with the pure SiC of Blend #1. This shift indicated a lower densification temperature for SiC-based ceramics with CNTs reinforcement. When added with TaC in the CNT/SiC composites, densification temperature would be increased as the transition point of Blend #1 shifted less than that of Blend #2, owing to the low self-diffusion coefficient of TaC, and thus poor sinterability. In the final soaking stage, pores were isolated and pinched off with punch displacement, and did not change significantly.

Obviously, the punch displacement data indicated that CNTs reinforcement helped to achieve a better densification for CNTs/TaC/SiC and CNTs/SiC composites, while TaC additives had a negative effect on the densification for CNTs/TaC/SiC composite due to the size difference and low self-diffusion coefficient. A finer particle size or higher sintering temperature might be needed in order to obtain a desirable relative density. The experimental data indicating higher relative density for Blend #1 and #2 were in agreement with these general observations made from punch displacement.
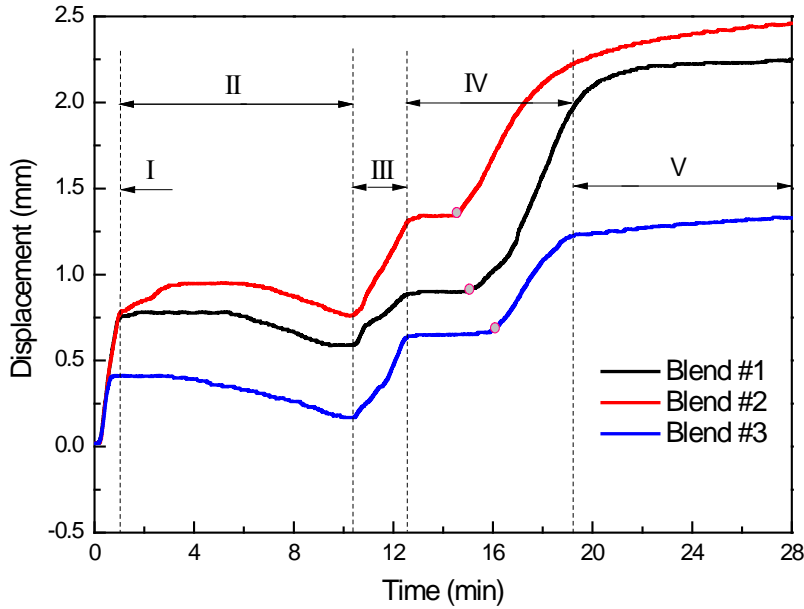
Fig. 2-10 Punch displacement profiles during SPS sintering cycles for Blend #1, Blend #2, and Blend #3

2.3.2 Effect of heating rate

Heating rate is one of the most important parameters of SPS that impacts the densification and grain size of the sintered materials. Depending on the geometry of the die/sample ensemble, thermal and electrical properties, as well as the electric power supplier, the heating rate varies from 100-600 ^{o}C/min. In order to study the heating rate's influence in the SPS of SiC-based ceramics, powders were processed at heating rates of 133 ^{o}C/min, 200 ^{o}C/min and 250°C/min, respectively, with a maximum sintering temperature of 1800 ^{o}C and maximum pressure of 90 MPa.

Fig. 2-11 shows the relative density and grain size under various heating rates for Blend #1 and Blend #2. It is observed that both the densification and grain growth decreased with an increase in the heating rate for the two blends. Apparently, TaC and/or CNTs reinforced SiC ceramics achieved a significant densification with little grain growth at a heating rate of

133°C/min. When the heating rate increased to 200 °C/min, the average values of relative density for Blend #1 and Blend #2 dropped to 95.8% and 96.2%, while the average value of grain size decreased to 2.08 and 1.62, respectively. The final densification for Blend #1 and Blend #2 at 250 °C/min was 93.1% and 94.9%, and the final corresponding grain size was 2.01 and 1.57. It is deduced that the rapid heating rate may influence the mobility of the grain boundaries, which accelerated the surface diffusion as well as the grain boundary diffusion. This high boundary mobility contributed to the rapid reduction of porosity and the hindrance of grain growth. However, the high heating rate provided by high currents may also cause local temperature gradients and local inhomogeneous densification.

Fig. 2-12 shows that young's modulus and the nanohardness of Blend #1 and Blend #2 decreased with the increase of the heating rate, which was attributed to the densification. Comparing Fig. 2-11 and Fig. 2-12, it can be found that both Blend #1 and Blend #2 exhibited the best mechanical properties in young's modulus and hardness at 133 °C/min when they achieved highest densification. For the SiC-based ceramics in the given study, young's modulus seems more sensitive to heating rate than hardness. Generally, a low heating rate promotes densification while a high heating rate helps in obtaining fine microstructure by inhibiting significant grain growth. 133 °C/min was an optimum heating rate for SiC-based ceramic in this study, and a heating rate higher than that resulted in lower densification, which in turn deteriorated the mechanical properties of samples.

(a)

(b)
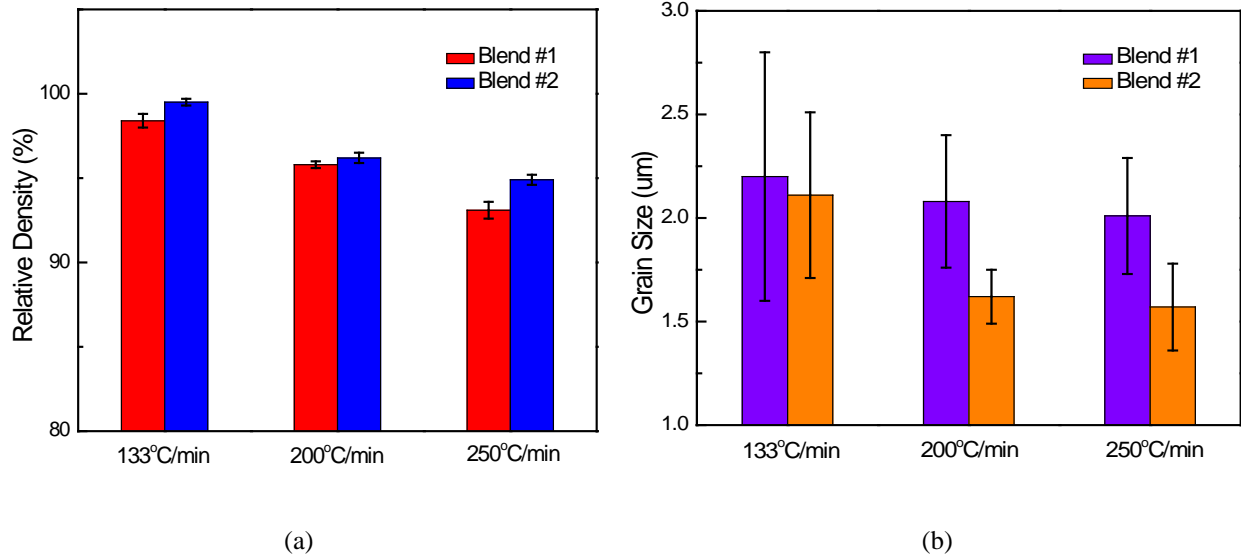
Fig. 2-11 (a) Relative density and (b) Grain size of SiC-based ceramics as a function of heating rate

(a)

(b)
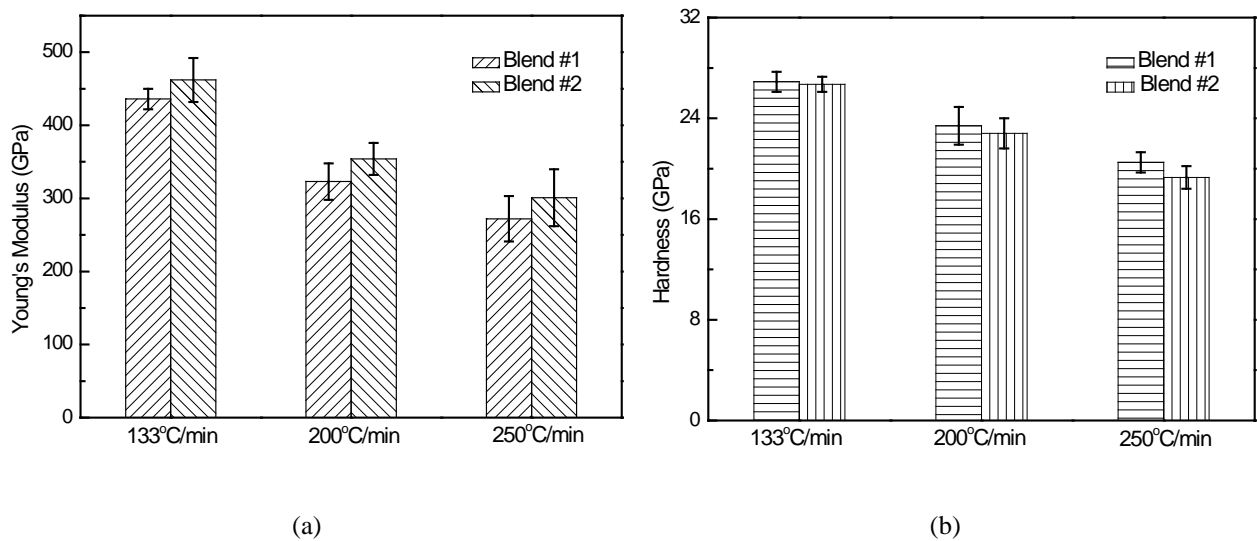
Fig. 2-12 (a) Young's modulus and (b) Hardness of SiC-based ceramics as a function of heating rate

2.3.3 Effect of maximum heating temperature

The sintering temperature is selected based on the melting point temperature (T_m) of the materials to be sintered. Garay [135] proposed a linear curve fit relationship between sintering temperature and relative density, which is expressed as:

$$\rho = s \left(\frac{T}{T_m} \right) + b \tag{3}$$

where ρ is the relative density, s is the temperature sensitivity, T is the sintering temperature, T_m is the melting temperature, and b is the intercept on the density axis. The majority of materials can reach full densification at 0.5-0.8 of their T/T_m. To study the influence of temperature in the SPS of SiC-based ceramics, powders were processed at maximum temperatures of 1700, 1800 and 1900 ^{o}C, respectively, with a heating rate of 133 ^{o}C/min and a maximum sintering pressure of 90 MPa.

Fig. 2-13 shows the temperature dependence of relative density and grain size for the sintered two blends. According to Eq. (3), the expected trend for densification is that the density increases with the sintering temperature. However, Blend #2 displayed a decreased value of densification from 99.5% at 1800 ^{o}C to 98.2% at 1900 ^{o}C. This could be caused by a local high temperature state, which led to the vaporization or melting of the surfaces of the SiC particles, or even damage of the CNTs during the SPS process. With the addition of TaC, Blend #1 just obtained the densification of 98.6% at 1900 ^{o}C. It is suggested that a higher sintering temperature be applied for Blend #1 in order to achieve full densification because of the ultra high melting point of TaC (3800 ^{o}C). Increasing the SPS temperature from 1700 to 1900 ^{o}C caused the average grain size to increase from 1.97 to 2.43 um for Blend #1, and from 1.82 to 2.55 um for Blend #2. The increasing grain growth may be due to the mass transport mechanism involved in the SPS process. As the temperature increases, the driving force that promotes neck growth increases, which gives rise to grain growth. Therefore, too high a sintering temperature would result in rapid grain growth, which competes with densification and prevents the achievement of full density.

Fig. 2-14 displays young's modulus and hardness as a function of sintering temperature for the two blends. Raising the SPS temperature from 1700 to 1800 $^{\circ}$C led to the increase of both young's modulus and hardness for the two blends, owing to the better densification of samples. When increasing the temperature from 1800 to 1900 $^{\circ}$C, however, Blend #1 and Blend #2 showed different trends in mechanical properties than those which had been found in densification. It can be noticed that young's modulus and hardness slightly increased for Blend #1 while it clearly decreased for Blend #2 in this temperature range. It is indicated that Blend #2 was very sensitive to sintering temperature after it achieved a nearly full densification in 1800 $^{\circ}$C, with a high possibility that some CNTs got damaged.

(a)

(b)
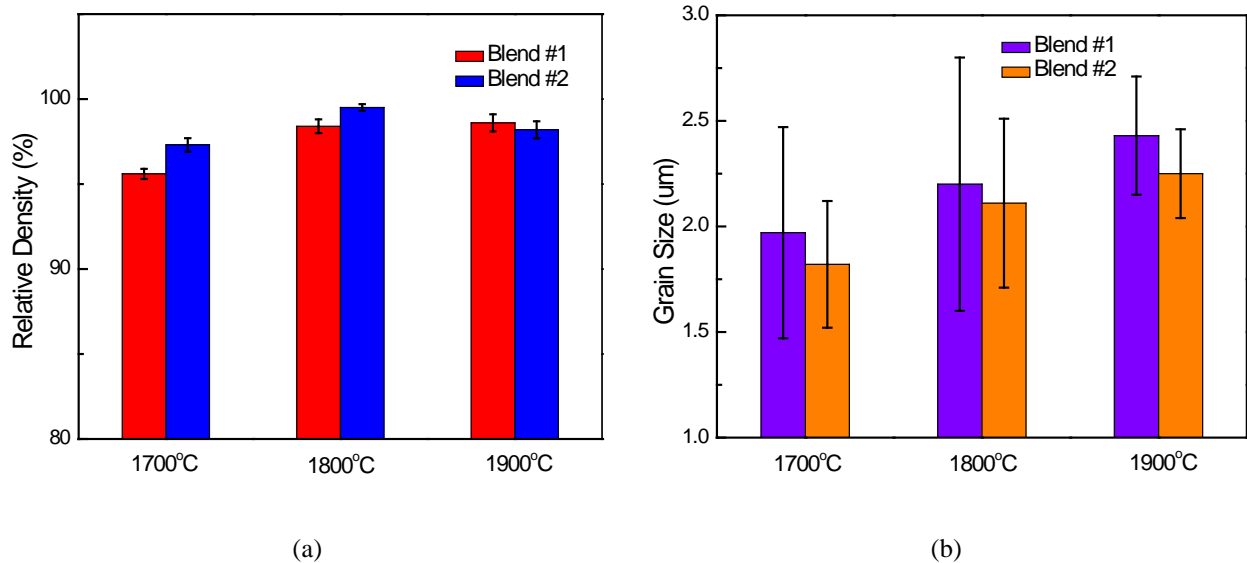
Fig. 2-13 (a) Relative density and (b) Grain size of SiC-based ceramics as a function of maximum heating temperature
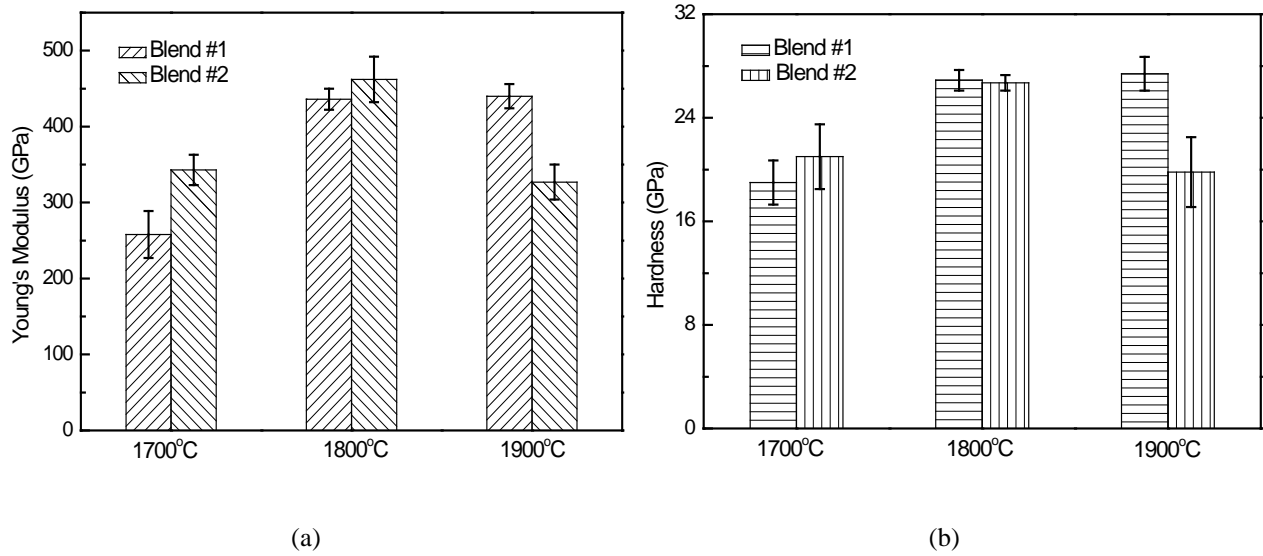
Fig. 2-14 (a) Young's modulus and (b) Hardness of SiC-based ceramics as a function of maximum heating temperature

2.3.4 Effect of maximum uniaxial applied pressure

As in the SPS process, temperature plays a dominant role and is the most important parameter. Yet the effect of pressure is often underestimated and has not been systematically investigated. Pressure can also play a key role by influencing the driving force for sintering or by introducing other densification mechanisms such as particle rearrangement and grain sliding. The relationship of densification and driving force is giving by [151],

$$\frac{d\rho}{(1-\rho)dt} = B(g\frac{\gamma}{x} + P) \tag{4}$$

where ρ is relative density, t is time, B is a term consisting of diffusion coefficient and temperature, g is geometric constant, γ is surface energy, x is particle size, and P is the applied sintering pressure. To investigate the influence of temperature in the SPS sintering of SiC-based ceramics, powders were processed under maximum sintering pressures of 50, 70 and 90 MPa, respectively, with a heating rate of 133 ^{o}C/min and a maximum sintering temperature of 1800 ^{o}C.

Fig. 2-15 shows the variation of densification and grain size with different applied pressures. Both Blend #1 and Blend #2 experienced an increase in relative density with an increase of sintering pressure, which indicated that pressure indeed has a significant effect on densification by impacting the driving force of sintering as predicted by Eq. (4). However, pressure also has an inverse effect on the diffusion coefficient, and the relationship is expressed as [152]:

$$\left[\frac{\partial lnD}{\partial P}\right]_T = -\frac{\Delta V}{kT} \qquad (5)$$

where D is the diffusion coefficient, P is the applied sintering pressure, ΔV is the activation volume for diffusion, k is Boltzmann's constant, and T is the absolute temperature. It is deducted from this equation that the increase of pressure would reduce the diffusion coefficient of the sintered compacts. The increase of grain size with increased pressure revealed that pressure restrained particle diffusion to get finer grains to some extent.

Fig. 2-16 depicts the pressure dependence of young's modulus and hardness for Blend #1 and Blend #2. Both blends exhibited an increase in mechanical properties, with increased sintering pressure. Blend #1 achieved an increment of 30 GPa in young's modulus and 5.9 GPa in hardness, while Blend #2 obtained a growth of 28 GPa in young's modulus and 6.4 GPa in hardness. It is believed that the applied sintering pressure has a positive effect on the densification by providing the driving force. This driving force helps to increase the contact area between particles and decrease the temperature gradient across the compacts, which generates high densified samples with a fine grain size and improved mechanical properties.

| | |
| (a) | (b) |
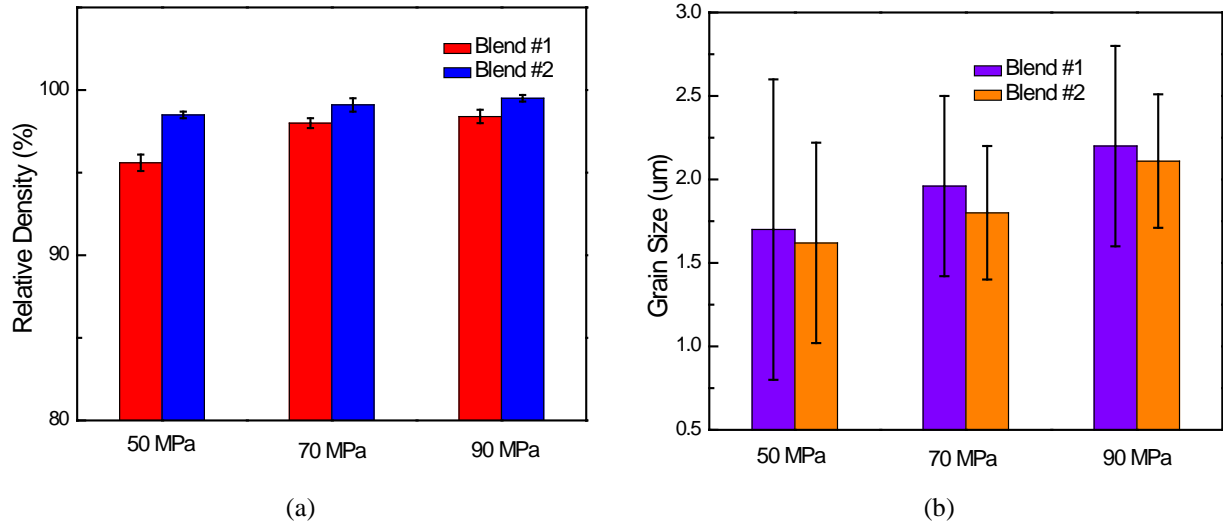
Fig. 2-15 (a) Relative density and (b) Grain size of SiC-based ceramics as a function of maximum applied pressure

| | |
| (a) | (b) |
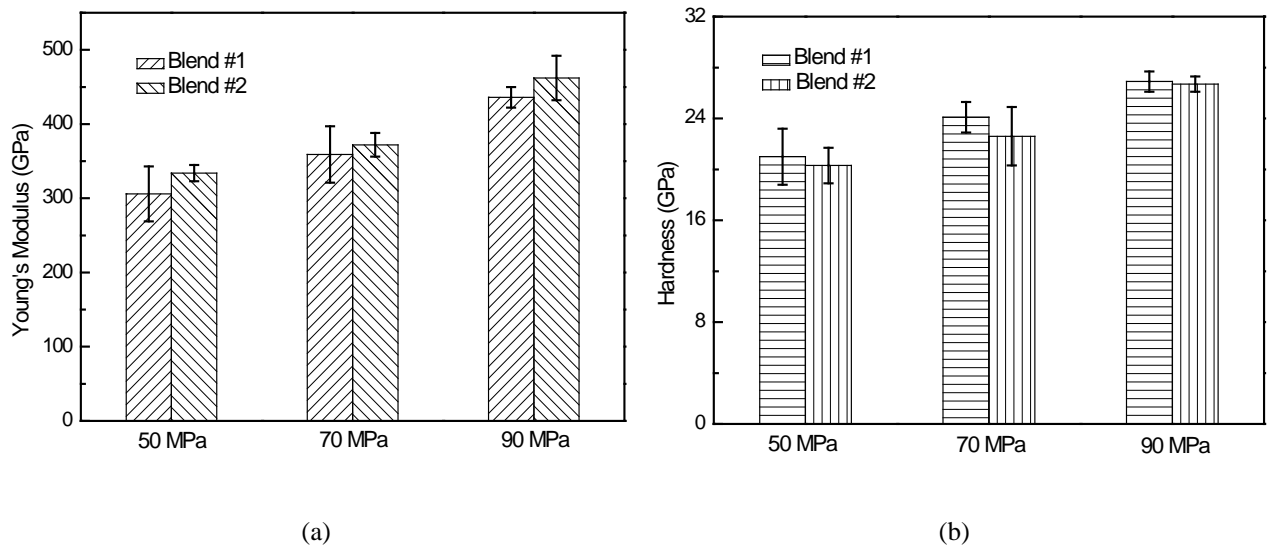
Fig. 2-16 (a) Young's modulus and (b) Hardness of SiC-based ceramics as a function of maximum applied pressure

2.4 CONCLUSIONS

TaC and/or CNTs reinforced SiC ceramics were successfully sintered using the spark plasma sintering technique. Ultrasonic treatment was observed to be an effective way to distribute CNTs homogeneously into the SiC matrix. The addition of CNTs increased the

47

densification of SiC from 86% to 99.5% while still maintaining submicron grain size under the sintering parameters of 133 ^{o}C/min heating rate, 1800 ^{o}C maximum temperature and 90 MPa maximum pressure. The increased densification could be due to the uniform distribution of CNTs along the grain boundaries of SiC occupying the pores, as well as the excellent thermal conductivity of CNTs that reduces the thermal gradient. The better densification, in turn, helped achieve better mechanical properties for the SiC-based composites. Detailed analysis of punch displacement curves revealed that TaC additives did not favor the densification of CNT/SiC ceramics owing to the larger size of TaC and low self-diffusion coefficient; however, TaC increased the hardness of the composites to some extent.

The increase of heating rate gave rise to worse densification for both the TaC and/or CNTs reinforced SiC ceramics, thus a negative effect in young's modulus and hardness, as rapid heating rate may cause local temperature gradients and local uniformity. However, a higher heating rate had a clean effect on the mobility of the grain boundaries, which inhibited the grain growth. CNTs/SiC ceramics achieved a nearly full densification at an 1800 ^{o}C sintering temperature, but higher temperatures resulted in rapid grain growth and deteriorated mechanical properties. While, for TaC/CNTs/SiC ceramics, 1800 ^{o}C was not sufficient to get full densification due to the higher melting point of TaC. Raising the sintering pressure brought about increased densification with improved mechanical properties for both the composites by influencing the driving force for sintering. However, too high a pressure could have an inverse effect on the diffusion coefficient, which caused the growth of grain size.

3.0 THE EFFECT OF TAC REINFORCEMENT ON THE OXIDATION OF CNTS/SIC CMCS

3.1 INTRODUCTION

Given the promising applications of CNTs/SiC CMCs in high temperature applications, it would be of great interest to understand the oxidation mechanism by adding the TaC additives to the CNTs/SiC composites. Thus, for the framework proposed in 1.3.2, this chapter is built to investigate the oxidation mechanism of SiC based CMCs with CNTs reinforcement, and how the TaC additives will affect the thermal oxidation resistance of the SiC-CNTs-TaC systems. Groups of TaC and/or CNTs reinforced ceramics are prepared through spark plasma sintering (SPS). The oxidation behavior up to 1500 $^{\circ}$C is characterized in terms of mass changes, oxide layer formation and thickness. TGA, XRD, Raman spectroscopy and SEM/EDS are carried out to study the structure of the oxides that are formed during oxidation.

SiC ceramic matrix composites (CMCs) have been recognized as promising materials for high temperature structural applications such as fusion reactors and aerospace engines where unique combinations of high strength at elevated temperatures, good oxidation resistance, high thermal shock resistance, and creep resistance are required. The oxidation mechanism of SiC has been studied extensively [52-53, 153]. When SiC is exposed to air at elevated temperatures, SiO_2 and CO are formed according to the following reaction.

$$SiC\ (s) + 3/2\ O_2\ (g) = SiO_2\ (s) + CO\ (g) \tag{1}$$
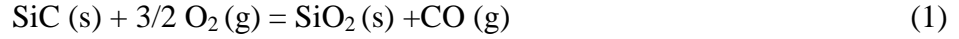
SiC begins oxidizing between 600 $^\circ$C and 800 $^\circ$C, forming a glassy SiO_2 layer that separates the oxygen from the ceramic base [154]. The protective SiO_2 layer shows the lowest permeability to oxygen of all the common oxides, and its properties are affected by the structural changes of SiO_2 [155-156]. The best protective effect provided by the glassy SiO_2 is around 1200 $^\circ$C, however, SiO_2 tends to be lost by evaporation or active oxidation at higher temperatures in a flowing environment [157]:

$$SiC\ (s) + 2\ SiO_2\ (g) = 3\ SiO\ (g) + CO\ (g) \tag{2}$$

Attempts have been made to improve the oxidation resistance through SiC ceramic coatings or SiC/Si additives for high temperature applications. Nayak et al. [158] coated Multi-walled carbon nanotubes (MWCNTs) with SiC and reported a higher stability of the modified MWCNTs as compared to the unmodified ones. Work done by Song et al. [159] also revealed that the onset oxidation temperature increased from 540 $^\circ$C to 700 $^\circ$C for the SiC-coated MWCNTs by thermogravimetric analysis (TGA). Zeman et al. [160] investigated the high-temperature resistance of ternary Ta-Si-N films with a more than 20 at.% Si content, and stated that an excellent oxidation resistance, in flowing air up to 1300°C, was achieved. Opila et al. [161] tested the oxidation resistance of hot pressed ZrB_2-20 vol% SiC samples at 1327°C and 1627 $^\circ$C, and identified a 150 μm thick protective silica layer at 1627 $^\circ$C. In a later work on Ta additions to the oxidation resistance of ZrB_2-20 vol% SiC and HfB_2-20 vol% SiC based ceramics, Opila et al. [162] observed that $TaSi_2$ additions lowered the oxidation rate at 1627 $^\circ$C, which was attributed to the phase separation in the amorphous surface layer.

Available studies on the oxidation mechanism of TaC are very scarce. It is known that TaC oxidizes to form Ta_2O_5 at temperatures as low as 400 $^\circ$C [163], following the reaction:

$$4\ TaC\ (s) + 7\ O_2\ (g) = 2\ Ta_2O_5\ (s,\ l) + 4\ CO\ (g) \tag{3}$$
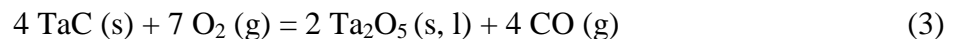
Wang et al. [63] carried out research on oxidation behavior of hot pressed ZrB_2-SiC-TaC ceramics in a vacuum environment with the temperature range from 1200 ^{o}C to 1500 ^{o}C, and found that low concentrations of TaC (10 vol%) exhibited deteriorated oxidation resistance while higher TaC concentrations showed enhanced oxidation resistance. The deterioration of oxidation resistance could come from the chemical reaction between the oxidized Tantalum (Ta_2O_5) and ZrO_2 to form the solid solution, with not enough Ta_2O_5 to protect the bulk materials. Peng et al. [8] reported that the interior layer covered by the glassy SiO_2 protective layer was less porous in Ta-containing composites.

3.2   EXPERIMENTAL PROCEDURE

3.2.1   Oxidation test

Prior to oxidation, samples were ground and cut into $4\times4\times6$ mm^3 bars and cleaned in an ultrasonic bath with acetone. Isothermal oxidation behaviors were investigated at 800 ^{o}C and 1200 ^{o}C using Thermogravimetric analysis (TGA, Simultaneous Symmetric Thermoanalyser, SETARAM, Caluire, France). Specimens were supported by an alumina crucible hung in the furnace, and heated to the setting temperature of 800 ^{o}C and 1200 ^{o}C, respectively, at a heating rate of 10 ^{o}C/min by exposure to flowing air from a compressed air tank with a flow rate of 0.1 L/min for 2 hours. After oxidation, the samples were cooled down in flowing high purity argon. As the temperature of the available TGA system cannot go beyond 1200 ^{o}C, a horizontal tube furnace (Carbolite, STF 15/450, UK) was employed to carry out the isothermal oxidation test at 1500 ^{o}C. Specimens were placed on an alumina plate, and inserted into the center of the furnace

and leveled. The ends of the tube were sealed with gas-tight end caps. A flowing atmosphere of air was maintained at the flowing rate of 10 mL/min. Specimens were heated at 5 ^{o}C/min to 1500 ^{o}C with a holding time of 2 hours, and cooled down in the furnace at ~3 ^{o}C/min. The weight of each sample was measured before and after oxidation to determine the weight change, this accomplished by a balance with accuracy of 0.01 mg (Mettler Toledo, AB135-S/FACT).

3.2.2   Materials characterization

X-ray diffraction (XRD) analysis was carried out to identify different phases in the specimens using a Bruker D8 Discover X-ray Diffractometer operated with Cu-Kα X-rays (λ=1.54178 Å) at a scan rate of 1°/min. Raman spectroscopy (Renishaw, inVia Raman system) was carried out on the sintered and oxidized samples to study the structural quality of CNTs with 633 nm laser excitation and 17 mW laser power. Cross sections of the oxidized samples were prepared by grinding and polishing them to a 1 μm finish using SiC polishing papers and diamond abrasives. The microstructures of oxidized samples were examined by scanning electron microscopy (SEM, JEOL JSM-6510LV) and energy dispersive spectrometry (EDS, OXFORD INCA EDS system). The thickness of oxidized layers was measured using the software Image J (U.S. National Institutes of Health, Bethesda, MD).

3.3   RESULTS AND DISCUSSION

Using a simple rule of mixtures and taking the density of 3.216 g/cm^3 for SiC, 2.1 g/cm^3 for CNTs, 13.9 g/cm^3 for TaC, and 2.51 g/cm^3 for B$_4$C, the theoretical densities of SiC-4 wt%

CNTs-4 wt% TaC-1 wt% B_4C (Blend #1) and SiC-4 wt% CNTs-1 wt% B_4C (Blend #2) should

be 3.237 g/cm^3 and 3.140 g/cm^3, respectively. The measured bulk densities of the SPS sintered

Blend #1 ranged from 3.175 g/cm^3 to 3.195 g/cm^3, while Blend #2 varied from 3.118 g/cm^3 to

3.130 g/cm^3. All of the specimens were sintered to near theoretical density (>98%), with no

indication of open porosity. Based on the high relative density achieved and the lack of open

porosity, porosity should not have a significant influence on the oxidation behavior. Fig. 3-1

presents the polished cross sections of the sintered ceramics. According to the EDS analysis (Fig.

2-5), it can be identified that the grayish white phase is SiC, while the white and dark phases are

TaC and B_4C, respectively.

<table>
<tr><td>(a)</td><td>(b)</td></tr>
</table>
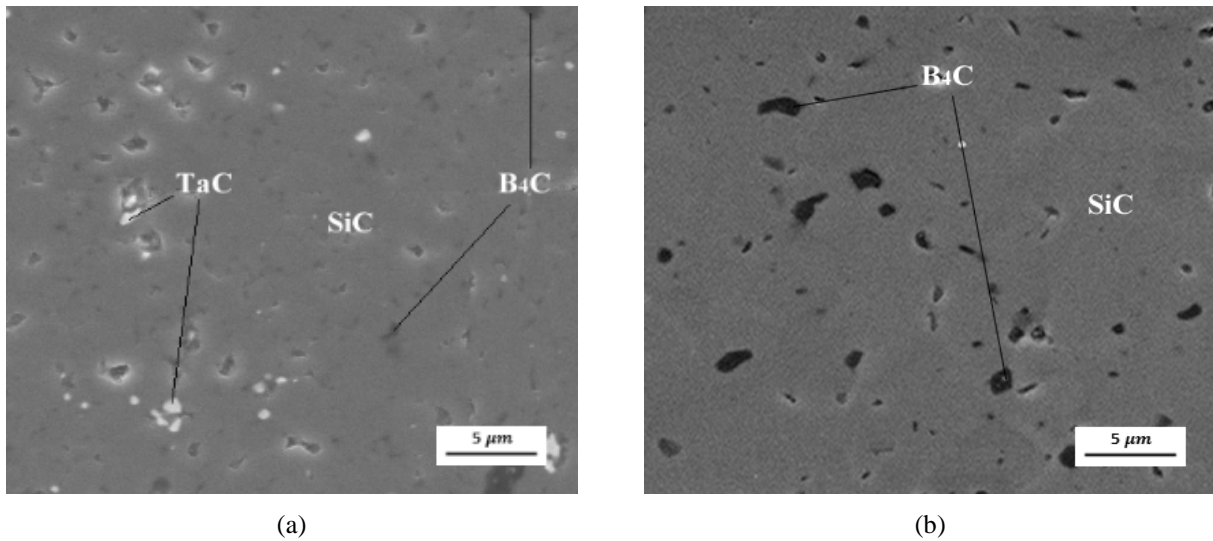
Fig. 3-1 SEM micrograph of the polished cross sections of the as sintered ceramics (a) Blend #1, and (b) Blend # 2

The relative weight changes of Blend #1 and Blend #2 samples were recorded by TGA

due to their oxidation in flowing air, and presented in Fig. 3-2. Samples were heated to 1200 ^{o}C

in air, maintained for 2 hours, and subsequently cooled down to room temperature. A mass loss

occurred at the temperature around 460 ^{o}C and stopped at 800 ^{o}C for Blend #2, which can be

attributed to the oxidation of CNTs. In inert atmosphere, CNTs are stable up to about 2700°C, while in air they readily oxidize at temperatures below 700 °C. The oxidation temperature varies with the type, structural defects and purity of CNTs [164-165]. By contrast, the onset oxidation temperature for Blend #1 was 550 °C. After a slight mass decrease, Blend #1 started to gain weight at 665 °C and peaked at 750 °C, this followed by a notable mass loss through until 883 °C. Such a delayed oxidation temperature for CNTs demonstrated the effective reinforcing influence of TaC on CNTs/SiC ceramic. The oxidation temperature for TaC is above 500°C, and the oxidized TaC on the CNT surfaces could protect the CNTs from oxygen, resulting in an increased oxidation temperature [166]. Since the oxidation of CNTs led to weight loss while Ta_2O_5 formation from TaC oxidation led to weight gain, the overall weight change of Blend #1 below 883 °C was determined by the kinetics of these two reactions. The total relative weight loss through 883 °C was approximately 0.050% for Blend #1, which was less than that for Blend #2 (0.065%), oxidized up to 800°C. After the weight decrease, both blends experienced mass growth ultil the oxidation test stopped at 1200 °C. This weight increase indicated that SiC started to oxidize to form SiO_2. The relative weight change between 883-1200 °C for Blend #1 was 0.016%, while for Blend #2 it was 0.020%, ranging from 800-1200 °C. Therefore, it can be concluded from TGA measurements that TaC showed an enhanced protective effect in retarding the oxidation temperature for CNTs, as well as reducing the weight change originated from SiC oxidation.
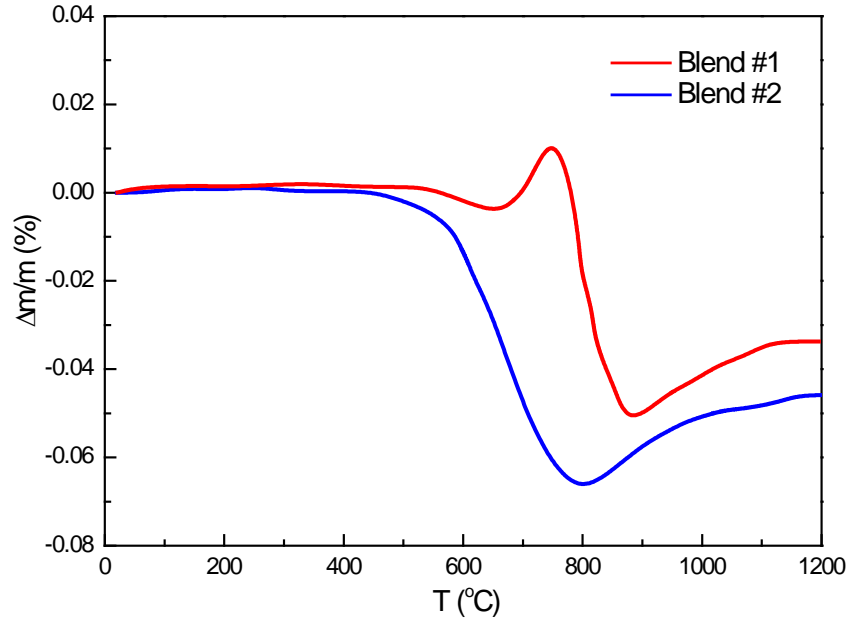
Fig. 3-2 TGA curves of the two ceramic composites oxidized in air up to 1200 ^{o}C with a ramp 10°C/min

To confirm the analysis based on TGA curves and better understand the oxidation mechanisms, oxidation tests were conducted at the same conditions by TGA at 600 ^{o}C and 800 ^{o}C for Blend #1, and at 400 ^{o}C and 800 ^{o}C for Blend #2. Since the oxidation resistance of SiC is provided by a protective glassy SiO_2 layer, which shows the best protective effect at ~1200 ^{o}C, above that temperature SiO_2 gets crystallized or lost by evaporation or active oxidation. Thus, it would also be of great interest to discover the oxidation mechanism at temperatures higher than 1200 ^{o}C. Oxidation tests were carried out at 1500 ^{o}C for both blends in a horizontal tube furnace.

Phase structures of the oxidized surfaces were investigated by means of X-ray diffraction. The development of XRD patterns for samples oxidized at increasing temperatures, as compared to those non-oxidized ceramic composites of Blend #1 and Blend #2, are shown in Fig. 3-3. For the two non-oxidized samples, XRD patterns are identical, except for the TaC phase in Blend #1, and no visible oxides can be found in both blends. It is worth mentioning that 6H SiC (α-SiC) was identified by XRD, and since the starting silicon powder was pure 3C SiC (β-SiC), which

55

means that α-SiC was formed during SPS process. This is due to the fact that cubic β-SiC becomes unstable at temperatures higher than $1500^{\circ}C$ and β→α transformation begins [167-168].

X-rays are scattered in many directions on amorphous phases, leading to a large bump distributed in a wider range instead of high intensity peaks [169]. Silica was detected as the amorphous phase under the 400 $^{\circ}C$ oxidation condition for Blend #2, but no similar bump manifested on the XRD pattern for Blend #1, oxidized at 600 $^{\circ}C$. It can be noticed from the 600 $^{\circ}C$ oxidation curve that some unknown small peaks appeared in the 2θ range of $20^{\circ}\sim25^{\circ}$, which may be an indication of reaction products of the crystal oxides from TaC. As for the XRD patterns obtained by samples oxidized at 800 $^{\circ}C$, both blends showed a high intensity bump of amorphous SiO_2, denoting that SiC oxidized extensively; Blend #1 presented a bump with lower intensity, next to the SiO_2 bump, which confirmed that TaC was oxidized to form amorphous Ta_2O_5 under 800 $^{\circ}C$. When increasing the oxidation temperature to 1200 $^{\circ}C$, the glassy SiO_2 bumps were still retained for both ceramics. Meanwhile, the diffraction bump of amorphous Ta_2O_5 phase in Blend #1 showed a tendency of crystallization. However, clear diffraction peaks of SiO_2 and/or Ta_2O_5 displayed on the XRD patterns of samples oxidized at 1500 $^{\circ}C$ for Blend #1 and Blend #2, respectively. It can be deduced that the protective glassy SiO_2 layer is effective at least up to 1200 $^{\circ}C$, while it may degrade under 1500 $^{\circ}C$ for the as sintered ceramic composites. Meanwhile, the diffraction peaks of SiO_2 and SiC in Blend #1 were slightly shifted to lower 2θ values compared with those in Blend #2, suggesting the formation of Ta-doped solutions [170].
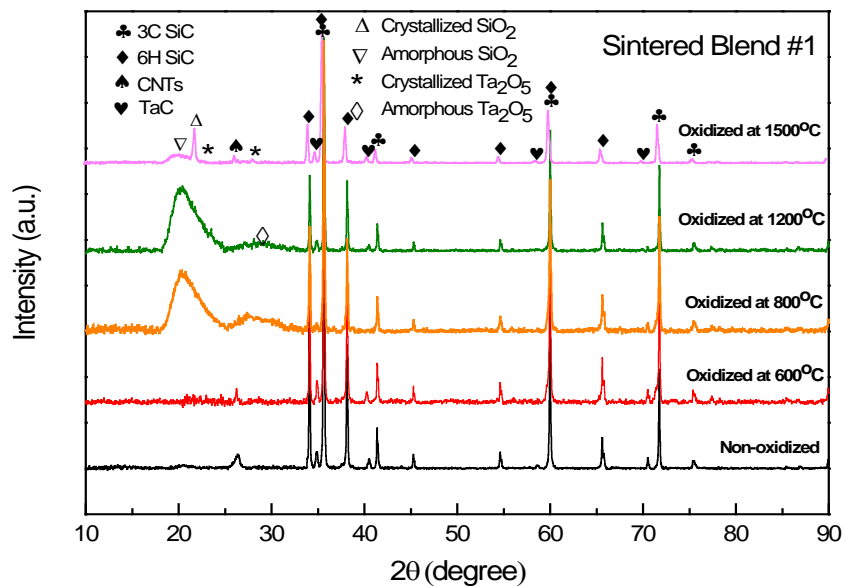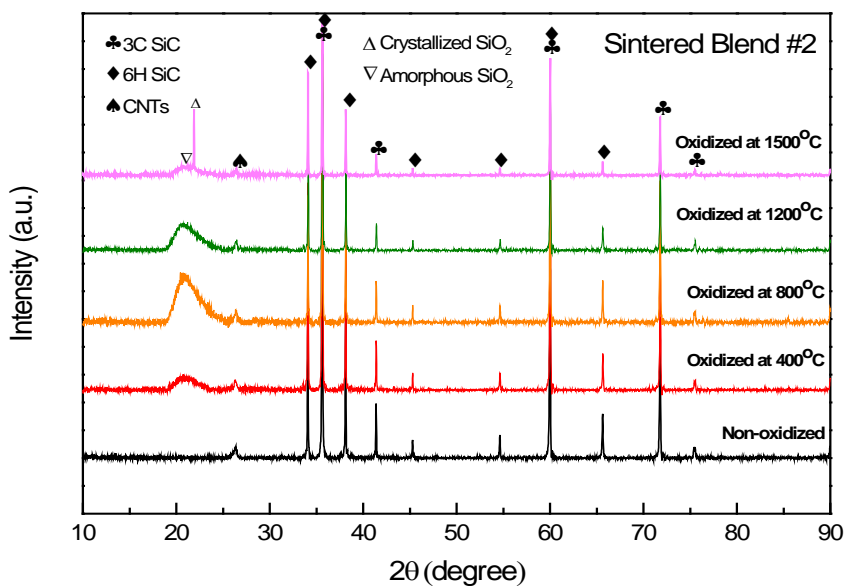
Fig. 3-3 XRD patterns of the ceramic composites non-oxidized and oxidized in air to difference temperatures (a) Blend #1, and (b) Blend #2

Raman spectroscopy has been shown to be a powerful and nondestructive technique for the characterization of the structural stability of CNTs based composites. Raman peaks for free multi-walled CNTs are generally observed at D band (~1342 cm^{-1}), G band (~1580 cm^{-1}), D'

band (~1620 cm^{-1}), and G' band (~2700 cm^{-1}) [171-172]. The D band is activated by the presence of disorder in the sp^2 carbon system and will not be seen in perfect graphite. The G band is assigned to the in-plane stretching of a C-C bond with a shoulder of D' band. The G' band is the second overtone of the defect-induced D band, which is diameter-dependent and does not require defects. Fig. 3-4 depicts the Raman spectra of the as sintered two blends of ceramic composites and their oxidized samples from multi-walled CNTs. The peak positions of D, G, and D' bands, as well as the ratio of the intensity of the D band and G band (I_D/I_G), are listed in Table 3-1. The as sintered non-oxidized two ceramics showed the same peak values for the D (1343 cm^{-1}), G (1586 cm^{-1}), and D' (1620 cm^{-1}) bands. Compared with the free multi-walled CNTs, the G peak of CNTs in SiC based ceramics exhibited a blueshift (an increase in frequency), indicating that the CNTs were subjected to compressive stresses from heat, pressure, and electric current during SPS [5]. For both blends of the oxidized samples, the G peak shifted to higher frequency, while the D peak slightly shifted to a lower frequency (redshift), with an increasing oxidation temperature. This significant blueshift of the G band can be understood as the increased thermal expansion in the lattice, which causes the residual compressive stress on the CNT network as imposed by the ceramic matrix during the heating and oxidation process [173-175]. The 4 cm^{-1} lowering of the D peak frequency at a 1500 ^{o}C oxidation temperature may be induced by the increase of average distance between defects and disorder [176-177]. Another observation from the Raman spectra was that the D and G bands got broader with increased oxidation temperatures, owing to higher disorder in CNTs [178].

The ratio of I_D/I_G is a good indicator of the disorder of carbon networks. In the purified CNTs reinforced samples, the D band is weaker [179]. As the oxidation temperature increased, the D peak gradually increased, and its height was less than that of the G peak for both blends.

Ratio values of I_D/I_G were very close for the as sintered Blend #1 (0.82) and Blend #2 (0.83), which means that CNTs had the same structural condition after SPS. However, Blend #2 presented a larger I_D/I_G value for each oxidized temperature, compared to that of Blend #1. It can be concluded that more disorder occurred in the CNTs network with higher oxidation temperatures, while the CNTs in Blend #1 were less disordered, implying that Blend #1 possessed better oxidation resistance than Blend #2.
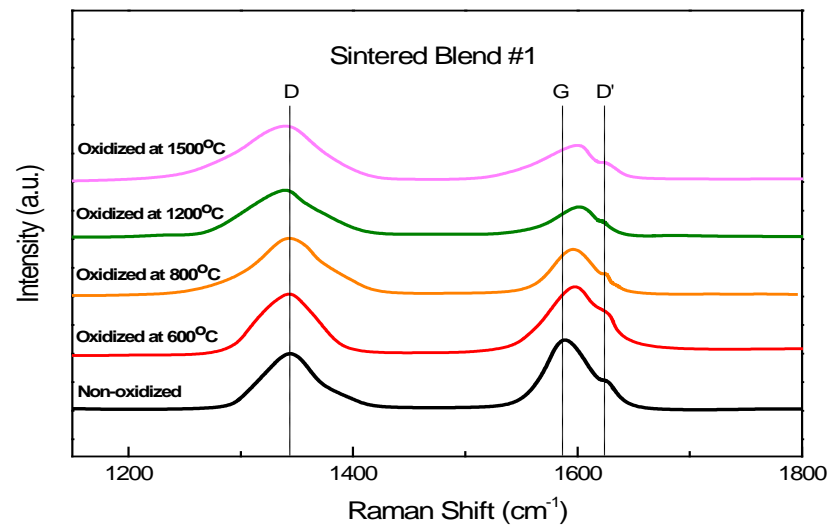
(a)
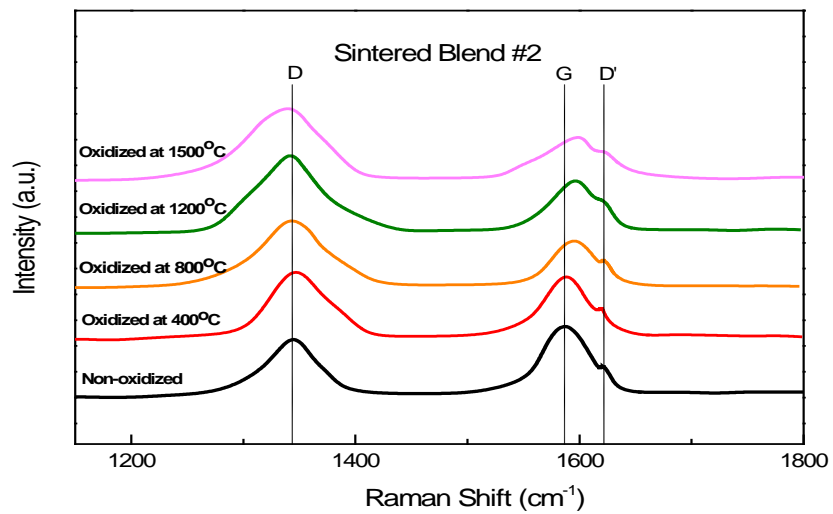
(b)

Fig. 3-4 Raman spectra showing the D, G and D' bands from multi-walled CNTs in (a) Blend #1, and (b) Blend #2

Table 3-1 Raman spectra peak data from CNTs of the SPS ceramics and their oxidized samples

Material	D-peak	G-peak	D'-peak	I_D/I_G
Blend #1_Non Oxidized	1343	1586	1620	0.82
Blend #1_600^{o}C	1343	1596	1620	0.93
Blend #1_800^{o}C	1343	1596	1620	1.25
Blend #1_1200^{o}C	1339	1600	1620	1.47
Blend #1_1500^{o}C	1339	1602	1620	1.56
Blend #2_Non Oxidized	1343	1586	1620	0.83
Blend #2_400^{o}C	1343	1589	1620	1.08
Blend #2_800^{o}C	1343	1595	1620	1.42
Blend #2_1200^{o}C	1342	1596	1620	1.54
Blend #2_1500^{o}C	1339	1601	1620	1.62

The variation of the thickness of the oxidized layer with temperature can be indicative of the oxidation mechanism. Fig. 3-5 shows the SEM images of the layered cross sections of the ceramic samples oxidized at 800 ^{o}C. Generally, three layers could be identified for each oxidized cross section, which were the severely oxidized outer layer, the less oxidized middle layer and the inner base material according to the EDS analysis (Fig. 3-5(c) and (d)). The outer layer was a very thin SiO_2 layer with a small amount of SiC (~1.6 μm) for Blend #2, and embedded with amorphous Ta_2O_5 (~1.8 μm) for Blend #1. The thickness of the less oxidized layer was ~9.8 μm for Blend #1 and ~9.7 μm for Blend #2. The high oxidation resistance of Blend #2 was attributed to the growth of a protective film, which largely decreased the oxygen diffusion towards the bulk material. On the other hand, TaC was oxidized to form Ta_2O_5 in Blend #1, and this amorphous Ta_2O_5 was also thought to act as an effective barrier to oxygen. Furthermore, transition metal carbides show good thermal and electrical conductivity, owing to their metallic nature. The enhanced thermal conductivity of TaC led to decreased thermal gradients while the formation of SiO_2 inhibited the penetration of oxygen.
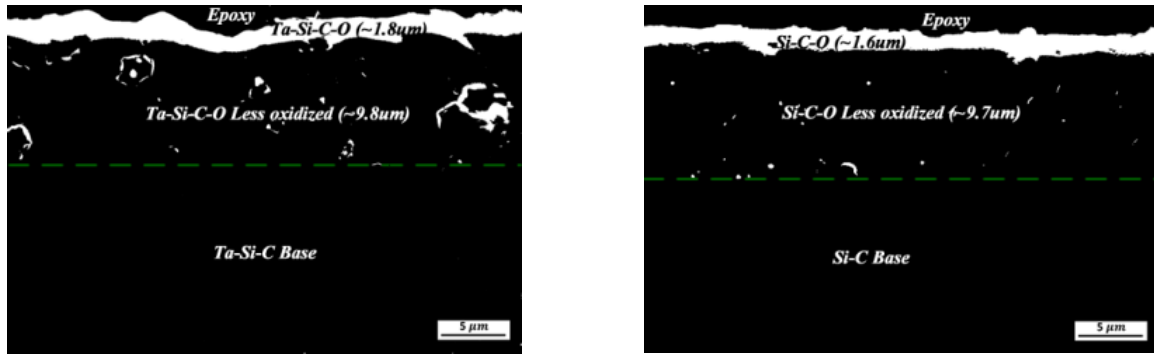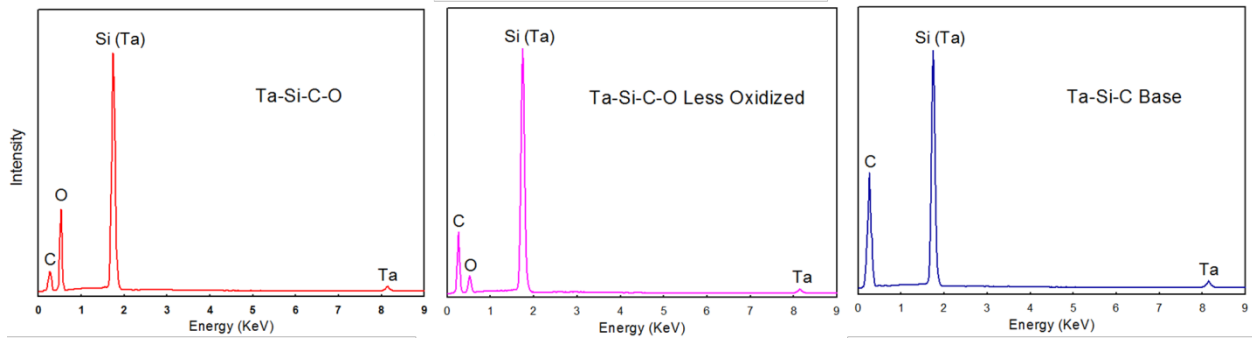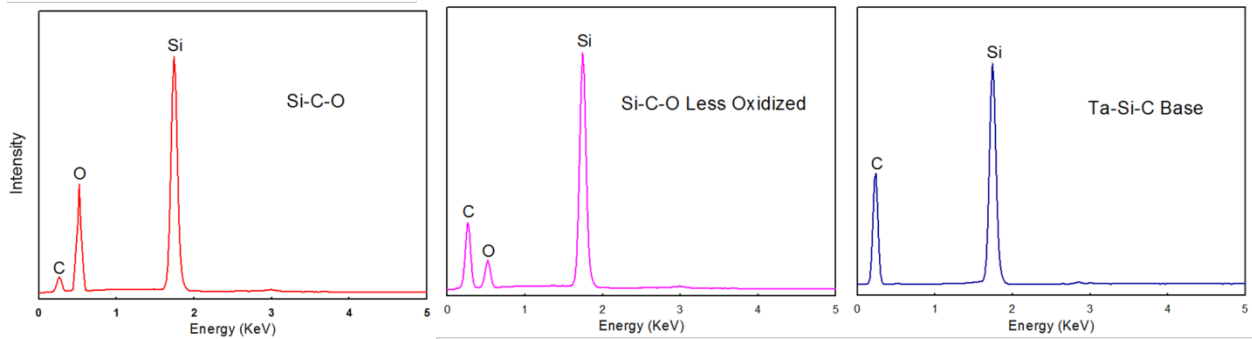
Fig. 3-5 SEM images showing layered cross sections of oxidized ceramics at 800°C (a) Blend #1, (b) Blend #2, (c) EDS of different layers for Blend #1, and (d) EDS of different layers for Blend #2

The SEM and EDS analysis gave clear evidence on the formation of oxidized layers on the ceramic samples' exposure to air at 1200 °C. As shown in Fig. 3-6, there is a dense oxidized outer layer containing SiO_2 and Ta_2O_5 (~3.3 μm), and a less oxidized layer (~10.3 μm) adjacent to the base material in Blend #1. In contrast, the oxidized outer layer in Blend #2 was ~3.6 μm, with SiO_2 as the major phase, but more carbon in comparison to the sample oxidized at 800 °C.

61

The thickness for the next less oxidized layer was ~12.9 μm, which was 2.6 μm thicker than that of Blend #1. The more oxidized layer in Blend #2 may be due to the porosity formed in the outer layer by the evolution of CO and/or CO_2 during the oxidation process. When Blend #1 oxidized at 1200 ^{o}C, amorphous crystalized (seen in Fig. 3-3). According to Wang et al. [173], the crystalized Ta_2O_5 grew with a preferred orientation giving rise to the phase separation in the glassy protective layer, which was reported to increase the viscosity of the glassy layer and lower the oxygen permeability through the layer. The specialized Ta_2O_5 and SiO_2 layer acted as an effective barrier to the transport of oxygen, leading to the improved oxidation resistance for Blend #1.

(a)

(b)

(c)

(d)
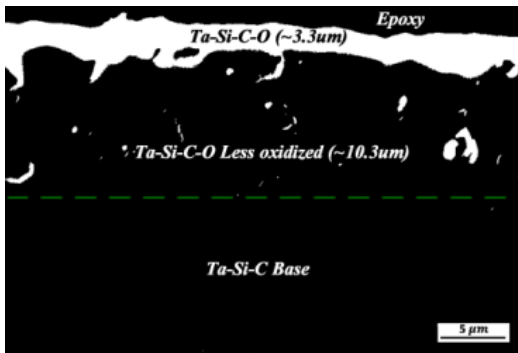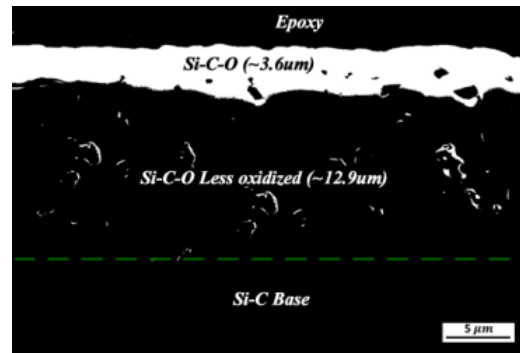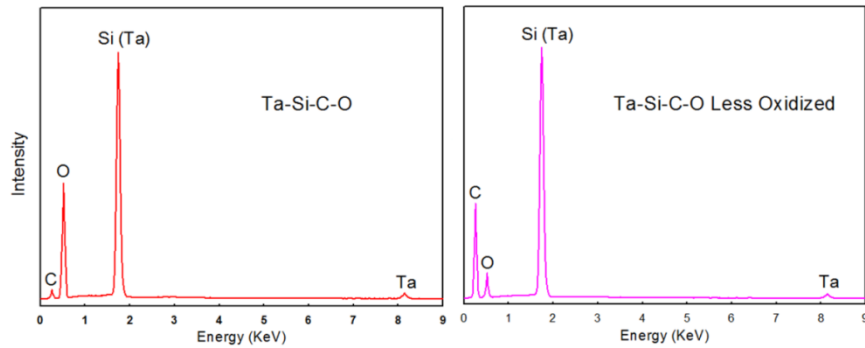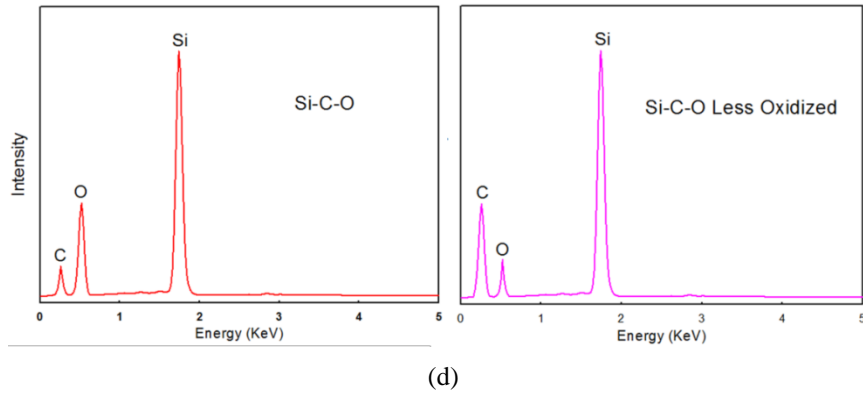
Fig. 3-6 SEM images showing layered cross sections of oxidized ceramics at 1200°C (a) Blend #1, (b) Blend #2, (c) EDS of different layers for Blend #1, and (d) EDS of different layers for Blend #2

Fig. 3-7 shows the SEM images and EDS analysis of the layered cross sections of the ceramic samples oxidized at 1500 °C. Three distinct layered structures could also be found in the cross sections of each sample: the oxidized outer layer was ~4.7 μm for Blend #1 and ~4.1 μm for Blend #2, and the less oxidized layer grew up to 14.3 μm for Blend #1 and 14.8 μm for Blend #2 and the base material layers. As can be seen in Fig. 3-7(b), the oxidized outer layer in Blend #2 had a more porous structure with a lager amount of carbon as compared with the sample oxidized at 1200 °C. Based on the XRD results in Fig. 3-3, the amorphous SiO_2 scale transformed to a crystalized structure at an oxidizing temperature of 1500 °C, which provided the penetration paths for oxygen. Another oxidation mechanism reducing the effectiveness of the SiO_2 barrier could be the active oxidation of SiC to form SiO (Eq. (2)), which can lead to rapid material loss [180]. With the increased oxidizing temperature for Blend #1, Ta_2O_5 crystals were performing the solid phase sintering driven by the increased surface energy from crystallization. Meanwhile, the volume shrinkage started which gave rise to the formation of small cracks and voids, providing the access to further oxidation [181]. The Ta-doped SiO_2 solution, suggested by XRD results in Fig. 3-5, changed the oxidation mechanism from phase separation to the oxygen solution and diffusion mechanism in the melt [173]. The cracks shown in Fig. 3-7(a), were

63

probably caused by the above mentioned volume shrinkage of stress concentration, and might also arise from grinding during sample preparation, which was due to the fact that the less oxidized layer in Blend #1 was thinner than that shown in Blend #2.

(a)

(b)

(c)

(d)
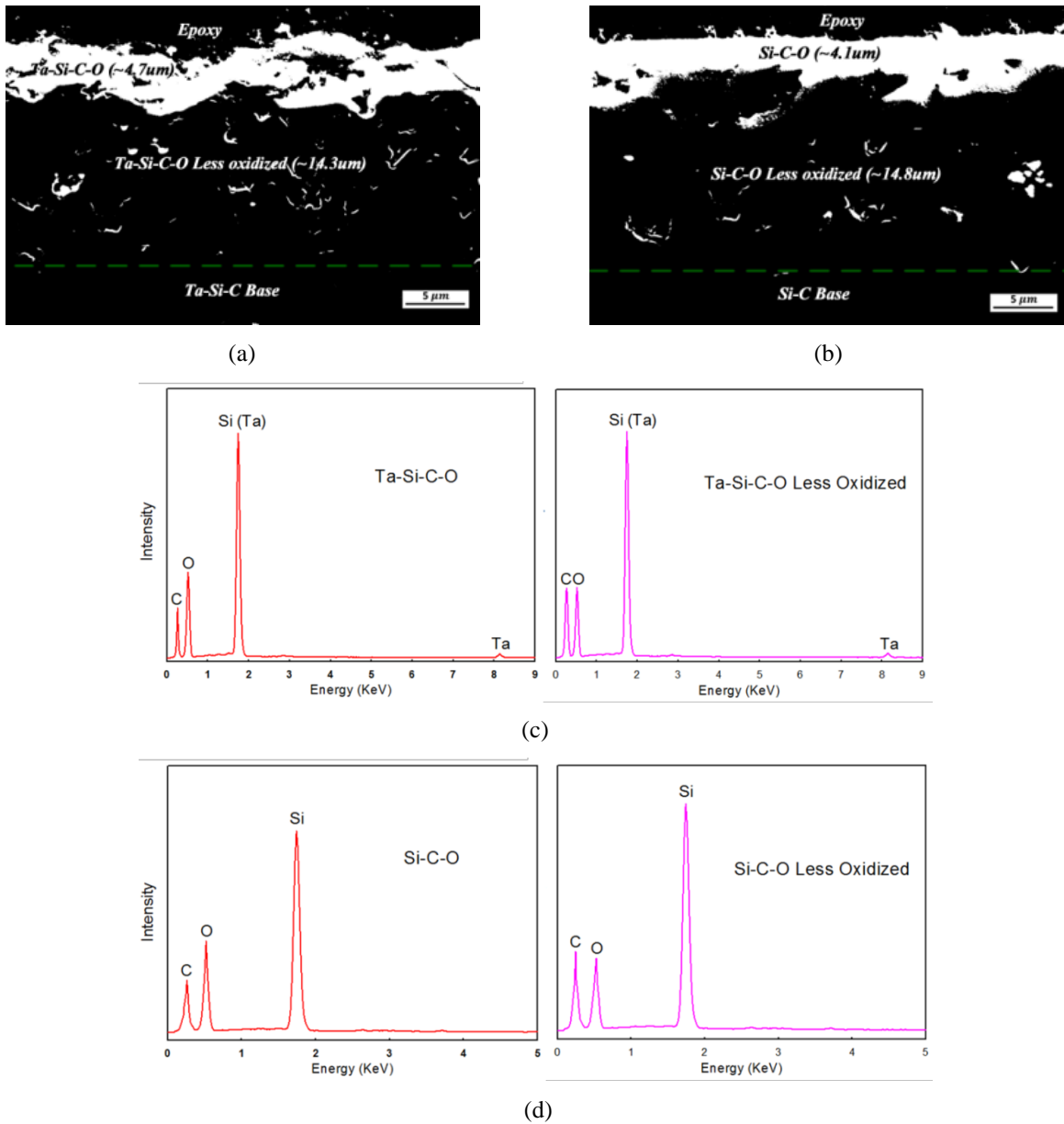
Fig. 3-7 SEM images showing layered cross sections of oxidized ceramics at 1500°C (a) Blend #1, (b) Blend #2, (c) EDS of different layers for Blend #1, and (d) EDS of different layers for Blend #2

3.4   CONCLUSIONS

TaC and/or CNTs reinforced SiC CMCs were successfully sintered near theoretical density (>98%) using the SPS technique. The β→α transformation of SiC was observed during the SPS, owing to the fact that cubic β-SiC was unstable at temperatures higher than 1500 $^{\circ}$C.

The oxidation behavior of the as sintered SiC ceramics was investigated up to 1500 $^{\circ}$C. Raman spectroscope analysis indicated that CNTs were retained, but subject to compressive stresses from heat, pressure, and electric current during SPS. More disorder occurred in the CNT network with increased oxidation temperature, while the CNTs in Blend #1 were less disordered than those in Blend #2, implying a better oxidation resistance.

The TGA results revealed that the addition of TaC in Blend #1 exhibited an enhanced protective effect in increasing the oxidation temperature of CNTs from 460 $^{\circ}$C to 550 $^{\circ}$C. Generally, three layers were detected for each oxidized cross section, which were the severely oxidized outer layer, the less oxidized middle layer, and the inner base material. When oxidized under 800 $^{\circ}$C, Blend #2 exhibited more weight loss, and its oxidation resistance was attributed to the growth of a protective SiO_2 film which largely decreased the oxygen diffusion inward of the bulk material, while the oxidation mechanism of Blend #1 was determined by the kinetics of both amorphous SiO_2 and Ta_2O_5. A denser and thinner oxidized outer layer containing SiO_2 and Ta_2O_5 was found on Blend #1 oxidized at 1200 $^{\circ}$C, indicating a better oxidation resistance than Blend #2. The improved oxidation resistance of Blend #1 benefitted from the crystalized Ta_2O_5 that embedded in the glassy protective layer. With oxidizing temperature up to 1500 $^{\circ}$C, the protective outer layer got thicker but more porous denoting a degraded oxidation resistance. The oxidation mechanism of Blend #1 was controlled by the crystallization of SiO_2 and Ta_2O_5.

4.0 DYNAMIC RESPONSE OF TAC/CNTS/SIC CMCS UNDER HIGH STRAIN RATE LOADING WITH ELEVATED TEMPERATURE OR MOIST ENVIRONMENT

4.1 INTRODUCTION

The overall material performance of the ceramic composites under dynamic loading depends on the material configuration (thickness, reinforcements, manufacturing methods), loading rates, loading direction, and environmental conditions. On the basis of framework 1.3.3, this chapter highlights the effects of sample thickness, impact energy (loading rates), temperature and moisture on the compressive dynamic response of TaC and/or CNTs reinforced SiC CMCs. The high strain rate tests are conducted by a penetration split Hopkinson pressure bar (P-SHPB). Material properties in terms of ultimate stress, ultimate strain, strain rate, compressive modulus, energy absorption, and particle velocity are investigated. Damage patterns induced by the dynamic indentation are compared.

Ceramic matrix composites (CMCs) are known as an attractive choice for applications in aerospace turbine engines and future space vehicles. SiC CMCs are non-oxide composites possessing high strength and modulus at elevated temperatures. However, the exceptional strength and stiffness also cause the ceramic to be very brittle, while fails catastrophically. With the addition of high performance reinforcing carbon nanotubes (CNTs), the overall material properties of the ceramic composites can be increased significantly [182-183]. Unfortunately,

many of these CNTs reinforced CMCs have exhibited degradation when undergoing high strain rate loading conditions of a short duration that produce stress wave pulses with a strain rate up to a few hundred per second, and when simultaneously in the presence of high temperature and moisture [184]. As a result, it would be of great interest to study the environmental effects on composite materials subjected to dynamic deformation.

A significant amount of work has been done on the strain rate sensitivity of ceramics under dynamic loading [185-188], and on the influences of moisture and temperature [189-192] on quasi-static material properties of ceramic composites. Brittle ceramic composites under dynamic loading, in general, are characterized by increased fracture strength [193-194] and fracture toughness [195-196]. Fiber/matrix interphase plays an important role in improving the material performance of CMCs. Absorbed water molecules transport through the pores and microcracks in the matrix, and interacts with CNTs [197], which will propagate cracks and weaken the interfacial bonding between the CNTs' surfaces and the ceramic matrix. The SiC CMCs are reported to experience significant strength reduction in the intermediate temperature (450-900 ^{o}C), where cracks in matrix material allow the oxygen to penetrate inside and degrade the material properties [198-199]. Up to this date, very limited information is available in the literature about the high strain rate response of SiC CMCs under the influence of temperature and moisture.

4.2   THEORETICAL BACKGROUND

4.2.1   Strain, strain rate, and stress measurements

The basic assumptions and validity of SHPB in the study of the dynamic behavior of materials are well documented [200 - 202]. These assumptions are true for the present investigation, namely, that minor local heat generated during the impact does not change the material properties of the specimen; the Hopkinson bar is elastic and wave propagation within the bar follows elementary wave theory; the slender cross sectional bar of the ratio is $d/L<1/50$, where d and L are the diameter and length of the bar; and the shape of the wave is non-dispersive and it remains unchanged during propagation along the bar. That is, the plane wave will remain planar and parallel to the cross section during propagation from one section to another; the state of the stress is in equilibrium along the entire bar at any instant of strain measurement due to the dynamic impact of having a long bar and a thin specimen; transverse strain, lateral inertia, body forces, and parasite waves are all negligible. For the P-SHPB, it is assumed that the effect of fixture and the indenter's head on the stress waves' configuration in the bars is small enough to be neglected. It is further assumed that sample strain is much greater than the total strain of the bar and the specimen fixture.
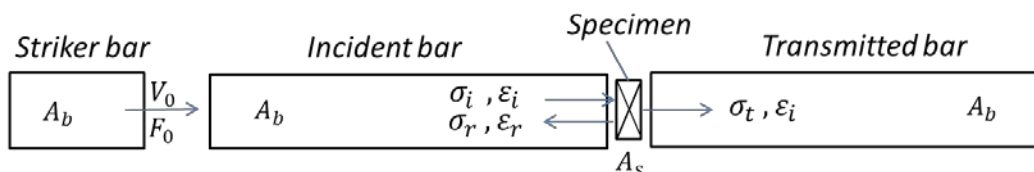
Fig. 4-1 Schematics illustration of wave propagation

A simplified schematic of the wave propagation is shown in Fig. 4-1, and the subscripts of i, r, and t stand for incident, reflected, and transmitted waves, respectively. Dynamic loading is provided by the longitudinal impact load F_0 of the strike bar, generating a uniaxial stress pulse at the incident bar, as:

$$\sigma(t) = \frac{F_0}{A_b} = \rho c v(t) \qquad (1)$$

where A_b is the cross sectional area of the incident bar, ρ is the density of the incident bar material, c is the wave velocity in the bar, and $v(t)$ is the particle velocity. Accurate measurements of the wave pulse in dynamic impact studies are important since the wave train is considered the propagation of the disturbance or vibration of the particles. With a specimen of the cross sectional area, A_s, placed in a specimen fixture and sandwiched between the incident bar and the transmitter bar of the cross section area, A_b, equilibrium at each interface (incident bar/indenter, indenter-head/specimen, specimen/specimen holder, and specimen holder /transmitted bar) encountered is satisfied by the continuities of forces and velocities at the interface [203, 75]. The incident, reflected, and transmitted strain waves are captured from strain gauge measurements on the bars. The amplitude of the incident wave pulse depends on the impact velocity (a function of the applied air pressure) and material properties of the striker bar. By solving wave equation, the displacement of the incident bar is denoted as:

$$u(x, t) = f(x - ct) + g(x + ct) = u_i(x, t) + u_r(x, t) \qquad (2)$$

$$\varepsilon(t) = \frac{\partial f(x,t)}{\partial x} + \frac{\partial g(x,t)}{\partial x} = \varepsilon_i(t) + \varepsilon_r(t) \qquad (3)$$

Upon the arrival of a compressive incident wave at the specimen/incident bar interface, the wave is partially reflected (because of the impedance mismatch) and partially transmitted through the specimen. Thus, the displacement, u_1, and force, F_1, at the incident bar/specimen interface can be expressed as:

69

$$u_1(t) = \frac{c}{E} \int_0^t \big(\sigma_i(t) + \sigma_r(t)\big) dt \tag{4}$$

$$F_1(t) = A_b E \big(\varepsilon_i(t) + \varepsilon_r(t)\big) \tag{5}$$

Similarly, the displacement of the incident bar is:

$$u(x,t) = h(x + ct) = u_t(x,t) \tag{6}$$

$$\varepsilon(t) = \frac{\partial h(x,t)}{\partial x} = \varepsilon_t(t) \tag{7}$$

And the displacement, u_2, and force, F_2, at the specimen/transmitted bar interface are:

$$u_2(x,t) = \frac{c}{E} \int_0^t \sigma_t(t) dt \tag{8}$$

$$F_2(t) = A_b E \varepsilon_t(t) \tag{9}$$

Assuming a uniform stress through a thin specimen ($F_1 = F_2$, $\varepsilon_i + \varepsilon_r = \varepsilon_t$), the sample stress, strain, and strain rate can be expressed as:

$$\sigma_s(t) = \frac{F_1 + F_2}{2A_s} \approx \frac{A_b}{A_s} E \varepsilon_t$$

$$\varepsilon_s(t) = \frac{u_1 - u_2}{L_s} \approx \frac{-2c}{L_s} \int_0^t \varepsilon_r(t) dt \tag{10}$$

$$\dot{\varepsilon}_s(t) \approx \frac{-2c}{L_s} \varepsilon_r(t)$$

where A_b and A_s are the cross sectional areas of bars and sample, c is wave velocity, E is young's modulus of the bars, L_s is the specimen thickness, σ_i, σ_r and σ_t are incident, reflected and transmitted stress, and ε_i, ε_r and ε_t are incident, reflected and transmitted strain.

4.2.2 Energy measurement

Assuming that the energy delivered by the incident bar with an indenter is equal to the total expendable energy for the impact process, the energy delivered by the propagating compressive wave to the composite plate is derived as:

$$E_d = \int_0^t F_i(t) du_n \equiv E_A \tag{11}$$

where $F_i(t) = A(\sigma_i(t) + \sigma_r(t))$ is the net compressive loading force, the net displacement du_n is:

$$du_n(t) = \frac{c}{E} \int_0^t (\sigma_i(t) - \sigma_r(t) - \sigma_t(t)) dt \tag{12}$$

The total expendable energy can be obtained as the integrated area of the force-displacement curve over the duration of the wave. Substituting du_n expression from Eq. (12) into (11), the net energy to be expended for the damage process, plus energy losses to the fixture, is expressed as:

$$E_A(t) = \frac{A_b c}{E} \int_0^t (\sigma_i^2(t) - \sigma_r^2(t) - \sigma_t^2(t)) \, dt \tag{13}$$

Thus, Eq. (13) gives the total energy absorption curve decomposed into energy absorbed by the plate (ΔE_{abs}) and the elastic strain energy (ΔE_s), i.e.,

$$E_A^{min} = \Delta E_{abs}$$

$$E_A^{max} = \Delta E_{abs} + \Delta E_s \tag{14}$$

According to Eq. (14), the elastic strain energy is the difference between the peak energy and the residual energy absorbed. The rest of the energy is dissipated in the formation of the plastic deformation of the sample or lost in overcoming friction.

The validly of the proposed P-SHPB method can be justified since only the strain measurements on the incident and transmitted bars, and the geometry of the bars and specimen, are required for the determination of particle velocities, displacements, and energy absorption.

The drawback in the continuity assumption, however, is that energy losses to the specimen holder and the indenter could reduce the relative strain reaching the gage at the mid-point of the transmitted bar. This will result in over-estimating the energy measurement by Eq. (13). An experimentally determined correction factor that accounts for the total energy loss to the indenter and holder are usually applied to minimize the error due to the losses. Although the error could reduce the accuracy of the P-SHPB method for absolute measurements of materials properties, P-SHPB remains a reliable tool for elaborating upon the fracture mechanics and dynamic failure behaviors of composite materials subjected to high strain rate loading [204].

4.2.3 Moisture absorption measurement

The water absorption rate, which is the weight of moisture in the pores as a fraction of the weight of the tested ceramic composites, is determined by the following equation [205]:

$$c_t(\%) = (\frac{c_t - c_0}{c_0}) \times 100 \tag{15}$$

where c_t is the weight of the sample at time t, c_0 is the initial weight of the sample. The water absorption behavior of the sample can be studied by Fick's equation [205, 206]:

$$\frac{c_t}{c_\infty} = 4(\frac{Dt}{\pi h^2})^{1/2} \tag{16}$$

where c_∞ is the equilibrium water content, D is the diffusion coefficient, and h is the sample thickness.

4.3   EXPERIMENTAL PROCEDURE

4.3.1   P-SHPB impact system

Fig. 4-2 is a schematic diagram of the indentation assembly for the Hopkinson bar system. The figure shows the indenter and specimen support that holds the composite sample. The fixture is sandwiched between the incident and transmitter bars as shown. The indenter is attached to the end of the incident bar through its inner diameter. The sample holder is attached to the transmitter bar with its open end facing the indenter. The striker is housed inside a launch cylinder and is driven by compressed air. To begin each test, the desired pressure is manually set using a gauge between the launch cylinder and the reservoir. A switch in the control room activates the opening of a quick-acting solenoid valve, allowing compressed air acceleration of the striker into the incident bar. The impact-end of the striker is spherically rounded for a repeatable point of contact with the incident bar on a plane centrally normal to the longitudinal direction of the wave propagation. Proper axial alignment between the striker and incident bars is ensured to minimize flexure. The uniaxial waveform generated in the bar determines the rate at which energy is transferred from the bar to the sample. The geometrical shape of the striker and the impact velocity controls the shape of the waveform. The stress wave amplitude varies with impact velocity, while the stress profile changes with striker geometry. Incident and transmitter bars are guided through pillow blocks containing low-friction ball bearings. The bushings (mounted on a rigid steel channel which is backed up by an I-beam) support the bar shifts without restraining them. The support can be adjusted laterally and vertically for proper alignment. To minimize vibration, the unit is anchored to steel beams running through a 102 mm steel-reinforced concrete deck. A striker rod is attached to one end of the striker and protrudes

outside the cylinder as a means of adjusting the stroke length (and, therefore, the striker velocity). Venting holes along the launch tube maintain a low-pressure zone in front of the striker and prevent the possibility of multiple impacts. The experimental parameters for the sample and system are described in Table 4-1.
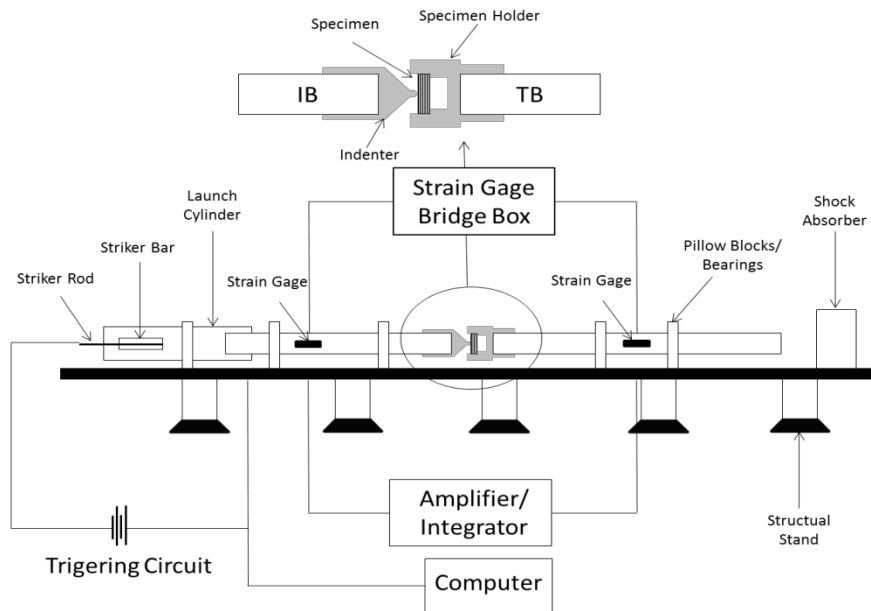
Fig. 4-2 Schematic diagram of the P-SHPB system

Table 4-1 Experimental parameters

Specimen Parameters:	
Diameter:	20.32 mm (0.8inch)
Thickness:	3mm, 4mm, 5mm, 6mm
Specimen Type:	TaC/CNTs/SiC, CNTs/SiC CMCs
System Parameters:	
Hopkinson Pressure Bar:	
Young's modulus of maraging steel bar:	2.07×10^{11} Pa
Wave velocity in maraging steel bar:	5010 m/s
Bar length:	2.4384 m
Density of maraging steel:	8000kg/m^3
Impact Parameters:	
Indenter:	1/4-inch diameter conical hemispherical-nosed
Striker bar length:	0.305m maraging steel
Ram displacement:	0.61 m to impact the incident bar
Compressed air pressure:	0-30 psi

4.3.2 System calibration

A calibration curve is established as a correlation between the compressor impact pressure and the striker impact velocity delivered to the incident bar. The striker velocity just before impacting the incident bar was measured as a function of impact pressure using two infrared photo gate detectors. A pair of infrared detectors mounted on the striker bar measures the average velocity of the striker bar just before impact with the incident bar. A second set of infrared detectors on the incident bar measures the particle velocity of the incident bar (V_p). The kinetic energy of the striker bar (referred to impact energy E_i) is then calculated from the known mass of the striker bar. The striker impact energy is directly proportional to the bar indentation energy and is directly controlled by the experimenter by simply controlling the compressed air pressure.

Fig. 4-3 depicts the calibration curves showing the nonlinear relationship between the striker impact velocity, energy, and pressure. The striker impact velocity is related to impact energy and particle velocity in the following equations:

$$E_i = \frac{1}{2}m_s V_i^2 \tag{17}$$

$$V_i = 2V_p \tag{18}$$

where m_s is the mass of the 0.61 m striker bar equal to 2.47 kg, V_p is the particle velocity at the indentation end of the incident bar. Calibration measurement of the particle velocity shows a 2% error from the theoretical value given by $V_i = 2V_p$ as compared to $V_i = 1.96V_p$ from direct measurement. The above relationships provide us with a reliable impact pressure to impact energy calibration.
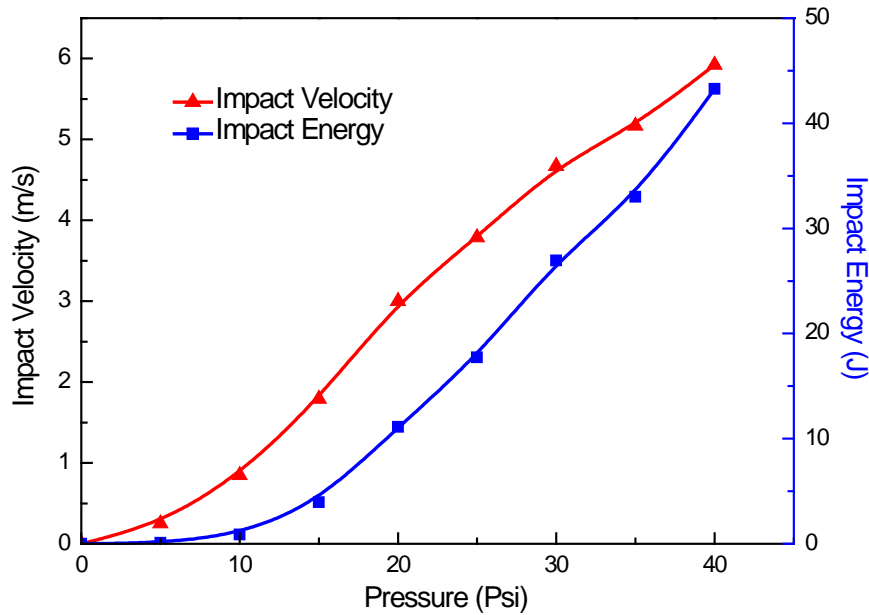
Fig. 4-3 Impact velocity and energy as a function of pressure

4.3.3 Experimental design

The indentation tests were carried out in the thickness direction at a 4-27 J striker bar impact energy to investigate the effect of sample thickness and impact energy on the TaC/CNTs/SiC ceramic composites' failure response under dynamic compressive loading.

For the effect of temperature, TaC/CNTs/SiC ceramic specimens were heated in a separate oven. Once the required temperature was achieved, samples were quickly taken out, fitted into the holder in-between the horizontal pressure bars, and made ready for the impact. In the meantime, a high performance thermal imaging infrared camera (Flir SC5000, Flir Systems Inc, PA, USA) was used to monitor the specimen's temperature.

As for the influence of moisture absorption, a comparison group of TaC/CNTs/SiC (Blend #1 with a densification of 98.4%) and CNTs/SiC (Blend #2 with a densification of 99.5%) composite samples were prepared in consideration of the different densification of the two

76

composites. To test the moisture absorption rate, samples were immersed in water at room temperature, taken out of the water at regular intervals, wiped with filter paper to remove surface water, and then weighed with a balance with an accuracy of 0.01 mg (Mettler Toledo, AB135-S/FACT). Samples were re-immersed into water for a sufficiently long time until equilibrium was reached. The moisture absorption as a function of the square root of time for the two ceramic composites is plotted in Fig. 4-4. The straight initial period indicates that they obey Fick's law of diffusion, and the linear slope is directly proportional to the moisture diffusion coefficient of the samples, according to Eq. (16). The calculated moisture diffusion coefficients for Blend #1 and #2 are 1.31×10^{-4} mm^2/s and 1.93×10^{-4} mm^2/s. The maximum moisture absorption at the equilibrium state for Blend #1 samples was 3.2%, which was higher than that of 1.1% for Blend #2 samples. This is reasonable because Blend #1 ceramics had a lower densification, providing more pores for water absorption.
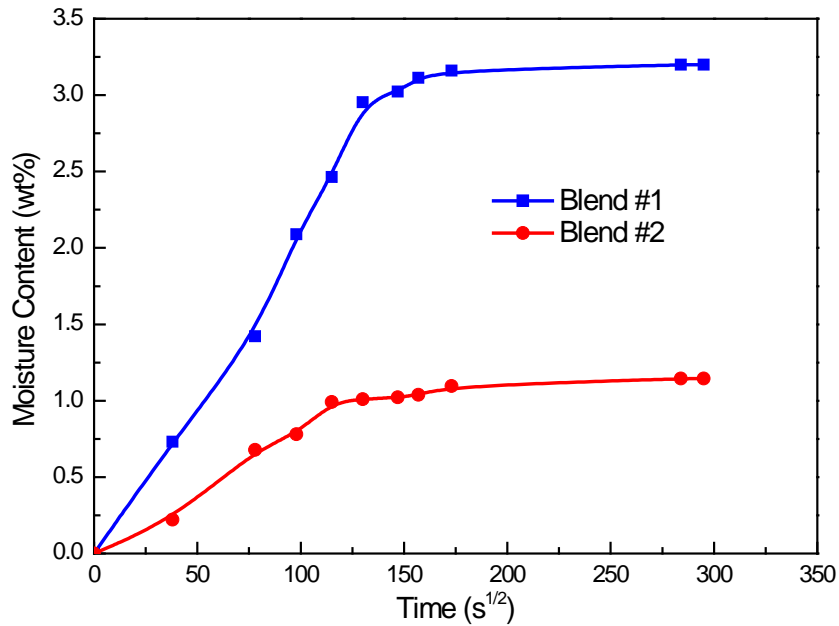
Fig. 4-4 Moisture absorption behavior of the sintered ceramic composites

4.4 RESULTS AND DISCUSSION

4.4.1 P-SHPB wave correction

The theoretical formulae for the P-SHPB are based on the conventional SHPB in Fig. 4-1, for which the specimen is sandwiched between the incident bar and transmitted bar. The setup of P-SHPB presented in Fig. 4-2, including the indenter and specimen holder, introduces additional boundaries and interfaces to the system, and causes the assumptions of equilibrium and continuity to not be achieved fully. Account for the equilibrium deviation and appropriate corrections for the waves of P-SHPB are experimentally determined as:

$$C(t) = \frac{\varepsilon_{SHPB}}{\varepsilon_{F-SHPB}} \tag{19}$$

where ε_{SHPB} is the measured SHPB strain pulse without indenter or specimen holder, and ε_{F-SHPB} is the measured strain pulse for P-SHPB setup. Fig. 4-5 shows a nonlinear time dependence of the correction factor $C(t)$, determined by a forth order polynomial fitting with r=0.985.

$$C(t)=6.77E-9*t^4-5.61E-6*t^3+1.13E-3*t^2+1.82E-2*t+1.53$$
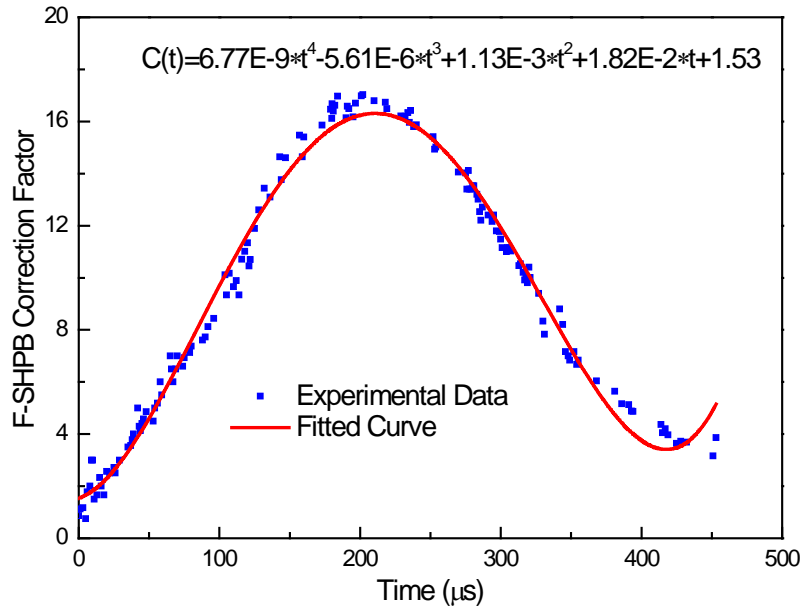
Fig. 4-5 Time variation of P-SHPB correction factor

Fig. 4-6 shows the incident, reflected, and transmitted strain waveform, determined from the measured strain signal using appropriate system calibration. The incident wave reaches the strain gage located at 1.22 m in 260 μs and 520 μs to the bar/specimen interface at 2.44 m. This represents a wave speed of 4692 m/s as compared to the 5010 m/s theoretical value [207], with a difference of 6.3%. It is noted that the theoretical wave speed is determined from the density and elastic modulus data supplied for the maraging steel Hopkinson bar material. Part of this incident wave is reflected back and travels the same time to reach the strain gage on the incident bar. Without a specimen, the transmitted wave will also begin its traverse time at the same time as the reflected wave and will reach the strain gage on the transmitter bar after 260 μs. The waveform is captured at a sample rate of 250,000 samples/sec at 4 J and 27 J impact energy. The 4 J wave, for no incipient damage, shows more than two full reflections before the wave experiences any distortion, and a smooth transmitted wave as compared to the 27 J wave that has a reduced reflected wave amplitude and distorted transmitted wave. This is because most of the residual

79

energy returns to the system when indentation causes damage to the material. The strain wave pulse from the P-SHPB experiment provides information for a complete characterization of the damage process.

(a)

(b)
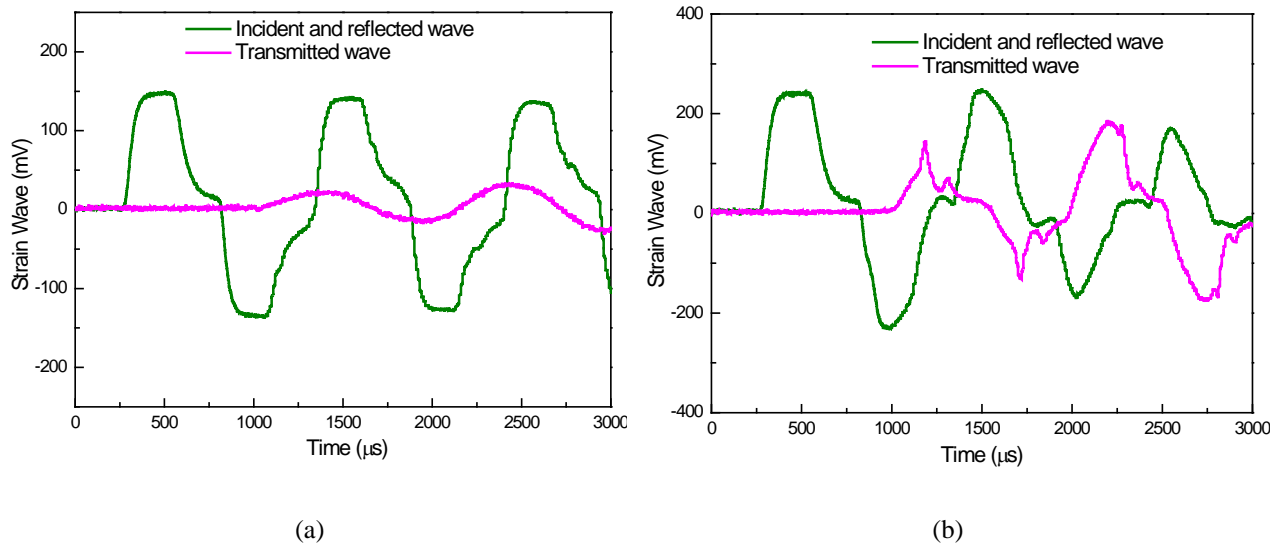
Fig. 4-6 Comparison of strain waveform for the impact test (a) 4 J with no incipient damage and (b) 27 J with indentation

4.4.2 Effect of sample thickness on high strain rate response

Fig. 4-7 compares the effect of sample thickness on the longitudinal compressive stress-strain (a) and strain rate (b) behaviors of TaC/CNTs/SiC CMCs at a 12 J striker bar impact energy. The stress-strain curve exhibits typical behavior of brittle materials, and provides a good estimation of how much the specimen is strained at the onset of damage initiation. The ultimate strength is defined as the stress of the ceramic specimen at which rupture occurs, and proved to be a sensitive basis for surface damage development and characterization [196]. The ultimate stress levels in the specimen were in the range of 7.8-19.4 MPa. In all cases, no evidence of catastrophic stress drop was observed, and the relative long tail in Fig. 4-7(a) indicates that stress

80

was still carried by the ceramic specimen. It is clear that thicker specimens developed greater ultimate strength to failure than thin specimens, which implies that thicker specimens allowed more strain wave to be transmitted to the transmitted bar according to Eq. (10).

Fig. 4-7(b) displays the strain rate-time histories for various thickness specimens. The specimen reached a plateau region of maximum strain rate within the first 100 μs after impact with the compressive stress wave. It remained constant for about 200 μs, at which time the damage to the specimen must have been completed, and then the strain rate dropped to zero. This behavior also validates one of the assumptions made for the use of the Hopkinson bar for high strain experiments. It is clear from the summary plot in Fig. 4-7(c) of the peak strain rate values that the strain rate decreased from 307 to 168 1/s with the increase of thickness. It was hypothesized that strain rate is inversely proportional to specimen thickness. The results show that the relationship in most cases is almost linear.

The variations of the compressive elastic properties of the ceramic composites are shown in Fig. 4-7(c). As the ultimate strength increased with thickness while the ultimate strain decreased with thickness, the compressive longitudinal modulus increased (108-440 MPa) with sample thickness (3-6 mm). This is owing to the fact that thicker materials tend to behave in a more brittle manner by decreasing the plastic damage zone, due to the effective increase of the ultimate strength [208]. However, once the sample thickness is sufficiently large, such as in a state of plane strain, further increases in thickness will not be applicable in the P-SHPB experiments.

(a)

(b)

(c)
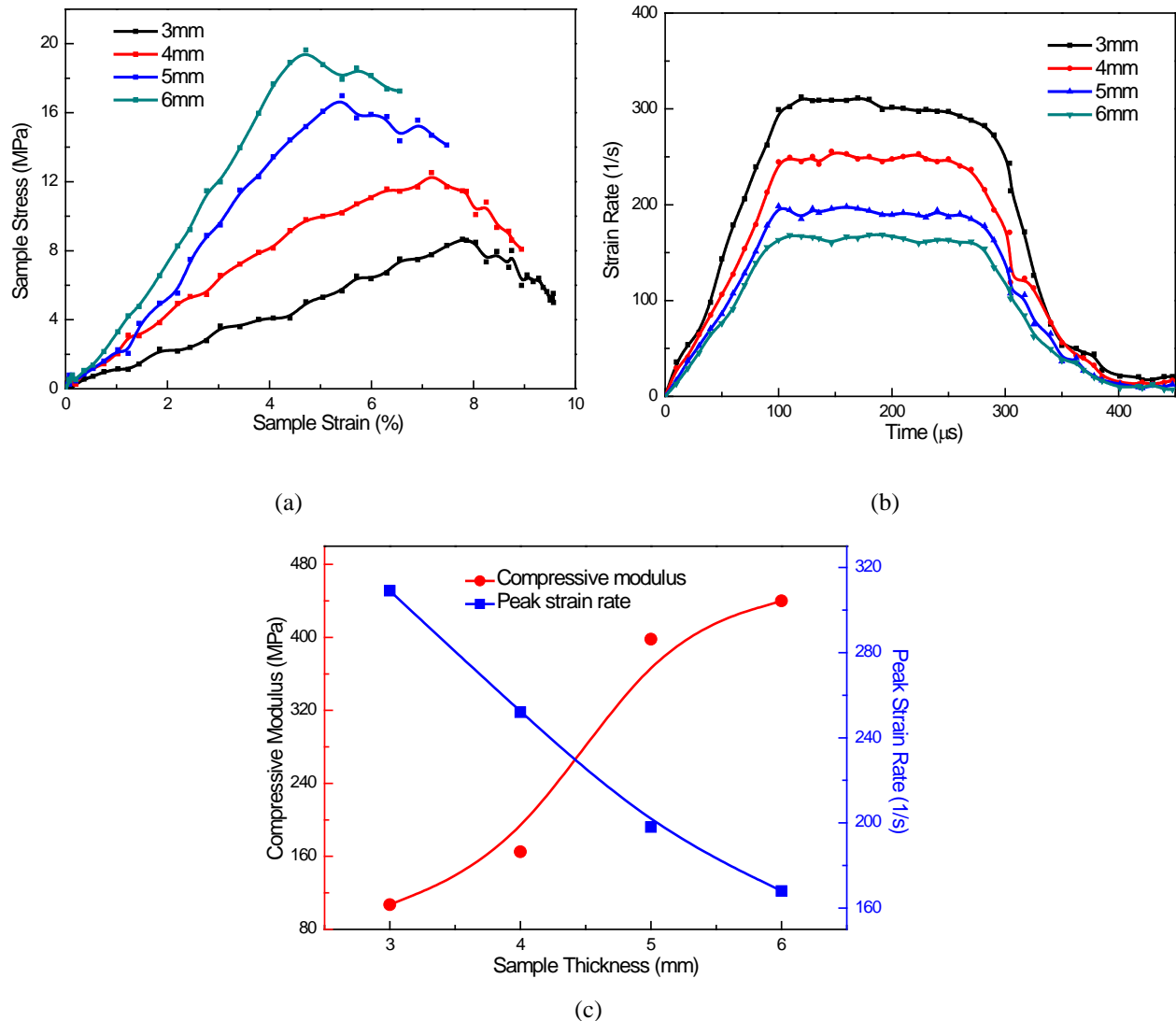
Fig. 4-7 Effect of sample thickness on (a) stress-stain behavior, (b) strain rate-time history and (c) compressive modulus and peak strain rate

Fig. 4-8(a) shows the variation of energy absorption with time for different sample thickness. Energy absorption increased linearly during the intial loading of the specimen up its peak value, and then decreased due to the strain energy released in the impact. The peak energy absorbed and the particle velosity are summarly plotted in Fig. 4-8(b). It can be safely concluded that, at the same striker bar impact energy, the peak energy absorbed and particle velocity had a high dependency on sample thickness. The peak energy absorbed increased almost

linearly with a sample thickness from 0.48 to 0.78 J, while particle velocity decreased nonlinearly with sample thickness from 0.88 to 0.84 m/s. This may be explained by the increasing brittleness and hardness of thicker specimens that restrained particle motion and increased energy absorption.

(a) (b)
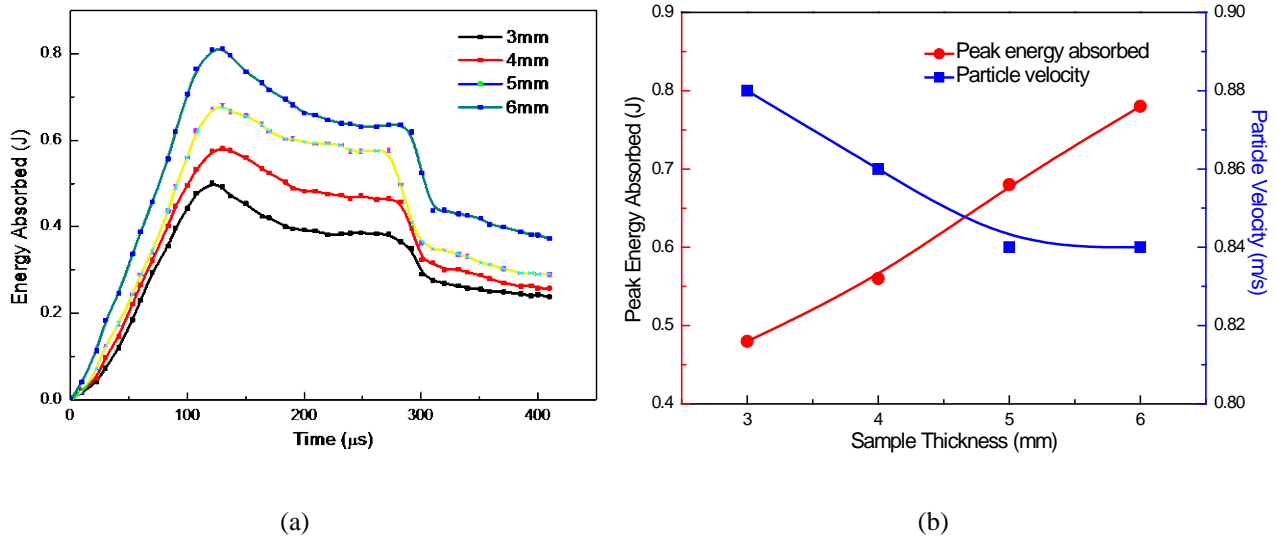
Fig. 4-8 Effect of sample thickness on (a) energy absorption-time history and (b) peak energy absorbed and particle velocity

4.4.3 Effect of impact energy on high strain rate response

Fig. 4-9 illustrates the influences of impact energy on the stress-strain (a) and strain rate (b) behaviors of 6 mm TaC/CNTs/SiC CMCs specimens. In all cases, the ultimate stress and strain rate are seen to increase with the increasing of impact energy level. No crack was observed for a lower energy impact of 4 J and 12 J, while multiple surface cracks onset to propagate at 18 J impact energy. Specimens were observed to fracture at a 27 J impact energy. It should be noted that the ultimate stress at an 18 J impact energy was 47.8 MPa, and at a 27 J impact energy, was 55.4 MPa, while the corresponding ultimate strain was 5.9% and 6.1%, which is very similar to

83

the strain hardening mechanisms in metals. Fig. 4-9(b) and (c) show the peak strain rates increased from 168 to 311 1/s on ceramic samples response to indentation impact from 4 to 27 J. Three regions can be observed as described in Fig. 4-7(b). The first region is related to elastic stress distribution in the samples. This region cannot be used to determine the elastic properties of materials due to the stress wave reflection and stress nonuniformity caused by the nature of the SHPB method. The flow of stress plastically through the specimen generates a high strain rate so that the strain rate remains at the ultimate limit before the strain hardening of the materials lowers it. This observation is in agreement with strain-rate-dependent theory as originally proposed by Malvern [209] which decomposes strain rates into an elastic and plastic portion, and predicts that a material will reach a state of incipient plastic flow after a certain amount of elastic strain has been attained. Subsequently, the specimen begins to retain or dissipate the energy for the damage events such as fracture.

The variation of the compressive longitudinal modulus with different impact energies are plotted in Fig. 4-9(c). While both the ultimate strength and ultimate strain increased with impact energy, the results generally show an increasing trend for the compressive modulus. The increase of the compressive modulus is very slow on the incipient of fracture (830 MPa). Since a higher impact energy level generates higher strain rate loading, it can be equivalent to saying that the compressive modulus increased under higher strain rate loading. This phenomenon can also be explained by the hardening and embrittlement of materials as the loading rate changes a material's ductile-to-brittle transition behavior.

(a)

(b)

(c)
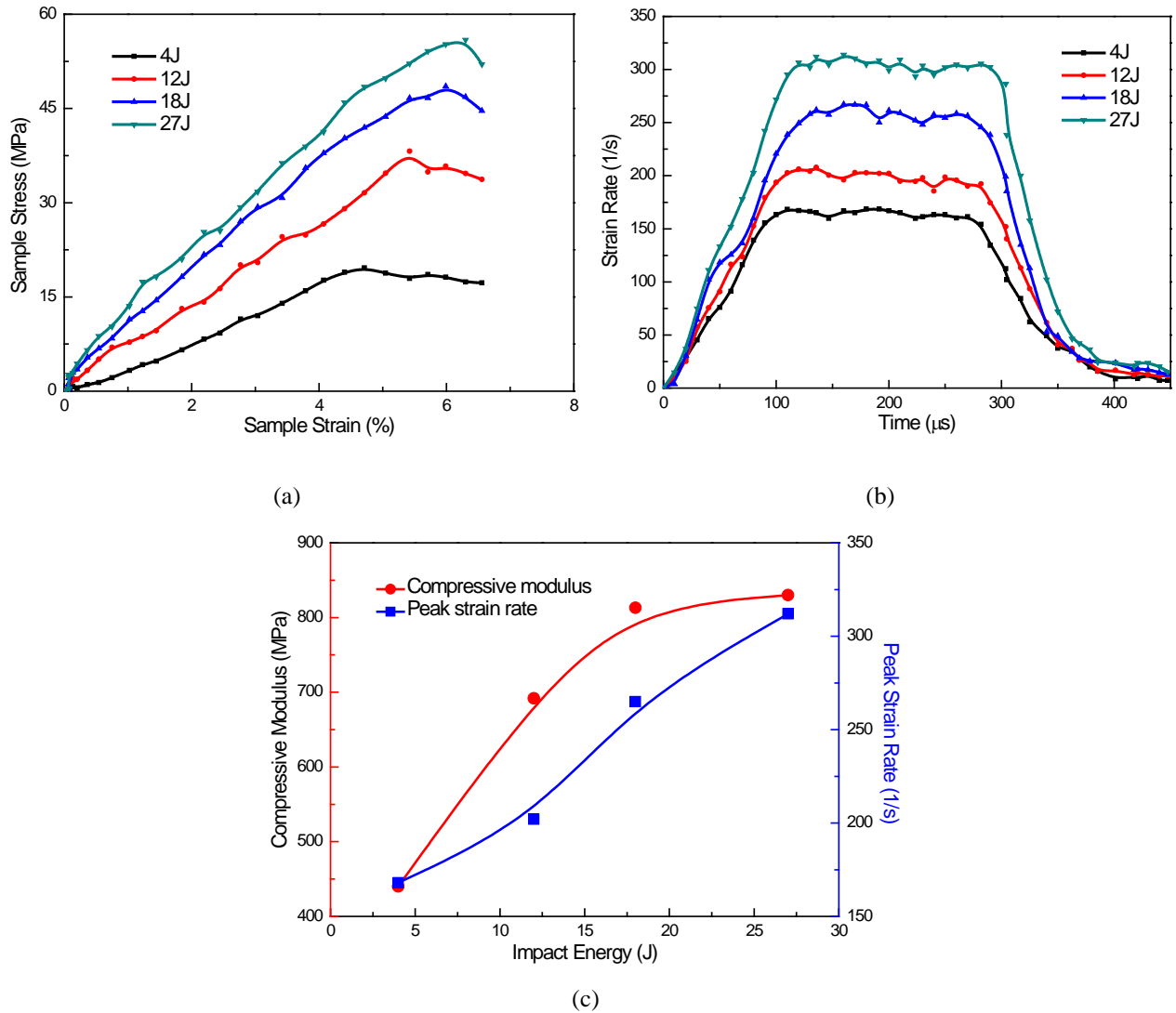
Fig. 4-9 Effect of impact erngy on (a) stress-stain behavior, (b) strain rate-time history and (c) compressive modulus and peak strain rate

The energy absorption-time curves in Fig. 4-10(a) show that the total energy released or delivered to the system for damage initiation and propagation depended on the striker impact energy. The results clearly show that the energy retained by the composite specimen was only slightly different at low energies. When increasing the impact energy to 18 J, energy absorption increased sharply. Ringing in the energy-absorbed curve is an indication of greater particle vibration and energy dissipation in the specimen. Fig. 4-10(b) shows a high dependency of

particle velocity (0.84-2.47 m/s) on the impact energy. The higher the impact energy, the greater the load on the specimen will be, and, therefore, the greater the vibration and propagation of the particles.

(a)   (b)
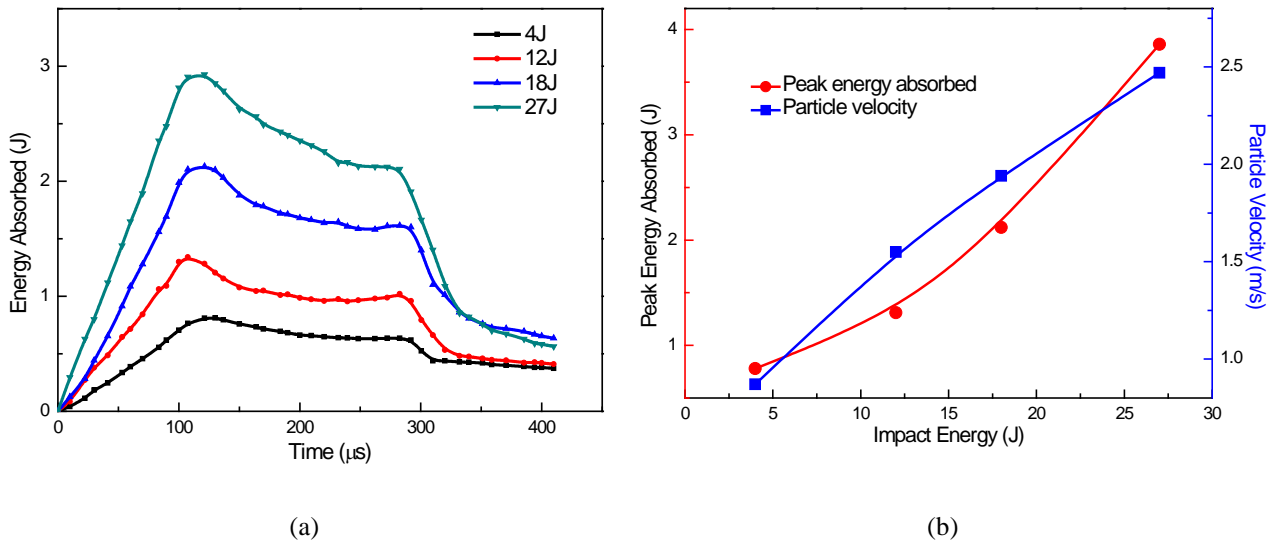
Fig. 4-10 Effect of impact energy on (a) energy absorption-time history and (b) peak energy absorbed and particle velocity

4.4.4   Effect of temperature on high strain rate response

Fig. 4-11 and Fig. 4-12 show stress-strain, strain rate and energy absorption plots under 12 J compressive loading on 6 mm TaC/CNTs/SiC CMCs specimens at room and elevated temperatures in the range of 24-500 ^{o}C. The stress-strain curves in Fig. 4-11(a) maintained linearity almost up to the peak fail load for 24-400 ^{o}C indicating that the failure is mostly controlled by the fibers. The slight nonlinearity that is observed for 500 ^{o}C is due to micro matrix cracking and kinking of the fiber prior to final failure. No crack was observed at a 12 J striker impact energy, for all of the temperatures except 500 ^{o}C, which could also be implied by the relatively short tail of the 500 ^{o}C test on the stress-strain curve. In general, the ultimate stress

86

decreased while the ultimate strain increased with elevated temperature. The average strength degradation from 24-500 $^\circ$C was about 9.8%, and the average strain enhancement was about 8.1%. The reason for such enhanced failure strain at elevated temperatures is probably due to the excellent resilience reinforced by the CNTs [210]. It is clear from Fig. 4-11(b) that temperature had a positive effect on the strain rate. As discussed above, high strain rate loading would embrittle a material by changing the material's ductile-to-brittle transition behavior. Thus, the dynamic strain rate behavior on elevated temperature effect should be explained in terms of the interactions between temperature and strain rate.

Fig. 4-11(c) demonstrates the effect of temperature and strain rate on the compressive modulus. It is evident that the elevated temperature is the dominant effect on the degradation of the compressive modulus. Note that there is just a slight decrease of the compressive modulus from 100-300 $^\circ$C, but the degradation is more severe from 400-500 $^\circ$C. This significant reduction of strength in the intermediate temperature of SiC CMCs was also reported by Mall [198] and Morscher et al. [199]. The degradation of compressive properties under high temperatures would cause cracks in the matrix material, allowing oxygen to penetrate inside and attack the fiber/matrix interphase.

(a)

(b)

(c)
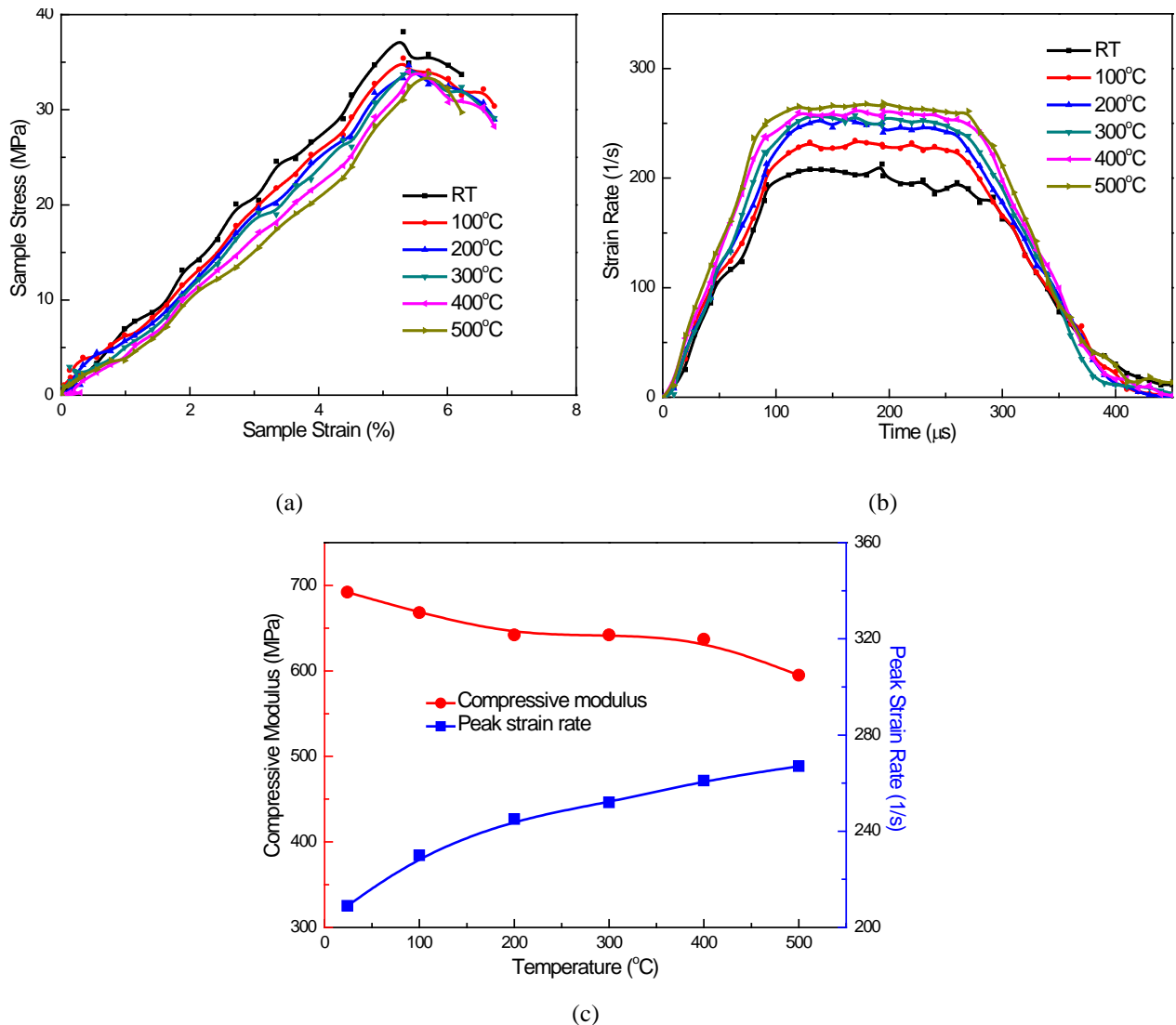
Fig. 4-11 Effect of temperature on (a) stress-strain behavior, (b) strain rate-time history and (c) compressive modulus and peak strain rate

The effect of temperature on energy absorption and particle velocity on a 6 mm specimen at a 12 J striker bar energy is investigated in Fig. 4-12. The peak energy absorption ranged from 1.07-1.31 J, and decreased with the elevated temperature. It is conceivable that heating will increase the thermal mismatch between the fibers and matrix, resulting in an increase in the thermoelastic residual stress. When such residual stress exceeds the matrix strength, microcracks will develop in the matrix, which would lower the energy absorption needed to initiate and

propagate damage on the material. The particle velocity illustrated in Fig. 4-12(b) exhibited a slight increase with the elevated temperature, suggesting that the effect of temperature could accelerate the motion of particles to some extent.

(a)   (b)
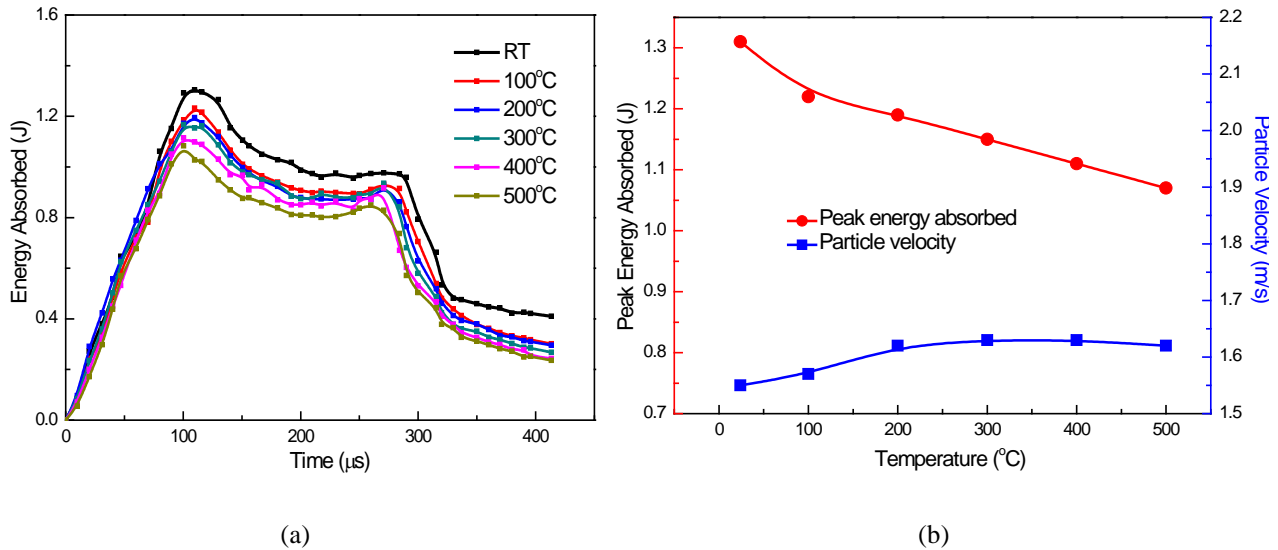
Fig. 4-12 Effect of temperature on (a) energy absorption-time history and (b) peak energy absorbed and particle velocity

4.4.5   Effect of moisture on high strain rate response

The effect of moisture absorption on 4 mm Blend #1 and #2 specimens under a 12 J striker bar impact energy are investigated in Fig. 4-13 and Fig. 4-14. The stress-strain curves in Fig. 4-13(a) still maintained linearity for all of the cases except the wt. 3.2% #1 one, which is caused by the micro matrix cracking and kinking of the fiber before rupture. It can be observed that Blend #1 and #2 dry specimens showed little difference on the dynamic responses. With the increase of moisture content, the ultimate stress decreased up to 6.9% for Blend #2 and 9.2% for Blend #1. This could be due to the fact that immersion of the ceramic composites to water affects the interfacial adhesion between fiber and matrix, leading to the degradation of material strength.

89

In contrast, the ultimate strain tends to increase with the increase of moisture content, which could possibly be due to plasticization and softening effects that occur during the moisture absorption process. The failure strain increments for Blend #1 and #2 are 5.8% and 7.9%, respectively. In most case, the increase of failure strain due to moisture is within 8% [211].

The variation of strain rate with moisture content is shown in Fig. 4-13(b), which shows a considerable increase in the strain rate of wet samples when compared to dry samples. This higher strain rate of wet samples would enhance the material strength to some extent, but cannot compensate for the strength reduction due to moisture absorption. In such cases, the compressive modulus plotted in Fig. 4-11(c) showed a decrease with the increase of moisture content. Water absorbed by the composites is generally free water, which is free to travel through the micro voids and pores, or bound water, which penetrates the composite matrix through micro cracks and reduces the interfacial adhesion of the fiber with the matrix [212].

(a)   (b)
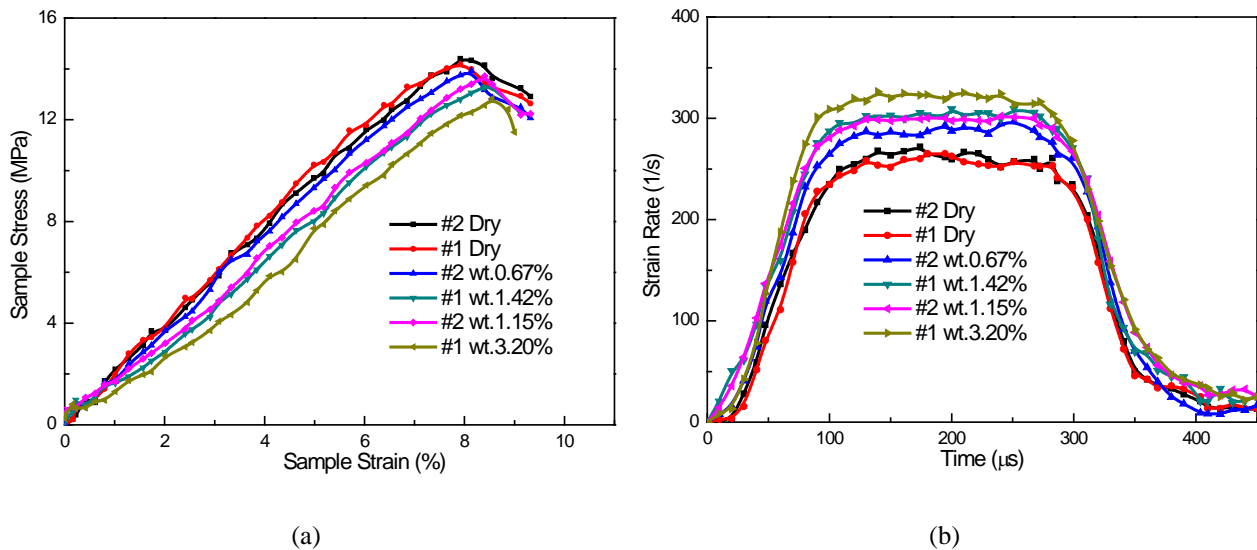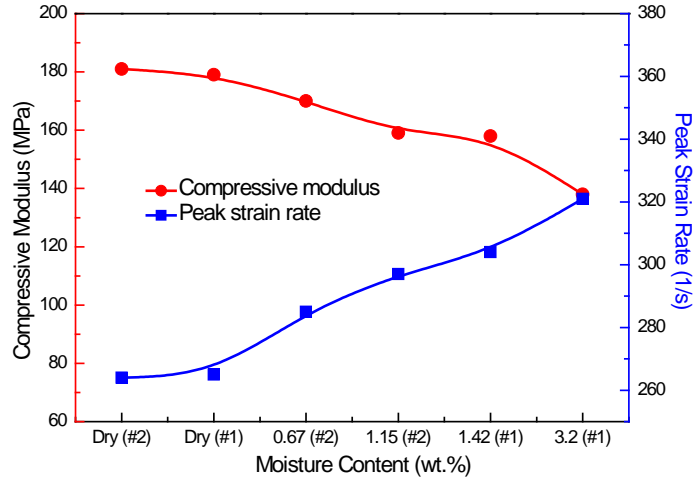
(c)

Fig. 4-13 Effect of moisture content on (a) stress-stain behavior, (b) strain rate-time history and (c) compressive modulus and peak strain rate

The influence of moisture content on energy absorption and particle velocity is displayed in Fig. 4-14. In a similar manner, the energy absorption showed a negligible difference on the two dry samples, but a decrease with the increase of moisture content. The peak energy absorption for the dry sample is 0.91 J, and reduced to 0.71 J for Blend #2, and 0.62 for Blend #1. The water penetration along the microcracks and the fiber/matrix interface weakens the compressive strength of the ceramic composites by lowering the absorbed energy to initiate and propagate the damage. The summary result in Fig. 4-14(b) shows that the particle velocity remained relatively stable for both dry and wet samples.
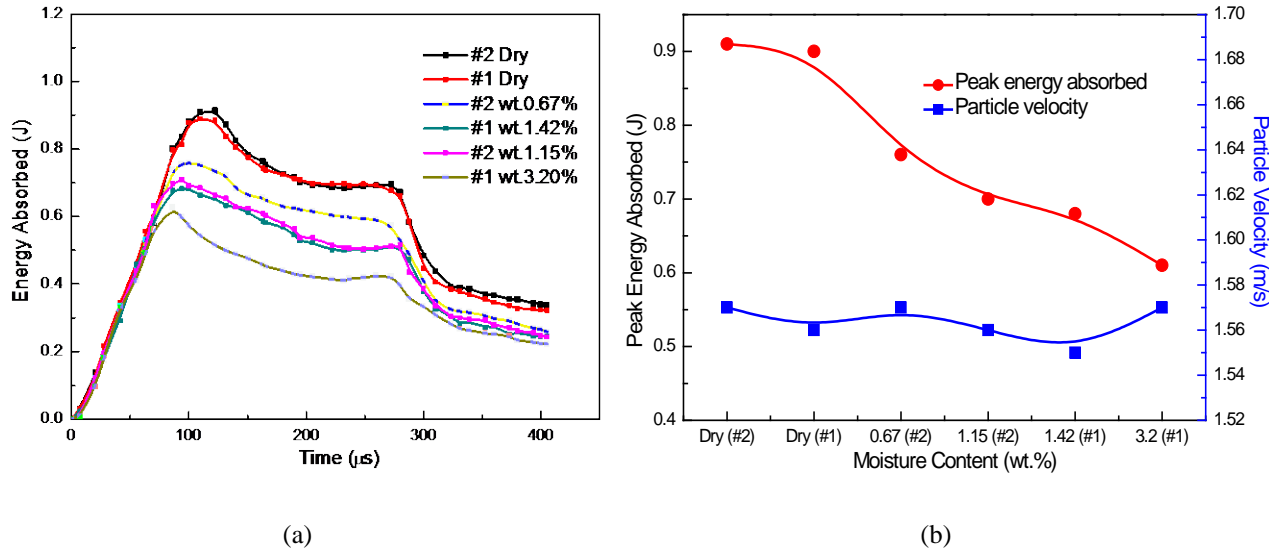
Fig. 4-14 Effect of moisture content on (a) energy absorption-time history and (b) peak energy absorbed and particle velocity

4.4.6 Damage patterns induced by high strain rate loading

Dynamic indentation induced deformation and fracture phenomena are related to the deformation behavior and fracture patterns evolved in the dynamic impact on structural ceramics. A comparison of damage patterns due to different impact conditions is provided in Fig. 4-15. Fig. 4-15(a) shows the undamaged specimen with no observation of cracks, sitting in the holder. Visible cracks propagated from the indentation point are presented in Fig. 4-15(b). These defects will act as potential sources for microcracks initiating and growing into macrocracks, leading to a catastrophic rupture with further loading or in hostile environments. A highly cracked pattern radiated from the impact point is displayed in Fig. 4-15(c) and (d). In such cases, multiple cracks initiate, resulting in extensive fragmentation and eventually in materials' totally losing the capacity for any further loading. Satapathy [213] proposed a dynamic spherical cavity expansion model based on the radial cracking process. In his model, he defined the indentation ceramic

plate as a finite cavity surrounded by the comminuted region which is the penetrator/ceramic plate interface, and then followed by the radial cracks, which is exactly the case in Fig. 4-15(d).

(a)

(b)

(c)

(d)
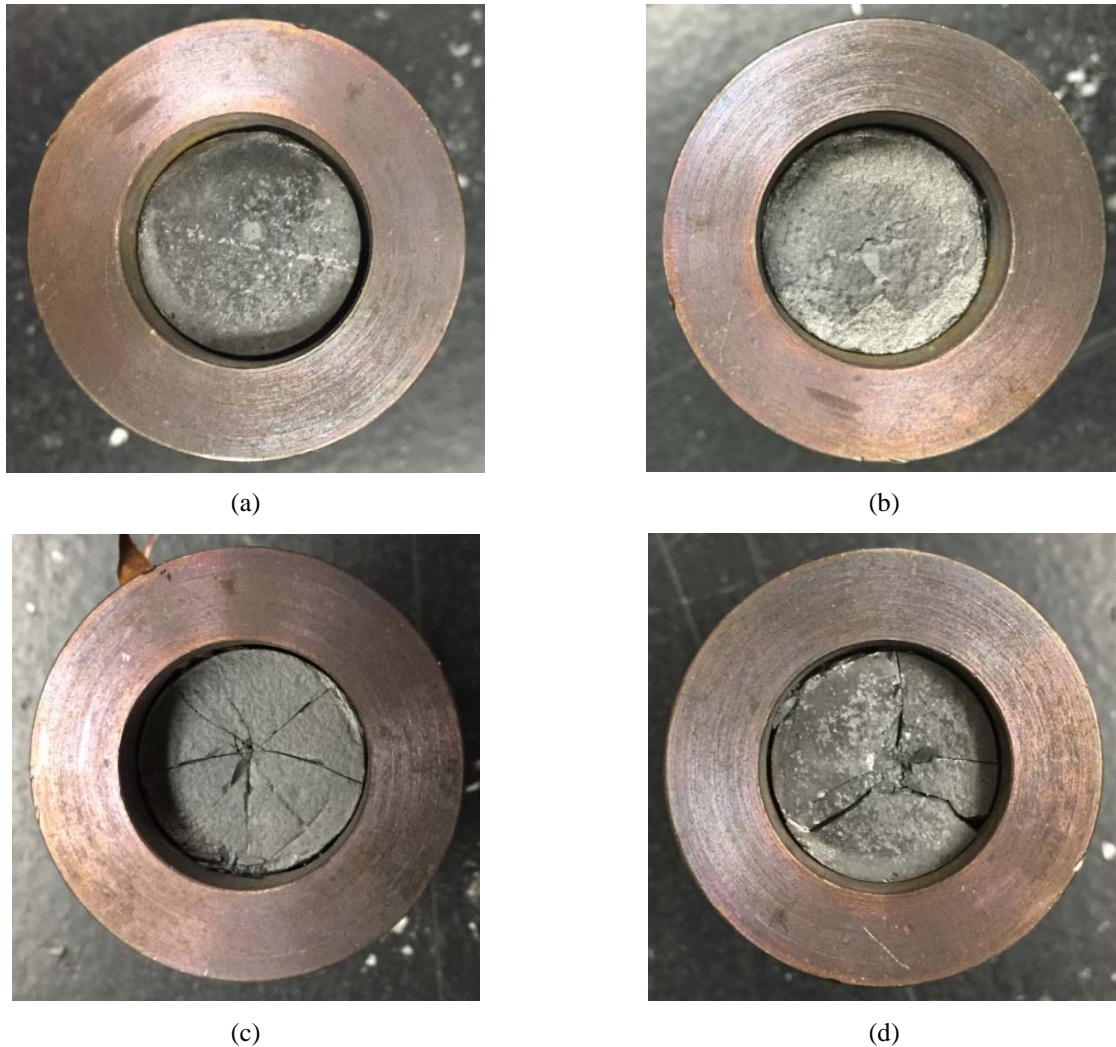
Fig. 4-15 Comparison of the damage patterns induced by dynamic indentation (a) no incipient of crack (b) visible crack propagation (c) high radial cracking (d) fragmentation

Assuming the fragments from dynamic impact are spherical and by measuring the weight of each fragment, the equivalent diameter or size can be obtained. The relation between fragment size and strain rate based on this assumption is presented in Fig. 4-16. The average equivalent fragment size was between 6.19 mm to 9.10 mm in the strain rate range of 168-312 1/s.

According to Zhang et al. [214], the equivalent fragment size under high strain rate can be predicted by the following equation:

$$a = \frac{6K_{IC}^2}{D_f E^2 \left(m\dot{\varepsilon}^{1/(1+\beta)} + \varepsilon_{cr}\right)^2} \tag{20}$$

where K_{IC} is the fracture toughness, D_f is damage scalar, E is young's modulus, m and β are parameters determined by the dynamic fracture properties of the material, and ε_{cr} is the critical strain determined by the quasi-static tensile fracture stress. For brittle materials, β can be taken as equal to 2. A fitting curve with a good correlation (R=0.94) based on Eq. (20) is also plotted in Fig. 4-16. It can be observed that the average equivalent fragment size decreases with the increment of strain rate. From the dynamic view point, fragment size can be related with fracture toughness by a dynamic function of strain rate:

$$a = f(\dot{\varepsilon}) K_{IC}^2 \tag{21}$$

where $f(\dot{\varepsilon}) = \frac{1}{(0.115\dot{\varepsilon}^{1/3} + 0.719)^2}$ is the dynamic function specific for the ceramic composites.
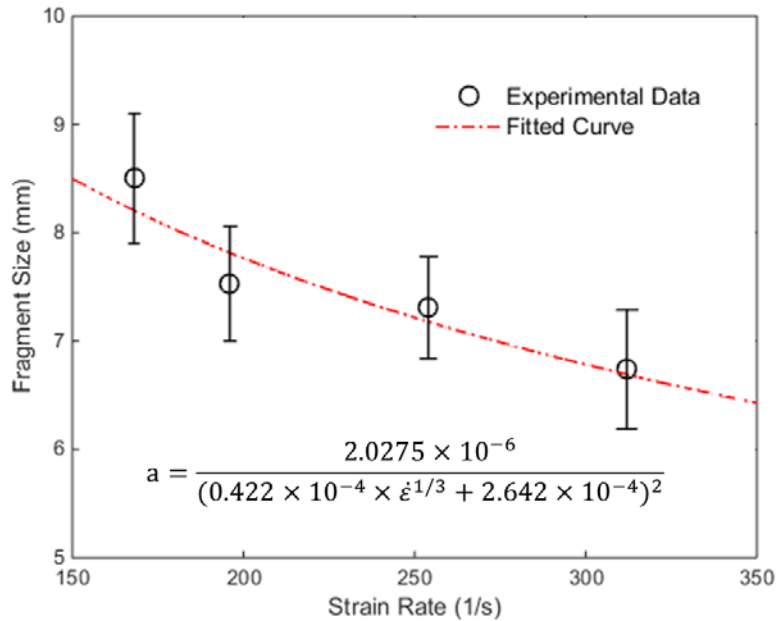
Fig. 4-16 Fragmentation distribution under various strain rates

4.5   CONCLUSIONS

The effects of sample thickness, impact energy, temperature, and moisture on the material properties of TaC and/or CNTs reinforced SiC CMCs using P-SHPB were investigated. The stress-strain curves exhibited typical behavior of brittle materials, and maintained linearity almost up to the peak fail load, indicating that the failure was mostly controlled by the fibers. The slight nonlinearity in some cases was due to micro matrix cracking and kinking of the fiber prior to final failure.

The results showed that thicker specimens and a higher impact energy (higher strain rate loading) tended to promote brittle behavior of the material as characterized by increased ultimate stress and compressive modulus. Strain rate was inversely proportional to specimen thickness, but positively dependent on impact energy. The energy absorption was found to be consistently increased with sample thickness and impact energy. The decreased particle velocity for thicker specimens was probably due to the hardening and embrittlement effect that slowed the particle motion, while the increased particle velocity with an increased impact energy was because of the greater load on the specimen that, in turn, caused greater vibration and propagation of the particles.

The results also highlighted the fact that increased temperature and moisture content degraded the mechanical properties of the ceramic composites. The maximum reduction of ultimate stress due to the increase of temperature from 24-500 $^\circ$C was about 9.8%, while the maximum ultimate strain increment in this range was 8.1%. A severe degradation of the materials' strength was found from 400-500 $^\circ$C. Negligible difference was found for the two blends of dry samples, but the maximum degradations of failure strength for Blend #1 and Blend #2 at the equilibrium water content were approximately 9.2% and 6.9%, with the corresponding

95

failure strain increments of 7.9% and 5.8%. Both the strain rate and energy absorption were increased with temperature and water content. In the hostile environment, microcracks developed in the matrix due to thermoelastic residual stress or water penetration, which would lower the energy absorption needed to initiate and propagate the damage. The particle velocity was slightly increased with temperature while it remained stable for the wet speciments. Highly cracked patterns radiating from the impact point was observed and the equivalent fragment size was between 6.19 mm to 9.10 mm in the strain rate range of 168-312 1/s, and generally decreased with the increase of strain rate.

5.0   DYNAMIC FRACTURE TOUGHNESS OF TAC/CNTS/SIC CMCS

5.1   INTRODUCTION

Based on the framework of 1.3.4, the purpose of this chapter is to develop a better understanding of the mechanics of fracture of ceramic composites in impact from quasi-static to dynamic, as well as the possibility of toughening with CNTs reinforced silicon carbide ceramics. In this study, we have employed Vickers indentation to measure the static fracture toughness on the polished surface of ceramic samples, SEM to directly observe the crack propagation after indentation, and SHPB to determine the dynamic fracture toughness within the ceramic samples subjected to an impact in a three-point bending configuration. The work is novel in that the SHPB apparatus allowed accurate measurement of velocity, force, and energy absorption information for the entire impact duration using the recorded incident, reflected, and transmitted stress waves.

As carbon nanotubes present excellent Young's modulus, good flexibility, low density, and exceptional electrical and thermal performance in general, they have been considered as one of the most promising nanoscale reinforcements for polymers, metals, and ceramics [215-217]. Among which, the CNTs reinforced ceramics with improved fracture toughness and material properties have attracted intense global research since they have increasingly been applied in impact related areas such as aerospace and ballistic armors [89]. Accurate understanding and

determination of the dynamic fracture toughness at high strain rate conditions is of significant importance for the assurance of the integrity and safety of structural components subjected to impact loading.

Investigators attempted to extent the quasi-static ASTM standard into dynamic loading range through various high rate bending techniques. The specimens were designed as three- or four-point bending of precracked beams, while the dynamic loading was applied using a modified split Hopkinson pressure bar (SHPB), a drop weight tower, or a modified Charpy tester [218]. Geary et al. [219] studied the dynamic fracture toughness under different strain rates of glass reinforced polymer, using three-point bending specimens, and they reported that the dynamic fracture toughness is higher than the static one, owing to different failure modes. Jiang et al. [220] employed the Hopkinson pressure bar to determine the dynamic fracture toughness parameter at a loading rate exceeding 10^6 MPa m$^{1/2}$/s. Samborski [221] compared the static and dynamic fracture toughness values for alumina and magnesia ceramics, and investigated the effect of porosity on the fracture toughness and found that the increase of initial porosity reduces the values of both static and dynamic fracture characteristics. Rubio-Gonzalez, et al. [222] tested the dynamic fracture toughness for two composite materials by means of an instrumented Hopkinson bar with precracked specimens loaded on a three-point bending configuration. The dynamic fracture toughness in this study was determined from the critical dynamic stress intensity factor at the onset of crack initiation. Up until now, there has not been a complete standard to characterize and measure dynamic fracture toughness of ceramic materials, this owing to both the difficulties in dynamic fracture theory and experimental techniques [223-224].

5.2   FRACTURE MECHANICS OF CERAMICS

The strength of composite materials is always governed by the flaw-initiated characteristics, as these microcracks cause a reduction in stiffness and provide sites for fracture. Therefore, the mechanics of fracture including crack initiation and propagation are of extreme importance in design and analysis of structural materials. The property commonly measured in the fracture mechanics study is fracture toughness, which is defined as the resistance of a material to failure from a fracture, starting from a pre-existing crack. Fracture toughness values are used extensively to characterize the fracture resistance of ceramics and brittle materials. The fracture of brittle ceramics is usually controlled by the mode I fracture toughness.

It is generally considered that the Griffith [225] fracture mechanics was the first to introduce a powerful criterion to predict crack propagation for many types of materials. According to Griffith's theory, when a centrally cracked panel (Fig. 5-1) is subjected to a uniform axial stress σ, the energy absorbed ΔU_A by the plate due to the growth of a crack of $2a$ length is given by:

$$\Delta U_A = \frac{\pi \sigma^2 a^2 t}{E} \tag{1}$$

where t is the thickness of the plate, and E is the young's modulus. If S is the surface energy of the two new surfaces created by the crack, then

$$S = 4\gamma a t \tag{2}$$

where γ is the surface tension of the material.
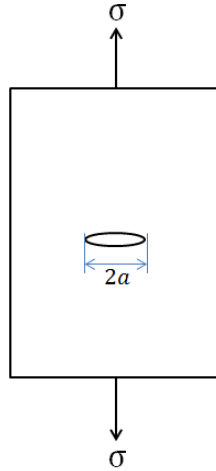
Fig. 5-1 Centrally cracked panel under uniform axial stress σ

Eq. (1) shows that, if σ is increased, more stored elastic strain energy will be available to propagate the crack. Obviously, this crack-driving force is opposed by an equilibrium resistance of the materials. When the rate of increase of the crack-driving force with respect to crack length is equal to the rate of increase of the resistance, the crack becomes self-propagating. This unstable or critical condition can be defined as:

$$\frac{\partial(\Delta U_A - S)}{\partial a} = 0 \tag{3}$$

or,

$$\sigma_c = \left(\frac{2E\gamma}{\pi a}\right)^{1/2} \tag{4}$$

Irwin [226] used linear elastic stress analysis theory to show that in an infinite plate the strain-energy release rate G_{Ic} is related to critical stress intensity K_{Ic} at the crack tip in the following expression:

$$EG_{Ic} = K_{Ic}^{2} = \pi a \sigma_c^{2} \tag{5}$$

In the case of dynamic fracture toughness, it is assumed that the specimen has reached a state of uniform stress at a constant energy consumption rate. The term of energy absorption

(ΔU_A) can be determined from classical wave mechanics [227]. After the impact of a striker bar with the incident bar, a fraction of the compressive wave generated is reflected at the surface of the sample and others are transmitted through the sample. An elastic wave traveling through the specimen for time t pumps this energy into the crack tip in the direction of crack propagation. Thus, neglecting energy losses within the fixture, the total energy lost in the impact or the energy absorbed for the fracture process can be calculated by subtracting the energy transmitted and reflected from the incident wave:

$$\Delta U_i = \frac{A_b c}{E} \int_0^t \sigma_i^2(t) \, dt$$

$$\Delta U_r = \frac{A_b c}{E} \int_0^t \sigma_r^2(t) \, dt \tag{6}$$

$$\Delta U_t = \frac{A_b c}{E} \int_0^t \sigma_t^2(t) \, dt$$

where ΔU_i is the incident energy due to the incident compressive wave, ΔU_r is the surface strain due to the reflected wave, resulting from surface impedance mismatch, ΔU_t is the internal strain energy in the specimen, A_b is the cross sectional area of bars, c is wave velocity in the bars, E is young's modulus of the bars, and σ_i, σ_r and σ_t are incident, reflected and transmitted stress, respectively. Thus, energy dissipated in the dynamic fracture can be expressed as:

$$\Delta U_A = \Delta U_i - \Delta U_r - \Delta U_t \tag{7}$$

Substituting Eq. (6) into (7) gives the total energy dissipated in the fracture process as:

$$\Delta U_A = \frac{A_b c}{E} \int_0^t [\sigma_i^2(t) - \sigma_r^2(t) - \sigma_t^2(t)] dt \tag{8}$$

Dynamic fracture mechanics is the subfield of fracture mechanics concerned with fracture phenomena for which the role of materials inertia becomes significant. Inertial effects may arise either from applied loading on a cracked material or from rapid crack propagation. Test methods for measuring the fracture toughness for ceramics are well established (ASTM C

1421, ASTM STP 1409, and NIST SRM 2100). However, currently no appropriate high strain rate test standard exists due to the obstacles of dynamic effects induced at a high strain rate. It was reported by Bohme et al. [228] that the specimen jumped off the supports when the loading point was impacted on the three-point bending configuration, which revealed significant vibration coupled with the sudden bending deformation. Furthermore, the local stress/strain fields near the crack tip were not in phase with the far-field forces measured from the bars if the loading rate was not constant. Quasi-static equations relating the far-field peak loading to fracture toughness are therefore no longer valid [218]. It is critical that these effects are carefully considered for the valid measurement of dynamic fracture toughness (K_{Id}), such that the vibration of the stress/strain field near the crack tip is minimized and the loading rate at the crack tip is nearly constant.

5.3 EXPERIMENTAL PROCEDURE

5.3.1 Vickers indentation

Vickers indentation was conducted by the Microindentation Tester LM800 (Leco, MI, USA), with a diamond in the form of a square-based pyramid indenter. The Vickers hardness HV is calculated as the mean contact pressure, i.e. load divided by projected area:

$$HV = \frac{F}{A} \approx \frac{1.854F}{d^2} \tag{9}$$

where F is the loading force, and d is the average length of the diagonal left by the indenter. To avoid border effects, the thickness of the sample should be at least 10 times thicker than the indentation depth [229].

For brittle ceramic materials, mode I fracture toughness, K_{IC}, can be calculated according to Anstis et al. [230]:

$$K_{IC} = 0.016\sqrt{\frac{E}{HV}}\frac{F}{c^{3/2}} \qquad (10)$$

where E is the Young's modulus and c is the crack length from the impression center (Fig. 5-2). The crack length used in Eq. (10) is the average of all four cracks from the indentation. The crack length is measured using SEM (Philips XL 30 FEG).
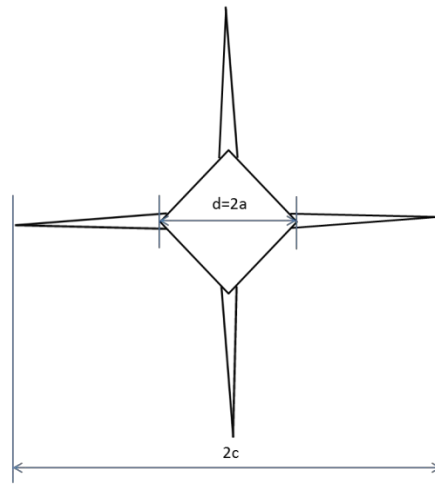
Fig. 5-2 Crack created by the Vickers indenter

5.3.2 Dynamic fracture toughness setup

The ASTM C1421-10 three-point bending test is one of the simplest methods for determination of the fracture characteristics of advanced ceramics at an ambient temperature. The specimens were prepared according to the precracked beam method, with a straight-through precrack created in the beam via bridge-flexure technique. The most important issue among those interested in plane strain fracture toughness testing is the specimen size required for a valid K_{IC} test. The precrack should be less than 0.10 mm in thickness and should have a normalized

crack size within the following range $0.35 \leq a/W \leq 0.60$. As the specimens used in this study are very brittle, no further fatigue crack is induced beyond the precrack because the brittle crack may initiate from the highly stress-concentrated area at the notch tip. For three-point fixtures, choose the outer support span such as that of $4 \leq S_0/W \leq 10$. The details of the test specimen as well as the three-point fixtures are given in Fig. 5-3.
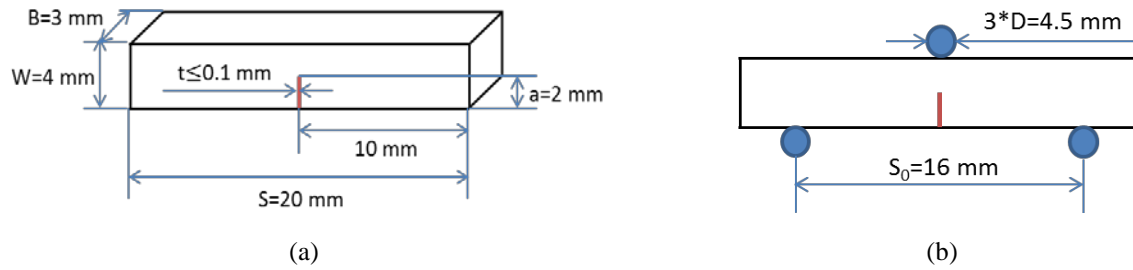
Fig. 5-3 (a) Schematic of the ceramic specimen; (b) Fixture configuration of the three-point loading

The dynamic experiment of fracture toughness testing was carried out on a modified SHPB with a deformable pulse shaper to obtain the dynamic equilibrium and constant loading rate [231]. Upon impact by the striker bar, the plastic deformation of the pulse shaper continuously increases its effective diameter, which allows a correspondingly increasing momentum transfer from the striker bar to the incident bar, thus generating an incident pulse with increasing amplitude. This incident waveform can be tuned by varying the pulse shaper material and dimensions. Pulse shapers are generally disks, rings, or tubes made of materials such as rubber, polymers, or metals. Among these, copper shapers are the most popular ones. In this research, an annealed copper disk of 3.2 mm diameter and 3.2 mm thickness was used for placement at the impact end of the incident bar. The three-point fixtures were glued on the bar-specimen ends. A small amount of preloading was necessary to hold the specimen in position

between the fixtures, which was achieved by two rubber bands tensioning the two bars to close

on the specimen. A schematic of the modified SHPB experimental setup is shown in Fig. 5-4.
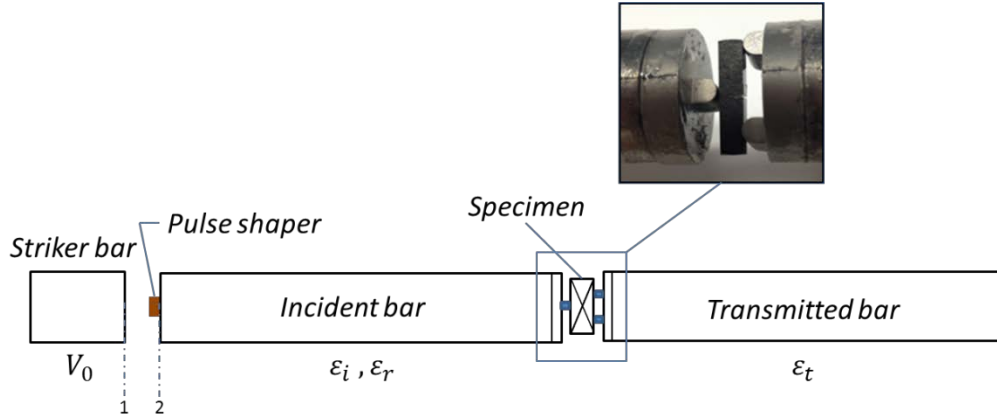
Fig. 5-4 Schematic of the modified SHPB setup for fracture toughness

As the experiment was designed in such a way that the specimen deformed under

dynamic equilibrium at a nearly constant loading rate, the dynamic fracture toughness could be

evaluated using the quasi-static method expression:

$$K_{IC} = f(a/W)[\frac{P_{max}S_o10^{-6}}{BW^{3/2}}][\frac{3(a/W)^{1/2}}{2(1-a/W)^{3/2}}] \tag{11}$$

where:

$$f(a/W) = \frac{1.99-(a/W)(1-a/W)[2.15-3.93(a/W)+2.7(a/W)^2]}{1+2(a/W)} \tag{12}$$

P_{max} is the maximal dynamic force, S_o is the three-point test fixture outer span, B is the side to

side dimension of the test specimen, W is the top to bottom dimension of the test specimen

parallel to the crack length, and a/W is the normalized crack size.

5.4 THEORETICAL FORMULAE FOR MODIFIED SHPB

With the annealed copper disk attached on the impact end of incident bar in the classical SHPB apparatus shown in Fig. 5-4, one must consider the pulse shaper effect. Upon being impacted by the striker bar, a compressive stress wave is generated in the pulse shaper which, after several reflections off its ends, yields a dynamic equilibrium. According to Frew [232], the force equilibrium at interfaces 1 and 2 can be expressed as:

$$P_1(t) = \sigma_{st}(t)A_{st} = \sigma_i(t)A_b = P_2(t) \tag{13}$$

where P_1 is the force at interface of striker bar and pulse shaper, σ_{st} is the stress in the striker bar, A_{st} is the cross sectional area of the striker bar, σ_i is the stress in the incident bar, A_b is the cross sectional area of the incident bar, and P_2 is the force at interface of the pulse shaper and the incident bar.

Consider the same diameter of striker bar and incident bar in this apparatus, $A_{st} = A_b$, from Eq. (13) as follows:

$$\sigma_i(t) = \sigma_{st}(t) = \frac{\sigma_p(t)A_p(t)}{A_b} = \frac{\sigma_p(t)A_{p0}}{A_b(1-\varepsilon_p)} \tag{14}$$

where σ_p and ε_p are the instant pulse shaper stress and engineering strain, A_{p0} and A_p are the initial and instant cross sectional area of the pulse shaper.

The velocity at interfaces 1 and 2 are given as:

$$v_1(t) = V_0 - v_{st}(t) = V_0 - \frac{\sigma_{st}(t)}{\rho_{st}c_{st}} \tag{15}$$

Substituting σ_{st} from Eq. (14) yields:

$$v_1(t) = V_0 - \frac{A_{p0}}{\rho_{st}c_{st}A_b}\frac{\sigma_p(t)}{(1-\varepsilon_p)} \tag{16}$$

where V_0 is the initial velocity of the striker bar, v_{st} is the instant velocity of the striker bar, ρ_{st} is the striker bar density, and c_{st} is the wave velocity in the striker bar.

$$v_2(t) = v_i(t) = \frac{\sigma_i(t)}{\rho c} \tag{17}$$

Substituting σ_i from Eq. (14) yields:

$$v_2(t) = \frac{A_{p0}}{\rho c A_b} \frac{\sigma_p(t)}{(1-\varepsilon_p)} \tag{18}$$

where v_i is the particle velocity in incident bar, ρ is the density of the incident bar, and c is the wave velocity in the incident bar.

The pulse shaper strain rate can therefore be calculated from the particle velocities at interfaces 1 and 2 as:

$$\dot{\varepsilon}_p(t) = \frac{v_1(t)-v_2(t)}{L_{p0}} \tag{19}$$

where L_{p0} is the initial length of pulse shaper.

Performing this calculation entails knowledge of the constitutive equation of the pulse shaper material and the relation between incident stress and the stress in the pulse shaper. The wave mechanisms with the modified SHPB system are analyzed to determine the instant force in the dynamic fracture toughness test, which is given by the following equation:

$$P(t) = \frac{[\sigma_i(t)+\sigma_r(t)]A_c}{2} \tag{20}$$

where σ_i is the incident stress, σ_r is the reflected stress, and A_c is the contact area between specimen and fixture on the incident bar. In the experimental setup, the impactor and the specimen respond to the compressive stress pulse. From Eq. (20), the force-time curve can be obtained, and the maximum force will be used to determine the dynamic fracture toughness K_{Id} by ASTM C1421-10 standard procedure.

5.5   RESULTS AND DISCUSSION

5.5.1   Samples response to the dynamic loading

The batches of precracked samples [Fig. 5-5(a) left] made of TaC and CNTs reinforced SiC composites were tested at different energy impacts. A collection of representative specimens, which failed under a 770 mJ impact energy for the three-point dynamic fracture test, are shown in Fig. 5-5(a) and (b).

(a)   (b)

Fig. 5-5 Samples for the dynamic fracture tests (a) sample before test, (b) sample after test

The ideal incident pulse for achieving a constant strain rate would be one where the leading part is of short duration up to an amplitude which just allows the specimen to yield, after which the amplitude should increase at a lower rate more appropriate to the reduced modulus [218]. Fig. 5-6 shows the incident, reflected, and transmitted strain pulses determined from the measured strain signal using appropriate system calibration. The waveform is controlled as a nearly linear ramp and captured at a sample rate of 250,000 samples/sec. The nearly constant slope of the incident and reflected strain wave reveals that the loading rate is nearly constant and

the specimen deforms under dynamic equilibrium during the fracture test. The transmitted strain wave is very small due to the extreme mismatch between the rigidity and mechanical impedance between the precracked specimen and the bars.
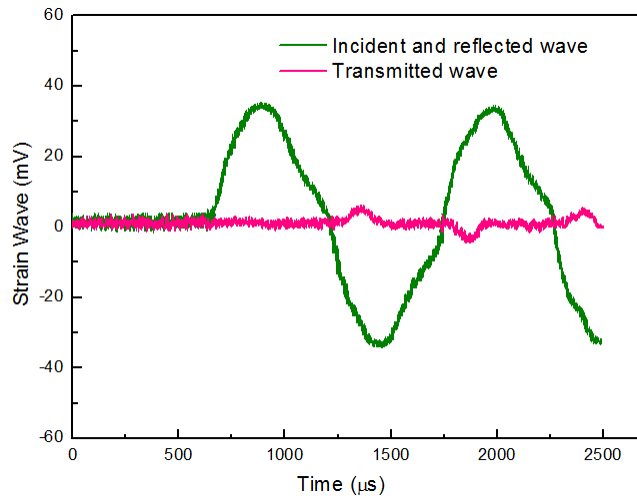
Fig. 5-6 Strain waveform for the dynamic fracture test

The strain wave pulses provide information for the complete characterization of the dynamic fracture process. Fig. 5-7 displays the time history of energy absorbed by the three-point bending configuration to develop the cracks. The fracture energy absorption increases with time as the crack propagates, and then decreases when approaching an unstable crack propagation state (after 215 µs). This is because, at this energy, the crack length has more than exceeded the critical crack length, at which point the potential energy exceeds the fracturing energy. Thus, the fracture energy absorbed decreases since more energy is released than consumed by the crack growth, and crack propagation is less stable and dissipates less energy during the period of rapid propagation than during initiation.

The variation of the force-time curve in Fig. 5-8 shows a nearly constant slope before the loading reaches its peak value, which reveals that the fracturing is under dynamic equilibrium.

Therefore, the loading history can be related with the stress intensity factor history near the crack tip. The peak force is assumed as the fracture initiation point, and after that, the crack propagates. There are multiple peaks and large oscillations on the force-time curve during crack propagation, owing to the fracture mechanisms, such as crack deflection and crack bridging, which prevent crack propagation.
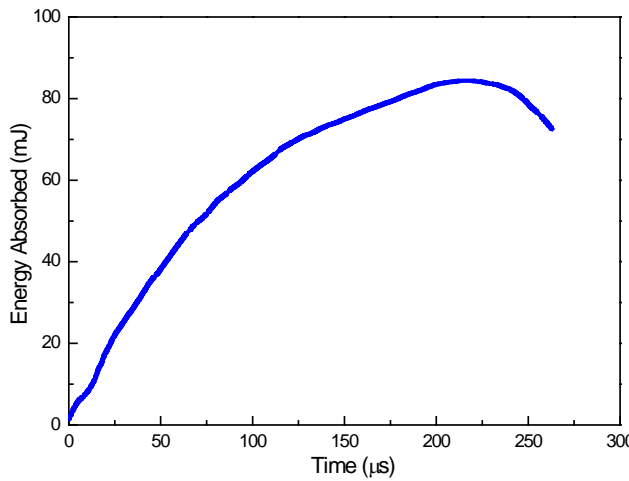
Fig. 5-7 Energy absorption time history for the dynamic fracture test
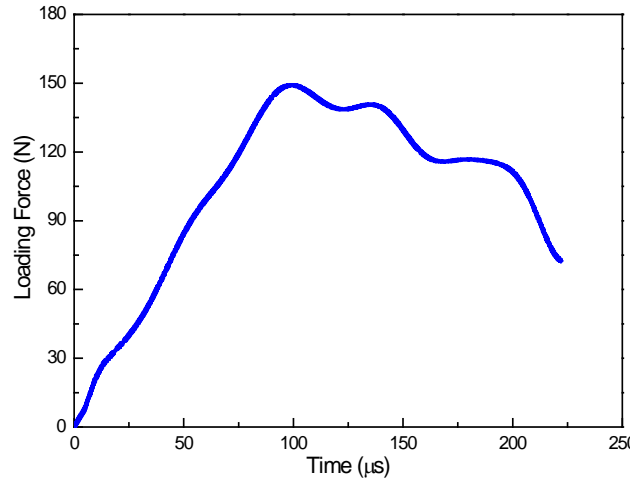
Fig. 5-8 Loading force time history for the dynamic fracture test

5.5.2 Effect of strain rate on fracture toughness

The calculated fracture toughness values for both static and dynamic cases, K_{IC}, are summarized in Table 5-1. As impact energy though the striker bar generates the strain rate effect on the material properties, such as strength and stiffness, strain rate sensitivity is controlled and defined for a fracturing study in this research. Fig. 5-9(a) shows that the variation of maximum energy absorption generally increased linearly with strain rates. At a higher strain rate or as more

energy is transferred to the system, maximum energy absorbed in the dynamic fracture process increases, which implies that more energy is available in the crack tip area to initiate the crack.

As the peak force is used to calculate the fracture toughness, K_{IC}, according to Eq. (11), Fig. 5-9(b) and (c) present the same nonlinear variation trend for peak loading force and fracture toughness with strain rates. At a lower strain rate of 51.0 1/s or where the impact energy was just to initiate and propagate the crack, the TaC and CNTs reinforced SiC composites had an average fracture toughness value of 4.71 MPa·m$^{1/2}$. When increasing the strain rate to 69.8 1/s, the calculated average fracture toughness increased to 5.45 MPa·m$^{1/2}$. Sharply, the average fracture toughness increased to 8.36 MPa·m$^{1/2}$ at a strain rate of 90.4 1/s. Generally, the increase was linear with strain rates. At a higher strain rate or as more energy is transferred to the system, maximum energy absorbed in the dynamic fracture process increases, which implies that more energy is available in the crack tip to initiate the crack.
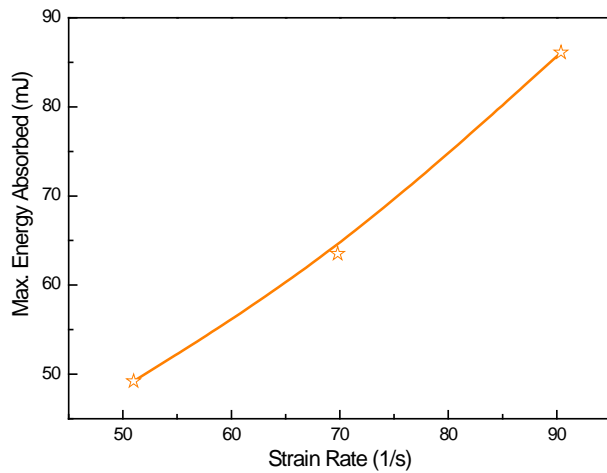
(a)
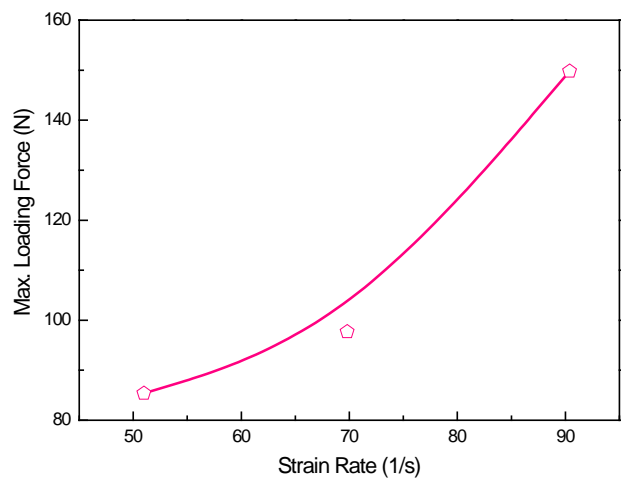
(b)
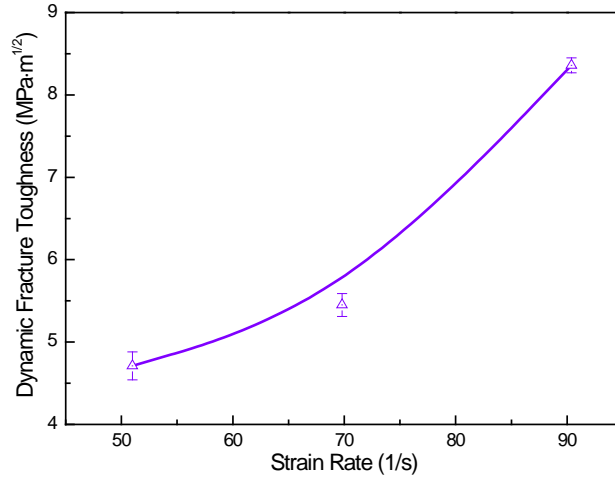
(c)

Fig. 5-9 (a) Variation of maximum energy absorbed with strain rate, (b) Variation of maximum loading force with strain rate, and (c) Variation of fracture toughness with strain rate

Table 5-1 Summary of results of fracture toughness

Impact Energy (E_I, mJ)	Vickers Hardness (HV, GPa)	Strain Rate ($\dot{\varepsilon}$, 1/s)	Maximum Energy Absorbed (ΔU_A, mJ)	Maximum Loading Force (P_{max}, N)	Fracture Toughness (K_{IC}, MPa·m$^{1/2}$)
Static	24.55 ± 1.32	/	/	/	3.88 ± 0.28
445	/	51.0	49.2	85.4	4.71 ± 0.17
790	/	69.8	63.5	97.7	5.45 ± 0.14
1235	/	90.4	86.1	149.8	8.36 ± 0.09

For many materials with strong strain rate dependence, the fracture toughness usually increases with an increasing strain rate, and is very sensitive to a strain rate in a certain loading range. Fracture toughness should therefore be evaluated in the region where it may show a relatively low and stable value, and the conditions that reveal the transition from high to low values of fracture toughness should be investigated. Knott [233] and Klepaczko [234] have defined the loading rate parameter $\dot{K}_I$ to express how fast the crack tip region is loaded:

$$\dot{K}_I = \frac{K_{IC}}{t_c} \tag{21}$$

112

where t_c is the time interval from the start of loading to the point when stable crack propagation starts. The stress intensity factor for both static and dynamic tests is calculated according to Eq. (21). The value for the static case is 0.39 MPa·m$^{1/2}$/s, while it ranges from 2.66×10^4 to 8.36×10^4 MPa·m$^{1/2}$/s for dynamic cases. The dependence of fracture toughness on the loading rate is shown in Fig. 5-10.

In general, the fracture toughness of the SiC composites increases with strain rate, and exhibits a more strain rate dependent property for higher strain rate. As the strain rate effect is an intrinsic material property, this could be explained by the limited small crack propagation velocity [218]. Fracture occurs only when the critical crack length is achieved by the propagation of small cracks. The small cracks can be very rate sensitive (e.g., below the Rayleigh wave speed), and it takes a finite amount of time for those small cracks to grow into the critical length. Although more energy is accumulated in the crack tip with increased strain rate, the propagation time for the small cracks to initial the fracture is the same.
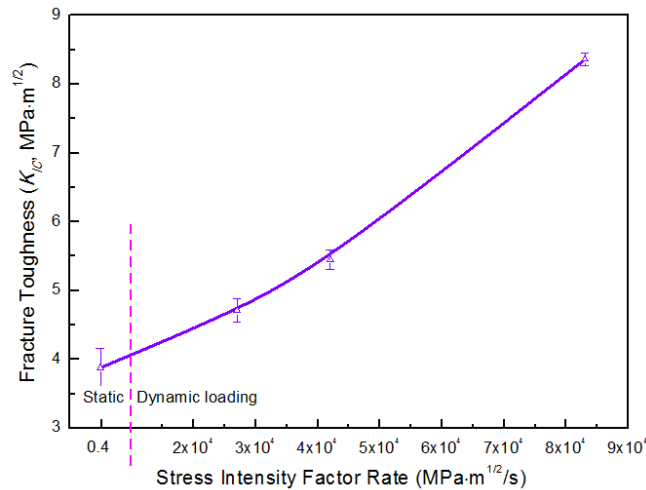
Fig. 5-10 Variation of fracture toughness with the loading rate

5.5.3 Fracture mechanisms

Ceramics are brittle at room temperature because the stress required for dislocation movement is higher than the fracture stress and, thus, fracture takes place. The published fracture toughness for SiC is 3.1 MPa·m$^{1/2}$ [235]. The SiC CMCs exhibit a higher fracture toughness when compared to the monolith SiC, owing to the frequently occurring toughening mechanisms during the crack propagation by reinforcements. The structural stability of the CNTs is essential for the fracture toughening to occur. In spark plasma sintering, the CNTs were subjected to the most severe conditions of heat, pressure, and current, but were found to be retained with their cylindrical structure intact, as reported in Chapter 2.

The path of cracks arising from the indentation on the composite is illustrated in Fig. 5-11, The cracks initiated from the tip area of the indentation and extended forward radially. Surface flaws and internal pores often act as stress concentrators and initiate cracks. Cracks propagate when the plastic flow at the tip of a crack is insufficient to absorb enough energy to stop the crack. However, the surface flaw behaved as a crack stopper for the left hand side main radial crack, as shown in the figure. This is because the presence of a surface flaw has relaxed the stress field in the vicinity of the crack tip, where not enough stress is left for moving dislocations. Also observed are some secondary radial cracks, which may have relieved some residual stress and decreased the crack opening as reported by Cook and Pharr [236].
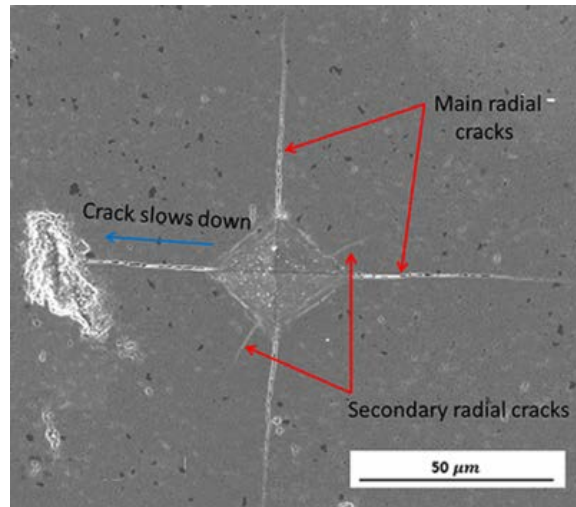
Fig. 5-11 SEM showing the crack path by Vicker's indentation

Photographic examination of the fracture surfaces revealed different toughening mechanisms due to the presence of CNTs, as shown in Fig. 5-12. The main toughening mechanisms observed are crack deflection and crack bridging. A higher magnification SEM micrograph of the two toughening mechanisms is displayed in Fig. 5-13. Crack deflection is a very frequently observed toughening mechanism in all investigated samples, and it is the interaction between cracks and CNTs. The interface of CNTs/matrix has a relatively lower toughness, compared to that of crack propagation through the reinforced particle cross-section, which is preferable for crack deflects.

CNTs bridging is the crack propagates perpendicular to the axial direction of the CNTs, and then the CNTs stretch freely along the separating crack faces, in such a way as that restrains the crack from opening and reduces the driving force for crack propagation in the matrix. The bridging is consistent with the crack deflection, where perpendicular cracks reach the CNTs/matrix interface and propagate along the interface rather than cut the grains. Thus, the CNTs are able to remain intact to bridge the crack and provide toughening via restraining forces acting against the desire of the crack to open and to grow further under the indentation load [100].
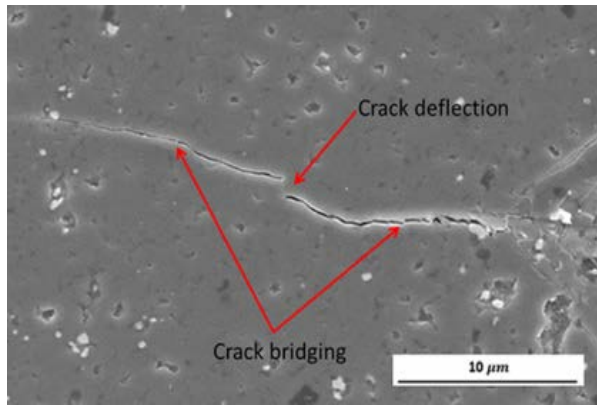
Fig. 5-12 Toughening mechanisms in the SiC composites
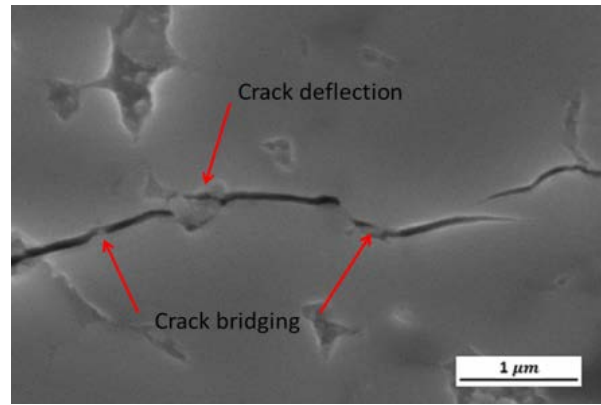
Fig. 5-13 Higher magnification showing the toughening mechanisms

5.6   CONCLUSIONS

The dynamic fracture toughness of TaC and CNTs reinforced SiC CMCs as a function of loading rate was investigated by the modified SHPB apparatus based on the quasi-static fracture toughness ASTM C1421-10 three-point bending standard for advanced ceramic materials. An annealed copper pulse shaper was successfully applied to SHPB to achieve the dynamic equilibrium and constant loading rate, which enabled to relate the fracture toughness at the crack tip to the far-field peaking loading through quasi-static equation.

The dynamic fracture toughness for SiC composites was 4.71-8.36 MPa·m$^{1/2}$, which was higher that the quasi-static toughness of 3.88 MPa·m$^{1/2}$. Variation of strain rate revealed that peak energy absorbed by the system to initiate the crack generally increased linearly with increased strain rates, while peak loading force increased nonlinearly with increased strain rates, as was the case with the fracture toughness. It was found that the SiC composites exhibited a more strain rate dependent property for a higher strain rate. At a higher strain rate, or as more

energy was transferred to the system, more energy was absorbed in the crack tip area to initiate the crack, but the propagation time for the small cracks to initial the fracture may be the same.

Fracture toughening mechanisms of CNTs deflection and CNTs bridging were directly observed by SEM. Though the interaction between cracks and the CNTs/matrix interface, perpendicular cracks deflected along the interface, or CNTs bridged the crack, restraining the crack from opening and growing further under the indentation load.

6.0   NUMERICAL AND EXPERIMENTAL ANALYSIS OF SHPB

6.1   INTRODUCTION

To address framework 1.3.5, this chapter is meant to study and predict the behavior of the laminated composites during a high strain rate impact event. The FE software ABAQUS/Explicit is employed to perform the user subroutine implemented numerical modeling of the composites under the SHPB test. In particular, it is of interest to predict the progressive damage behavior and estimate the resulting damage extent of laminates under the dynamic impact process. By comparison of the numerical and experimental results, it is hoped that this work provides reliable prediction of the extent of failure damage, which in turn forms the basis for prediction of the residual strength of the impact induced failure in composite structures.

The split Hopkinson pressure bar (SHPB) has been widely used to measure the dynamic properties at a high strain rate. The response of composite materials in terms of damage and fracture to the dynamic loading includes transverse matrix cracking, fiber breakage, fiber-matrix interface failure, and delamination [237-238]. In light of the complexity of high strain rate impact issues, it is not surprising that both experimental and numerical views are employed. Allazadeh and Wosu performed high strain rate compressive tests on woven graphite/epoxy laminates [239-240]. Siviour [241] used the split Hopkinson pressure bar to measure wave propagation in a rod of PMMA. Vinson [242] studied the effects of fiber orientation on the strain

rate properties of unidirectional graphite/epoxy composites and found that changing the fiber orientation affected the ultimate strength and strain of (IM7/8551-7) graphite/epoxy composites. Methods for simulating composite impact events were also researched. Nguyen performed a review of explicit finite element (FE) software for composite impact analysis. The FE packages considered, ABAQUS/Explicit, LS-DYNA, and Pam-Shock, were found to be capable of creating a composite damage model, running a damage-inducing dynamic loading event, and post-processing the failure information [108]. Patel et al. [243] studied the penetration of projectiles in composite laminates using 8-noded serendipity quadrilateral finite elements based on first-order shear deformation theory. Gu [244] utilized LS-DYNA to simulate the ballistic penetration of a steel projectile into a plain-woven fabric target, and applied 8-noded hexahedron elements to model the woven fabric explicitly. Nurhaniza et al. [245] used ABAQUS finite element software to determine the mechanical response of unidirectional E-glass.

The use of appropriate user-defined material models plays an important role in modeling the impact damage, controlling the extent of damage, energy absorption, stiffness reduction, and the final dynamic structural behavior. The Hashin failure criterion [113] is an interacting failure criterion as it uses more than a single stress component to evaluate different failure modes. The Hashin criterion was originally developed for unidirectional fiber composites in terms of quadratic stress polynomials, and then applied to other laminate types or non-polymeric composites for approximation. The advantage of using the Hashin failure criterion is that it identifies the failure modes independently, namely, tensile and compressive fiber failure, tensile and compressive matrix failure, and interlaminar tensile failure, resulting in a piecewise smooth failure.

6.2   SHPB IMPACT EXPERIMENT

The FE analysis is based on the conventional SHPB setup used to impact the thin composite laminates. Fig. 6-1 shows a schematic of the test setup. It consists of a striker bar, incident bar, laminate specimen, transmitted bar, and transmitted bar support. The bars are fabricated from maraging steel. The striker bar is housed inside a hollow tube which allows it to move only along its axis. The incident and transmitted bars are each supported on several pillow blocks which only allow motion in the axial direction. Diametrically opposed strain gauges located at the midpoints of the incident and transmitted bars are used to measure strain during the experiment. The transmitted bar support consists of a thick steel angle section with a plastic stopper that seats against the transmitted bar. All of the pillow blocks and the transmitted bar support are fixed to a stiff structural stand that minimizes vibration. The laminate is the fabric E-glass/epoxy (M10E/3783) composite plies with a stacking orientation of $[0]_S$. Table 6-1 presents the detailed information of the bars and composite laminate.
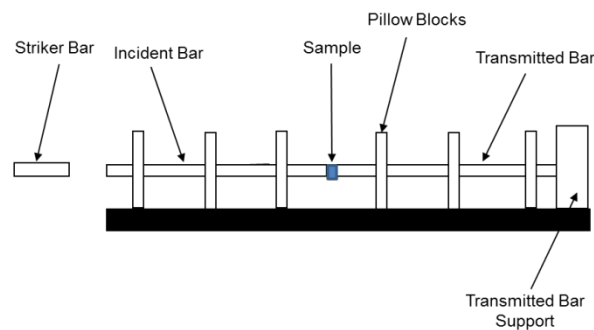
Fig. 6-1 Experimental setup for impact test

Table 6-1 SHPB setup and laminate specifications

Striker bar	L=0.6096 m, D=25.4 mm
Incident and transmitted bars	L=2.4384 m, D=25.4 mm
Composite laminate	17 mm * 17 mm
Fiber fraction	0.50
No. of plies	4
Ply orientation	$[0]_s$
Ply thickness	0.58 mm

6.3   NUMERICAL MODELING OF THE IMPACT BEHAVIOR

6.3.1   Progressive damage model

Composites have different failure modes under different loading conditions. Several failure theories can be found in literature, such as Maximum stress, Maximum strain, Tsai-Hill, and Tsai-Wu, which predict the failure of the composite laminates by prediction of the first ply failure [246]. These failure criteria typically underestimate the strength since it is well known that composites can continue to carry on loads even after the first ply failure. Furthermore, most of these theories do not account for the transverse stress which cannot be neglected while modeling the impact. In order to accurately predict the response of the composite laminates under an impact event, the Hashin criterion is considered to model the failure initiation and propagation for different damage modes. In the Hashin criterion, failure initiates as long as one of the five criteria is met:

Fiber tensile failure ($\sigma_{11} \geq 0$):

$$e_{f,t} = (\frac{\sigma_{11}}{X_t})^2 + (\frac{\sigma_{12}}{S_{12}})^2 + (\frac{\sigma_{13}}{S_{13}})^2 - 1 \geq 0 \tag{1}$$

Fiber compressive failure ($\sigma_{11} < 0$):

$$e_{f,c} = |\frac{\sigma_{11}}{X_c}| - 1 \geq 0 \tag{2}$$

Matrix tensile failure ($\sigma_{22} + \sigma_{33} \geq 0$):

$$e_{m,t} = (\frac{\sigma_{22}+\sigma_{33}}{Y_t})^2 + \frac{\sigma_{23}^2-\sigma_{22}\sigma_{33}}{S_{23}^2} + \frac{\sigma_{12}^2+\sigma_{13}^2}{S_{12}^2} - 1 \geq 0 \tag{3}$$

Matrix compressive failure ($\sigma_{22} + \sigma_{33} < 0$):

$$e_{m,c} = \frac{\sigma_{22}+\sigma_{33}}{Y_c}(\frac{Y_c}{2S_{23}})^2 + (\frac{\sigma_{22}+\sigma_{33}}{2S_{23}})^2 + \frac{\sigma_{23}^2-\sigma_{22}\sigma_{33}}{S_{23}^2} + (\frac{\sigma_{12}+\sigma_{13}}{S_{13}})^2 - 1 \geq 0 \tag{4}$$

Delamination ($\sigma_{33} \geq 0$):

$$e_d = (\frac{\sigma_{33}}{Z_t})^2 + (\frac{\sigma_{13}}{S_{13}})^2 + (\frac{\sigma_{23}}{S_{23}})^2 - 1 \geq 0 \tag{5}$$

where the subscripts 1, 2, and 3 indicate fiber direction, matrix direction and thickness direction of the composite lamina, respectively, X_t and X_c are tensile strength and compressive strength in fiber direction, Y_t and Y_c are tensile strength and compressive strength in matrix direction, and Z_t is tensile strength in thickness direction.

When failure initiates in a particular mode, damage propagation is modeled by reducing the stiffness of the element, thereby reducing the loading carrying capability. Such progressive failure stratagem takes the advantage of predicting the damage mode independently and then degrading the appropriate material stiffness. The degradation rules applied in this research work are presented in Table 6-2.

Table 6-2 Degradation in material stiffness due to different damage modes

Failure mode	Degradation rule
Fiber tensile failure	Element delete
Fiber compressive failure	E_{11}, E_{22}, G_{12}, $G_{13}=0$
Matrix tensile/compressive failure	E_{22}, $v_{12}=0$
Delamination	E_{33}, G_{13}, G_{23}, v_{23}, $v_{13}=0$

6.3.2 FE model

For the validity of SHPB in the study of the dynamic behavior of materials, important assumptions are made: (1) The bars remain elastic during the impact test, (2) Wave propagation inside the bars is one-dimensional and non-dispersive, and (3) The composite plate undergoes homogenous deformation.

The simulation was conducted in the ABAQUS/explicit package with the implementation of a VUMAT user subroutine, which defined the orthotropic material constitutive equation, the Hashin failure criterion, and the degradation of stiffness. Due to the symmetry, only a quarter of the bars and specimen model was created. The reduced integration of C3D8R with an 8-noded solid element was used. Fig. 6-2 depicts the simplified FE meshed model of the SHPB system. The composite laminates were sandwiched in between the incident bar and transmitted bar without a striker bar, since the striker bar would only act as generating a stress pulse, or the initial velocity, which could be simplified as the initial boundary condition applied on the incident bar.
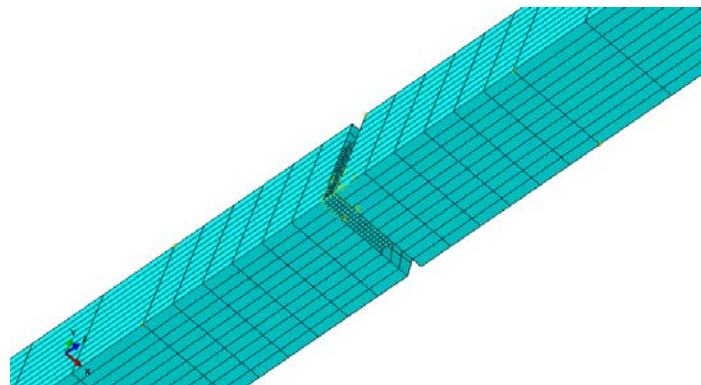
Fig. 6-2 3-D FE model

6.3.3 Boundary conditions

A prescribed stress pulse was applied to the impact end of the incident bar (Fig. 6-3), and symmetrical faces of bars and specimen were constrained by a symmetrical boundary condition. Hard contact with no friction was defined for the incident bar-specimen and specimen-transmitted bar surfaces. To determine an appropriate stress pulse, it is required that stress wave propagation distance should not exceed twice the length of the incident bar for the duration of the input stress pulse, which can be expressed as:

$$T_s < \frac{2L}{C} \tag{6}$$

where L is the incident bar length, C is wave velocity. Fig. 6-4 shows the time dependent stress pulse curve, and by selecting different T_a, T_b and T_s, different pulse shapes can be obtained. According to the actual impact process, a 300 µs duration stress pulse with 30 and 270 µs for T_a and T_b was defined.
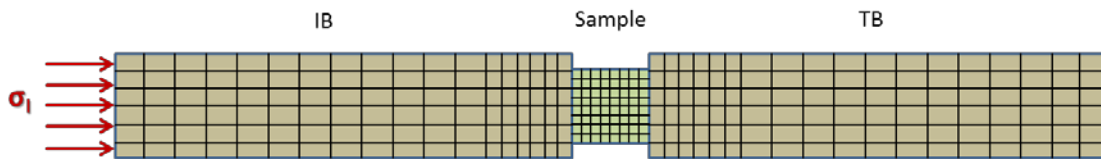
Fig. 6-3 Boundary conditions
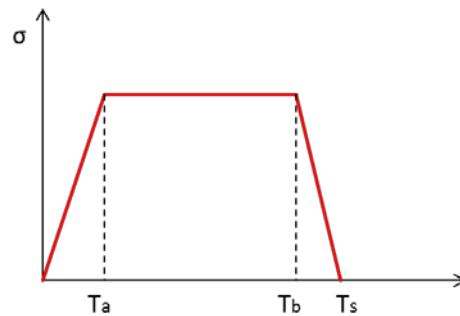
Fig. 6-4 Input stress pulse

6.3.4 Results and discussions

In order to monitor the wave propagation, points at the middle of the bars were assigned as based on the real experiment. The waves generated under an initial stress pulse of 150 MPa from both experiment and simulation are shown in Fig. 6-5. The simulated waveforms are quite similar to the experimental ones but without an apparent dispersion phenomenon [247]. This is due to an idea wave pulse and perfect bonding conditions between the bar surfaces and specimen surfaces were applied. The comparison of experimental and simulated waves also showed good consistence in the time taken for signal pulses to arrive at the middle of the bars, which validated the feasibility of the numerical SHPB system.
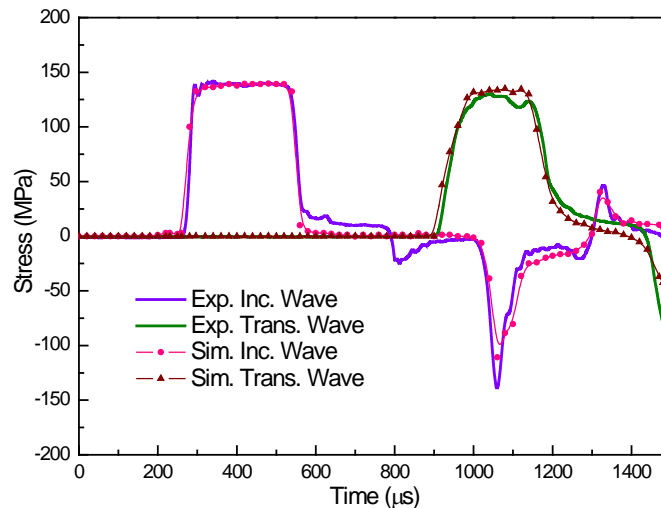
Fig. 6-5 Comparison of waves obtained by experiment and simulation

To further investigate the capacity of the simulation method to reproduce the dynamic response of composites in the SHPB test, evolutions of stress, strain rate, and energy absorbed are examined. Fig. 6-6 shows the comparison of strain rate history under an initial stress pulse of 150 MPa. In the experiment, strain rate reached its maximum value of 850 1/s in a very short

time, then dropped to 300 1/s around 100 μs and remained relatively constant for about 200 μs, and then the strain rate dropped to zero. The simulation generally predicted the strain rate behavior well, but with a lower maximum value (760 1/s) and a higher constant strain rate (360 1/s). As the strain rate behavior is revealed by the reflected wave, the characteristic time of strain rate can be analyzed in combination with the waveforms. In the first 100 μs, the wave propagates back and forth through the specimen for the first time, and there is no superposition in the reflected wave, so the reflected wave presents a rising edge that is nearly consistent with the incident wave. At this stage, stress equilibrium has not been achieved and the axial inertia effect cannot be ignored. From 100 μs to 300 μs, the reflected wave is nearly level, indicating that the strain rate remains approximately constant. Stress equilibrium has been achieved and the axial inertia effect can be ignored at this stage. Both the experiment and simulation showed a second peak on the strain rate curve, which corresponded to the damage in the composites [248].
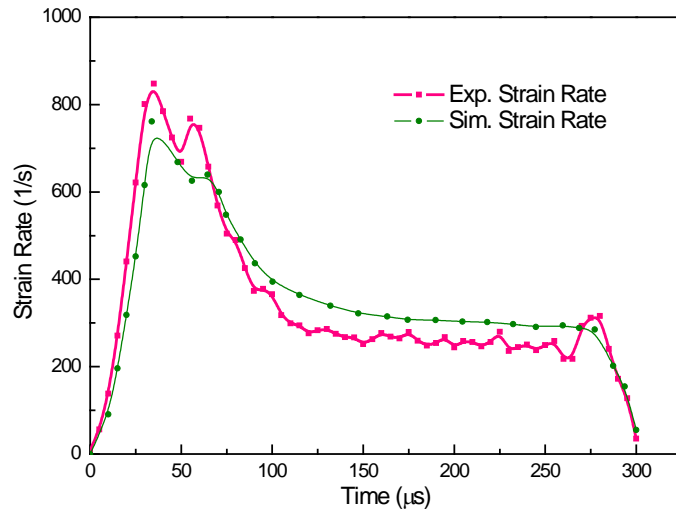
Fig. 6-6 Strain rate history

Fig. 6-7 shows the variation of energy in the specimen during the impact event. The peak value is the ultimate energy that was delivered by the SHPB for the damage process. After the

126

peak, strain energy is released and the residual energy will be absorbed by the composites. In the experiment, energy absorbed by the specimen was 3.18 J as compared with 2.90 J in the simulation. The higher energy level in the experiment resulted from the extra energy that was needed in overcoming friction and body force. Fig. 6-8 displays the comparison of stress-strain relationships. Numerical simulation predicts the overall variation of stress with strain fairly well. The ultimate stress and strain obtained in the experiment were 35.2 MPa and 0.42, while in the simulation were 38.9 MPa and 0.38.
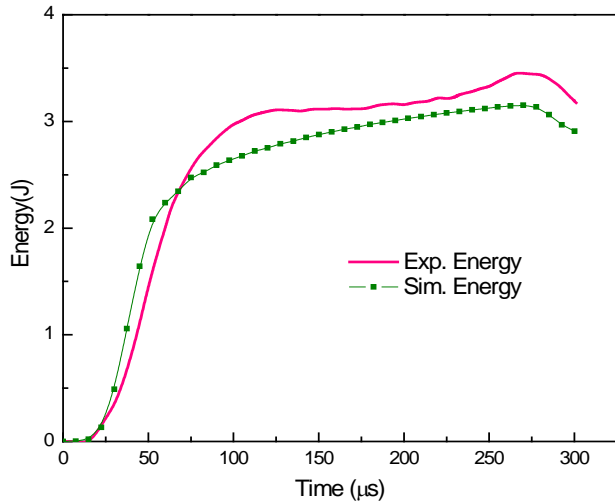
Fig. 6-7 Energy absorbed history
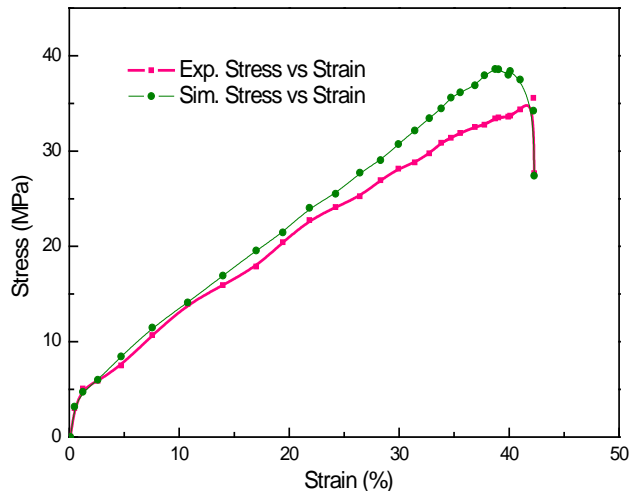
Fig. 6-8 Variation of stress with strain

Fig. 6-9 shows the projection of damaged elements (marked in red) of ply_1 of the composite plate under impact. It can be clearly seen that delamination is the most notable damage for laminates when subjected to transverse impact, followed by matrix failure, and fiber failure is the least. Compared with the impacted composite plate's surface in Fig. 6-10, numerical simulation predicted the damaged location fairly well. Table 6-3 lists the number of failed elements of each damage mode for each ply. It follows from ply_1 that delamination is the

most severe damage for each ply, while fiber failure is the least. It also can be found that ply_1 was subjected to delamination most, ply_4 was mainly under matrix tensile failure, and ply_2 seemed to undergo the least damage. Fig. 6-11 displays the delamination failure initiated at 80 MPa input stress pulse, and fiber tensile severely failed at 250 MPa input stress pulse, which caused the composite plate totally lost capacity for further loading.
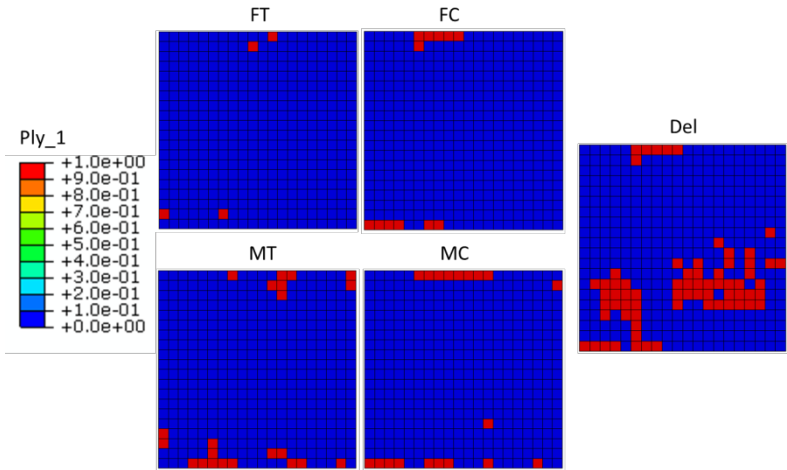
Fig. 6-9 View of the damaged elements (FT-fiber tensile failure, FC-fiber compressive failure, MT-matrix tensile failure, MC-matrix compressive failure, Del-delamination)

Fig. 6-10 View of the composite plate (ply_1) after impact

Table 6-3 Statistics of damaged elements of each damage mode for each ply

	FT	FC	MT	MC	Del
Ply_1	4	12	22	19	68
Ply_2	0	14	23	22	40
Ply_3	3	29	39	29	37
Ply_4	8	32	63	35	37

(a)   (b)
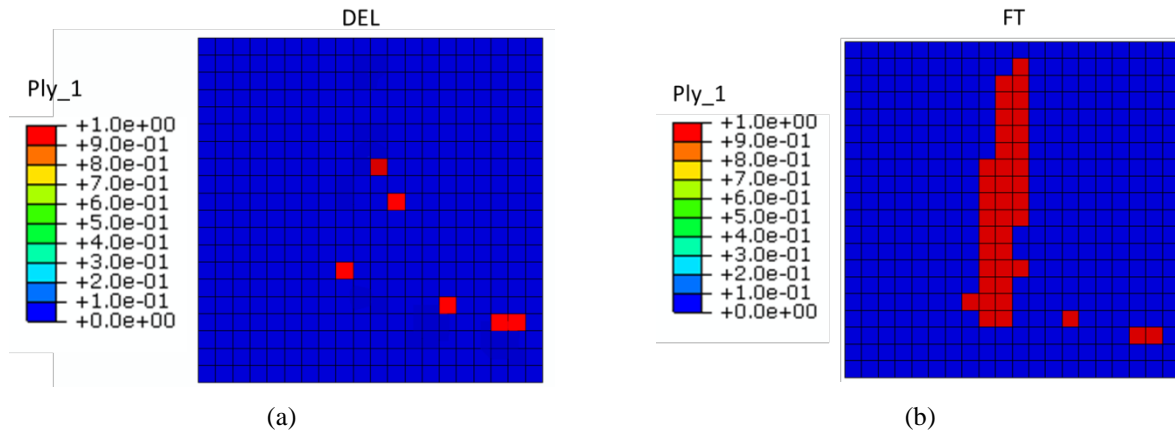
Fig. 6-11 (a) Delamination failure initiated at 80 MPa input stress pulse, and (b) fiber tensile severely failed at 250 MPa input stress pulse

6.4   CONCLUSIONS

Wave propagation in SHPB was investigated by ABAQUS in this research work, which validated the feasibility of the simplified SHPB model. Features of dynamic response on the composite plate, such as strain rate, energy absorption, and stress-train relations, were captured by the FE analysis. Failure initiation and the progressive damage model, accounting for stiffness degradation due to damage, was incorporated in the user-defined subroutine VUMAT in ABAQUS/explicit package. The numerical results generally showed good consistence with the

experimental ones. The differences probably resulted from the ideal initial stress pulse, perfect

boundary conditions, and the exact materials' properties in the numerical simulation process.

7.0   SUMMARY AND FUTURE WORK

7.1   SUMMARY OF RESULTS

In this dissertation, a new hybrid composite of TaC/CNTs/SiC was developed and fabricated through the SPS technique. Parametric study was carried out to investigate the densification behavior and mechanical properties. In order to reveal the change of the oxidation mechanism by adding TaC additives, a comparison group of TaC/CNTs/SiC (Blend #1) and CNTs/SiC (Blend #2) was examined. The high strain rate dynamic response of the composites was conducted by P-SHPB under various experimental conditions. Fracture toughness was determined both statically and dynamically, and fracture toughening mechanisms were also directly observed under SEM. Finally, wave propagation in SHPB was validated by numerical simulation and damage evolution of composites under transverse impact was predicted by a user-defined material subroutine VUMAT through ABAQUS/explicit. Here, the conclusions are drawn from each of the chapters.

In Chapter 2, reinforcements of TaC and CNTs, and sintering aids B_4C, were homogeneously distributed into the SiC matrix by ultrasonic agitation. Ceramic composites of TaC/CNTs/SiC and CNTs/SiC were successfully sintered by SPS. The addition of CNTs increased the densification of SiC from 86% to 99.5% while still maintaining submicron grain size under the sintering parameters of 133 ^{o}C/min heating rate, 1800 ^{o}C maximum temperature

and 90 MPa maximum pressure. Detailed analysis of punch displacement curves revealed that TaC additives did not favor the densification of CNT/SiC ceramics, owing to the larger size of TaC and low self-diffusion coefficient; however, TaC increased the hardness of the composites to some extent. The increase of heating rate gave rise to worse densification for both the TaC and/or CNTs reinforced SiC ceramics, and thus a negative effect in young's modulus and hardness as rapid heating rate may cause local temperature gradients and local uniformity. However, a higher heating rate had a clean effect on the mobility of the grain boundaries, which inhibited the grain growth. CNTs/SiC ceramics achieved a nearly full densification at an 1800 ^{o}C sintering temperature, but higher temperatures resulted in rapid grain growth and deteriorated mechanical properties. While, for TaC/CNTs/SiC ceramics, 1800 ^{o}C was not sufficient to get full densification due to the higher melting point of TaC. Raising the sintering pressure brought about increased densification with improved mechanical properties for both the composites by influencing the driving force for sintering. However, too high a pressure could have an inverse effect on the diffusion coefficient, which caused the growth of grain size.

In Chapter 3, the oxidation behavior of the as sintered SiC ceramics was investigated up to 1500 ^{o}C. Raman spectroscope analysis indicated that CNTs were retained but subjected to compressive stresses from heat, pressure, and electric current during SPS. More disorder occurred in the CNT network with an increased oxidation temperature, while the CNTs in Blend #1 were less disordered than those in Blend #2, implying a better oxidation resistance. The TGA results revealed that the addition of TaC in Blend #1 exhibited an enhanced protective effect in increasing the oxidation temperature of CNTs from 460 ^{o}C to 550 ^{o}C. Generally, three layers were detected for each oxidized cross section, which were the severely oxidized outer layer, the less oxidized middle layer, and the inner base material. When oxidized under 800 ^{o}C, Blend #2

132

exhibited more weight loss, and its oxidation resistance was attributed to the growth of a protective SiO_2 film which largely decreased the oxygen diffusion inward of the bulk material, while the oxidation mechanism of Blend #1 was determined by the kinetics of both amorphous SiO_2 and Ta_2O_5. A denser and thinner oxidized outer layer containing SiO_2 and Ta_2O_5 was found on Blend #1, oxidized at 1200 ^{o}C, indicating a better oxidation resistance than Blend #1. The improved oxidation resistance of Blend #1 benefitted from the crystalized Ta_2O_5 that embedded in the glassy protective layer. With oxidizing temperatures of up to 1500 ^{o}C, the protective outer layer got thicker but more porous, denoting a degraded oxidation resistance. The oxidation mechanism of Blend #1 was controlled by the crystallization of SiO_2 and Ta_2O_5, and the later changed the oxidation mechanism from phase separation to the oxygen solution and diffusion mechanism in the Ta-doped SiO_2 solution.

Chapter 4 investigated the effects of sample thickness, impact energy, temperature and moisture on the material properties of TaC and/or CNTs reinforced SiC CMCs using P-SHPB. The results showed that thicker specimens and a higher impact energy (higher strain rate loading) tended to promote brittle behavior of the material as characterized by increased ultimate stress and a compressive modulus. Strain rate was inversely proportional to specimen thickness, but positively dependent on impact energy. The energy absorption was found to be consistently increased with sample thickness and impact energy. The decreased particle velocity for thicker specimens was probably due to the hardening and embrittlement effect that slowed the particle motion, while the increased particle velocity with increased impact energy was because of the greater load on the specimen that, in turn, caused greater vibration and propagation of the particles. The results also highlighted that increased temperature and moisture content degraded the mechanical properties of the ceramic composites. The maximum reduction of ultimate stress

due to the increase of temperature from 24-500 ^{o}C was about 9.8%, while the maximum ultimate strain increment in this range was 8.1%. A severe degradation of the materials' strength was found from 400-500 ^{o}C. A negligible difference was found for the two blends of dry samples, but the maximum degradations of failure strength for Blend #1 and Blend #2 at the equilibrium water content were approximately 9.2% and 6.9%, with the corresponding failure strain increments of 7.9% and 5.8%. Both the strain rate and energy absorption were increased with temperature and water content. In the hostile environment, microcracks developed in the matrix due to thermoelastic residual stress or water penetration, which would lower the energy absorption needed to initiate and propagate the damage. The particle velocity was slightly increased with temperature while it remained stable for the wet specimens. Highly cracked patterns radiating from the impact point were observed and the equivalent fragment size was between 6.19 mm to 9.10 mm in the strain rate range of 168-312 1/s, and generally decreased with the increase of strain rate.

In Chapter 5, the dynamic fracture toughness of TaC/CNTs/SiC CMCs as a function of loading rate was investigated by the modified SHPB apparatus, based on the quasi-static fracture toughness ASTM C1421-10 three-point bending standard for advanced ceramic materials. An annealed copper pulse shaper was successfully applied to SHPB to achieve the dynamic equilibrium and constant loading rate, which enabled to relate the fracture toughness at the crack tip to the far-field peaking loading through quasi-static equation. The dynamic fracture toughness for SiC composites was 4.71-8.36 MPa·m$^{1/2}$, which was higher than the quasi-static toughness of 3.88 MPa·m$^{1/2}$. Variation of strain rate revealed that peak energy absorbed by the system to initiate the crack generally increased linearly with increased strain rates, while peak loading force increased nonlinearly with increased strain rates, as did the fracture toughness. It was found

that the SiC composites exhibited a more strain rate dependent property for higher strain rates. At a higher strain rate, or as more energy was transferred to the system, more energy was absorbed in the crack tip to initiate the crack, but the propagation time for the small cracks to initial the fracture may be the same. Fracture toughening mechanisms of CNTs deflection and CNTs bridging were directly observed by SEM. Through the interaction between cracks and the CNTs/matrix interface, perpendicular cracks deflected along the interface, or CNTs bridged the crack, restraining the crack from opening and growing further under the indentation load.

Chapter 6 served as a fundamental work for future directions. Wave propagation in SHPB was investigated by ABAQUS in this chapter, which validated the feasibility of the simplified SHPB model. Features of dynamic response on the composite plate, such as strain rate, energy absorption, and stress-strain relations, were captured by the FE analysis. Failure initiation and the progressive damage model accounting for stiffness degradation due to damage was incorporated in the user-defined subroutine VUMAT in ABAQUS/explicit. The numerical results generally showed good consistency with the experimental ones. The differences probably resulted from the ideal initial stress pulse, perfect boundary conditions, and the exact materials' properties in the numerical simulation.

7.2   FUTURE WORK

As stated above, Chapter 6 successfully validated the wave propagation in SHPB and predicted the damage evolution in the laminated composites by implementing the Hashin failure constitutive model within ABAQUS/Explicit through the user-defined materials subroutine VUMAT. Directions for future work following the numerical simulation of dynamic response for

TaC/CNTs/SiC CMCs under P-SHPB can be divided into two sections. In the first section, work regarding the extension of the FE model from SHPB to P-SHPB will be considered. In the second section, efforts will be made toward the development of an appropriate material model for the TaC/CNTs/SiC system to capture the crack initiation and propagation.

Compared with the conventional SHPB, the P-SHPB consists of an extra penetrator and specimen holder, which are mounted at the end of the incident bar and transmitted bar correspondingly. Thus, instead of being sandwiched between the incident bar and the transmitted bar, the specimen is placed in the holder and in contact with the penetrator before impact with the striker bar. By introducing the penetrator and specimen holder, more contact surfaces are imported: incident bar/penetrator contact pair, penetrator/specimen contact pair, specimen/holder contact pair, and holder/transmitted bar contact pair. In this case, a portion of the stress waves are reflected from the incident bar/penetrator and holder/transmitted bar boundaries, which will have an influence on the characteristics of the captured waves and of course make the simulation more complicated. Parametrical studies will be conducted on the optimization of penetrator geometry and specimen geometry enabling more accurate high strain rate properties for the composites.

Appropriate constitutive models are essential for the accurate simulation of materials under high strain rate loading conditions. As for ceramic materials, the most noteworthy models are the Johnson-Holmquist-Beissel (JHB) model [249], the Johnson-Holmquis (JH-2) model [250], and the combined model of the Drucker-Prager plasticity model [251]. Each of these models contains the same three basic elements which account for the crack initiation and propagation: (1) an equation of state (EOS) for the pressure-volume relation that includes the nonlinear effects of compaction, (2) a representation of the deviatoric strength of the intact and

136

fractured material in the form of a pressure-dependent yield surface, and (3) a damage model that transitions the material from the intact state to the fractured state. The constitutive model will be implemented within ABAQUS through a dynamic user-defined material model VUMAT. Experiments will be conducted to determine the appropriate material constants for the proposed model.

BIBLIOGRAPHY

[1] Z. Gurdal, R. T. Haftka, P. Hajela, Design and optimization of laminated composite materials. *John Wiley & Sons*, New York, 1999.

[2] Z. G. Yang. High energy milling of silicon and graphite mixtures and synthesis of nanostructured – Si_3N_4/SiC composites. *Ph.D Dissertation*, 1998.

[3] R. Smyth. The use of high temperature heat exchangers to increase power plant thermal efficiency Article No. 97089. *Energy Convers. Eng. Conf*. 1690-1695, 1997.

[4] E. Wuchina, E. Opila, M. Opeka, et al. UHTCs: Ultra-high temperature ceramic materials for extreme environment applications. *Electrochem. Soc. Interface*. 30-36, 2007.

[5] S. R. Bakshi, V. Musaramthota. D. A. Virzi, et al. Spark plasma sintered tantalum carbide-carbon nanotube composite: Effect of pressure, carbon nanotube length and dispersion technique on microstructure and mechanical properties. *Mater. Sci. Eng. A*. 528, 2538-2547, 2011.

[6] Z. Meng, G. Sun, M. Li, et al. The strengthening effect of Tantalum in Nickel-Based superalloys. *Proc. Int. Symp. Super*. 563-572, 1984.

[7] C. Booth-Morrison, R. D. Noebe, D. N. Seidman. Effects of a tantalum addition on the morphological and compositional evolution of a model Ni-Al-Cr superalloy. *Proceedings of the International Symposium on Superalloys*. 73-79, 2008.

[8] F. Peng and R. F. Speyer. Oxidation resistance of fully dense ZrB2 with SiC, TaB2, and TaSi2 additive. *J. Am, Ceram. Soc*. 91(5), 1489-1494, 2008.

[9] A. Sommers, Q. Wang, C. T. Joen, et al. Ceramics and ceramic matrix composites for heat exchangers in advanced thermal systems – A review. *Appl. Therm. Eng*. 30(11-12), 1277-1291, 2010.

[10] S. Iijima. Helical microtubules of graphitic carbon. *Nat*. 354, 56-58, 1991.

[11] L. Dai, A. W. H. Mau. Controlled synthesis and modification of carbon nanotubes and C$_{60}$: Carbon nanostructures for advanced polymeric composite materials. *Adv. Mater.* 13, 899-913, 2001.

[12] P. Hvizdos, V. Puchy, A. Duszova, et al. Carbon nanofibers reinforced ceramic matrix composites, nanofibers – production, properties and functional applications. *Dr. Tong Lin (Ed.), ISBN: 978-953-307-420-7,* InTech. 2011.

[13] K. T. Lau, D. Hui. The revolutionary creation of new advanced materials-carbon nanotube composites. *Compos. B Eng.* 33 (4), 263-277, 2002.

[14] E. T. Thostenson, Z. F. Ren, T. W. Chou. Advances in the science and technology of carbon nanotubes and their composites: A review. *Compos. Sci. Technol.* 61(13), 1899-1912, 2011.

[15] M. Shaffer, I. A. Kinloch. Prospects for nanotube and nanofibre composites. *Compos. Sci. Technol.* 64 (15), 2281-2282, 2004.

[16] J. N. Coleman, U. Khan, W. J. Blau, et al. Small but strong: A review of the mechanical properties of carbon nanotube-polymer composites. *Carbon.* 44(9), 1624-1652, 2006.

[17] Cs. Balazsi, Z. Konya, F. Weber, et al. Preparation and characterization of carbon nanotube reinforced silicon nitride composites. *Mater. Sci. Eng. C.* 23(6-8), 1133-1137, 2003.

[18] E. Flahaut, A. Peigney, Ch. Laurent, et al. Carbon Nanotube-metal-oxide nanocomposites: microstructure, electrical conductivity and mechanical properties. *Acta. Mater.* 48, 3803-12, 2000.

[19] Z. Shen, Z. Zhao, H. Peng, et al. Formation of tough interlocking microstructures in silicon nitride ceramics by dynamic ripening. *Nat.* 417, 266-269, 2002.

[20] M. Nygren, Z. Shen. On the preparation of bio-, nano- and structural ceramics and composites by spark plasma sintering. *Solid State Sci.* 5, 125-131, 2003.

[21] Z. Shen, H. Peng, J. Liu, et al. Conversion from nano- to micron-sized structures: experimental observations. *J. Eur. Ceram. Soc.* 24, 3447-3452, 2004.

[22] R. S. Dobedoe, G. D. West, M. H. Lewis. Spark plasma sintering of ceramics. *Bull. ECerS.* 1, 19-24, 2003.

[23] E. Grossman, I. Gouxman, R. Verker. Debris/micrometeoroid impacts and synergistic effects on spacecraft matrials. *MRS Bull.* 35, 41-47, 2010.

[24] W. J. Carter, S. P. Marsh. Hugoniot equation of state of polymer. *Report No. LA-13006-MS* (Los Alamos National Laboratory), 1995.

[25] K. J. Hemker, M. W. Chen, J. W. McCauley. Shock-induced localized amorphization in boron carbide. *Sci*. 299, 1563-1566, 2003.

[26] S. J. Lundin, R. B. Mueller. Advanced aircraft materials, engine debris penetration testing. *Report No. DOT/FAA/AR-03/37* (US Department of Transportation), 2005.

[27] E. L. Thomas. Opportunities in protection materials science and technology for future Army applications. *Report No. Natl Res*. (Council Report), 2011.

[28] N. Gupta and K. Cho. Symposium preview: high strain rate behavior of composites and heterogeneous materials. *JOM*. 62(3), 25-26, 2010.

[29] P. K. Dutta, D. Hui, M. R. Altamirano. Energy absorption of graphite/epoxy plates using Hopkinson bar impact. *U.S. Army Corps of Engineers*. 1991.

[30] E. J. Opila and R. E. Hann. Paralinear oxidation of CVD SiC in water vapor. *J. Am. Ceram. Soc*. 80, 197-205, 1997.

[31] S. Dutta. Fracture toughness and reliability in high-temperature structural ceramics and composites: Prospects and challenges for the 21st century. *Bull. Mater. Sci*. 24(2), 117-120, 2001.

[32] T. Hungria, J. Galy, A. Castro. Spark plasma sintering as a useful technique to the nanostructuration of piezo-ferroelectric materials. *Adv. Eng. Mater*. 11(8), 615-631, 2009.

[33] L. Lopez-de-la-Terro, B. Winkler, J. Schreuer, et al. Elastic properties of tantalum carbide (TaC). *Solid State Communic*. 134, 245-250, 2005.

[34] S. C. Zhang, G. E. Hilmas, W. G. Fahrenholtz. Pressureless densification of zirconium diboride with boron carbide additions. *J. Am. Ceram. Soc*. 89, 1544-1550, 2006.

[35] X. Zhang, G. E. Hilmas, W. G. Fahrenholtz. Synthesis, densification, and mechanical properties of TaB$_2$. *Mater. Lett*. 62(27), 4251-4253, 2008.

[36] I. G. Talmy, J. A. Zaykoski, M. M. Opeka. Synthesis, processing and properties of TaC-TaB2-C ceramics. *J. Eur. Ceram. Soc*. 30(11), 2253-2263, 2010.

[37] J. Yin, J. Chen, X. Liu, et al. Co-dispersion behavior of ZrB$_2$-SiC-B$_4$C-C powders with polyethyleneimine. *Mater*. 6, 4249-4258, 2013.

[38] K-S Cho, Z. A. Munir, H-K Lee. Microstructure of spark plasma sintered silicon carbide with Al-B-C. *J. Ceram. Processing Research*. 9(5), 500-505, 2008.

[39] K. Balani, S. R. Bakshi, D. Lahiri, et al. Grain growth behavior of Aluminum oxide reinforced with carbon nanotube during plasma spraying and postspray consolidation. *Int. J. Appl. Technol.* 7(6), 846-855, 2010.

[40] M. Mazaheri, D. Mari, Z. R. Hesabi, et al. Multi-walled carbon nanotube/nanostructured zirconia composites: Outstanding mechanical properties in a wide range of temperature. *Compos. Sci. Technol*. 71(7), 939-945, 2011.

[41] G-D Zhan, J. D. Kuntz, J. Wan, et al. Single-wall carbon nanotubes as attractive toughening agents in alumina-based nanocomposites. *Nat. Mater*. 2, 38-42, 2003.

[42] G-D Zhan, J. D. Kuntz, J. E. Garay, et al. Electrical properties of nanoceramics reinforced with ropes of single-walled carbon nanobubes. *Appl. Phys. Lett*. 83(6), 1228-1230, 2003.

[43] G-D Zhan, J. D. Kuntz, A. K. Mukherjee, et al. Thermoelectric properties of carbon nanotube/ceramic nanocomposites. *Scripta Mater*. 54, 77-82, 2006.

[44] J. Sun, L. Gao, W. Li. Colloidal processing of carbon nanotube/Alumina composites. *Chem. Mater*. 14(12), 5169-5172. 2002

[45] Cs. Balazsi, Z. Shen, Z. Konya, et al. Processing of carbon nanotube reinforced silicon nitride composites by spark plasma sintering. *Compos. Sci. Technol*. 65(5), 727-733, 2005.

[46] G. B. Yadhukulakrishnan, A. Rahman, S. Karumri, et al. Spark plasma sintering of silicon carbide and multi-walled carbon nanotube reinforced zirconium diboride ceramic composite. *Mater. Sci. Eng. A*. 552, 125-133, 2012.

[47] Z. Shen, M. Johnsson, Z. Zhao, et al. Spark plasma sintering of Alumina. *J. Am. Ceram. Soc*. 85(8), 1921-1927, 2002.

[48] Y. Kodera, N. Toyofuku, H. Yamasaki, et al. Consolidation of SiC/BN composite through MA-SPS method. *J. Mater. Sci*. 43, 6422-6428, 2008.

[49] A. Lara, R. Poyato, A. Munoz, et al. Spark plasma sintering and microstructural characterization of additive-free polycrystalline β-SiC. *Key Eng. Mater*. 423, 67-72, 2010.

[50] F. Lomello, G. Bonnefont, Y. Leconte, et al. Processing of nano-SiC ceramics: Densification by SPS and mechanical characterization. *J. Eur. Ceram. Soc*. 32(3), 633-641, 2012.

[51] Y. Shinoda, Y. Suzuki, K. Yoshida. TEM analysis of nanocrystalline SiC ceramics sintered by SPS using Al_2O_3-TiO_2 additive. *J. Asian Ceram. Soc*. 1(3), 267-273, 2013.

[52] C. M. V. Bolivar, A. Antonini, S. Biamino, et al. Oxidation resistance of multilayer SiC for space vehicle thermal protection systems. *Adv. Eng. Mater*. 12(7), 617-622, 2010.

[53] W. Yang, Z. Shi, H. Li, et al. Improvement of strength and oxidation resistance for SiC/graphite composites by SiC coating. *IOP Conf. Ser.: Mater. Sci. Eng*. 18(2), 1-4, 2011.

[54] X. Yao, Y. Zhang, J. Ren, et al. A SiC/ZrB$_2$-SiC/SiC oxidation resistance multilayer coating for carbon/carbon composites. *Corrosion Sci*. 57, 148-153, 2012.

[55] A. Rezaie, W. G. Fahrenholtz, G. E. Hilmas. Evolution of structure during the oxidation of Zirconium Diboride Carbide in air up to 1500°C. *J. Eur. Ceram. Soc*. 27, 2495-2501, 2007.

[56] S. J. Lee, S. S. Baek, E. S. Kang, et al. Fabrication and oxidation behavior of reactively hot presses TaB$_2$-SiC ceramics. *Surf. Rev. Lett.* 17, 215-221, 2010.

[57] D. Lahiri, E. Khaleghi, S. R. Bakshi, et al., Graphene-induced strengthening in spark plasma sintered tantalum carbide-nanotube composite. *Scripta Mater*. 68, 285-288, 2013.

[58] U. U. Gomes, J. F. da Silva Jr. and G. B. P. Ferreira. Effect of the additives of nanosized Nb and Ta carbides on microstructure and properties of sintered stainless steel, sintering - methods and products, *Dr. Volodymyr Shatokha (Ed.), ISBN: 978-953-51-0371-4,* InTech. 2010

[59] G. Li, X. Xiong, K. Huang. Ablation mechanism of TaC coating fabricated by chemical vapor deposition on carbon-carbon composites. *Trans. Nonferrous Met. Soc. China*. 19, 689-695, 2009.

[60] Y. Yang, H. Yin, B. Liu, et al. Effect of addition of TaC on properties of Ti$_3$SiC2 ceramics. *J. Aeronautical mater*. 33(1), 56-60, 2013.

[61] G. Li, X. Xiong, B. Hang, et al. Structural characteristics and formation mechanisms of crack-free multilayer TaC/SiC coating on carbon-carbon composites. *Trans. Nonferrous Met. Soc. China.* 18, 255-261, 2008.

[62] E. Opila, S. Levine, J. Lorinca. Oxidation of ZrB$_2$-and HfB$_2$-based ultra-high temperature ceramics: Effects of Ta additions. *J. Mater. Sci*. 39, 5969-6001, 2004.

[63] Y. Wang, B. Ma, L. Li, et al. Oxidation behavior of ZrB$_2$-SiC-TaC ceramics. *J. Am. Ceram. Soc.* 95 (1), 374-378, 2012.

[64] M. O. W. Richardson, M. J. Wisheart. Review of low-velocity impact properties of composite materials. *Compos. Part A*. 27, 1123-1131, 1996.

[65] K. T. Ramesh. Springer handbook of experimental solid mechanics. *Edited by William N. Sharpe, Jr.* Willam I. Sharpe. 2008

[66] J. A. Zukas. Impact dynamics. *John Wiley & Sons*, New York, 1982.

[67] H. M. Wen. Penetration of thick FRP laminates. *Compos. Sci. Technol*. 61, 1163-1172, 2001.

[68] S. A. Hitchen, R. M. J. Kemp. The effect of stacking sequence on impact damage in a carbon fibre/epoxy composite. *Compos*. 26(3), 207-220, 1995.

[69] M. A. Will, T. Franz, G. N. Nurick. The effect of laminate stacking sequence of CFRP filament would tubes subjected to projectile impact. *Compos. Struct*. 58, 259-270, 2002.

[70] E. P. Gellert, S. J. Cimpoeru, R. L. Woodward. A study of the effect of target thickness on the ballistic perforation of glass-fibre-reinforced plastic composites. *Int. J. Impact Eng*. 24, 445-456, 2000.

[71] T. Borvik, O. S. Hopperstad, M. Langseth, et al. Effect of target thickness in blunt projectile penetration of weldox 460 E steel plates. *Int. J. Impact Eng*. 28(4), 413-464, 2003.

[72] D. L. Orphal, C. E. Anderson Jr. The dependence of penetration velocity on impact velocity. *Int. J of Impact Eng*. 33(1-12), 546-554, 2006.

[73] E. Charles, T. Behner, T. J. Holmquist, et al. Penetration response of silicon carbide as a function of impact velocity. *Int. J of Impact Eng*. 38(11), 892-899, 2011.

[74] J. Fan, Z. Guan, W. J. Cantwell. Modeling perforation in glass fiber reinforced composites subjected to low velocity impact loading. *Polym. Compos*. 32(9), 1380-1388, 2011

[75] S. N. Wosu, D. Hui, L. Daniel. Hygrothermal effects on the dynamic compressive properties of graphite/epoxy composite material. *Compos.: Part B*. 43, 841-855, 2012.

[76] J. Lankford. The effect of hydrostatic pressure and loading rate on compressive failure of fiber-reinforced ceramic-matrix composites. *Compos. Sci. Technol*. 51(4), 537-543, 1994.

[77] V. Hohler, K. Weber, R. Tham, et al. Comparative analysis of oblique impact on ceramic composite systems. *Int. J of Impact Eng*. 26(1-10), 333-344, 2001.

[78] M. M. Shokrieh, G. H. Javadpour. Penetration analysis of a projectile in ceramic composite armor. *Compos. Struct*. 82(2), 296-276, 2008.

[79] M. Grujicic, B. Pandurangan, D. C. Angstadt, et al. Ballistic-performance optimization of a hybrid carbon-nanotube/E-glass reinforced poly-vinyl-ester-epoxy-matrix composite armor. *J. Mater. Sci*, 42, 5347-5384, 2007.

[80] M. Grujicic, W. C. Bell, L. L. Thompson, et al. Ballistic-protection performance of carbon-nanotube-doped poly-vinyl-ester-epoxy-matrix composite armor reinforced with E-glass fiber mats. *Mater. Sci. Eng. A*. 479, 10-22, 2008

[81] M. A. Makeev, S. Sundaresh, D. Srivastava. Shock-wave propagation through pristine a-SiC and carbon-nanotube-reinforced a-SiC matrix composites. *J. Appl. Phys.* 106(1), 014311, 2009.

[82] A. Morka, B. Jackowska. Ballistic resistance of the carbon nanotube fibres reinforced composites–Numerical study. *Comput. Mater. Sci.* 50(4), 1244-1249, 2010.

[83] L. Coppola, E. Cadoni, D. Forni, et al. Mechanical characterization of cement composites reinforced with fiberglass, carbon nanotubes or glass reinforced plastic (GRP) at high strain rates. *Appl. Mech. Mater.* 82, 190-195, 2011.

[84] K. S. Pandya, K. Akella, M. Joshi, et al. Ballistic impact behavior of carbon nanotube and nanosilica dispersed resin and composites. *J. App. Phy.* 112, 113522, 2012.

[85] L. R. Deobald, A. S. Kobayashi. A bar impact tester for dynamic fracture testing of ceramics and ceramic composites. *SEM Spring Conf. Exp. Mech.* Las Vegas, June 8-11, 1992.

[86] S. Laurenzi, R. Pastore, G. Giannini, et al. Experimental study of impact resistance in multi-walled carbon nanotube reinforced epoxy. *Compos. Struct.* 99, 62-68, 2013.

[87] Z. Wang, J. Xu, P. Qiao. Nonlinear low-velocity impact analysis of temperature-dependent nanotube-reinforced composite plates. *Compos. Struct.* 108, 423-434, 2014.

[88] R. S. Lee, H. J. Kim, J. E. Fischer, et al. Conductivity enhancement in single-walled carbon nanotube bundles doped with K and Br. *Nat.* 388, 255-257, 1997.

[89] S. Bi, G. Hou, X. Su, et al. Mechanical properties and oxidation resistance of α-alumina/multi-walled carbon nanotube composite ceramics. *Mater. Sci. Eng. A.* 528, 1596-1601, 2011.

[90] R. Z. Ma, J. Wu, B. Q. Wei, et al. Processing and properties of carbon nanotubes-nano-SiC ceramic. *J. Mater. Sci.* 33, 5243-5246, 1998.

[91] D. Jiang, J. Zhang, Z. Lv. Multi-wall carbon nanotubes (MWCNTs)-SiC composites by laminated technology. *J. Eur. Ceram. Soc.* 32(7), 1419-1425, 2012.

[92] S. Chang, R. H. Doremus, P. M. Ajayan, et al. Processing and mechanical properties of C-nanotube reinforced alumina composites. *Ceram. Eng. Sci. Proc.* 21(3), 653-658, 2000.

[93] K. G. Dassios. A review of the pull-out mechanism in the fracture of brittle-matrix fibre-reinforced composites. *Adv. Compos. Lett.* 16(1), 17-24, 2007.

[94] X. Wang, N. P. Padture, H. Tanaka. Contact damage resistant ceramic/single-wall carbon nanotubes and ceramic/graphite composites. *Nat. Mater.* 3, 539-544, 2004.

[95] J. Fan, D. Zhao, M. Wu, et al. Preparation and microstructure of multi-wall carbon nanotubes-toughened Al_2O_3 composite. *J. Am. Ceram. Soc*. 89(2), 750-753, 2006.

[96] G. Yamamoto, M. Omori, H. Kimura. A novel structure for carbon nanotube reinforced alumina composites with improved mechanical properties. *Nanotechnol*. 19(31), 315708, 2008.

[97] E. Flahaut, A. Peigney, Ch. Laurent, et al. Carbon nanotube-metal-oxide composites: microstructure, electrical conductivity and mechanical properties. *Acta Mater*. 48(14), 3803-3814. 2000.

[98] G. Yamamoto, M. Omori, K. Yokomizo, et al. Structural characterization and frictional properties of carbon nanotube/alumina composites prepared by precursor method. *Mater. Sci. Eng. B*. 148(1-3), 265-273, 2008.

[99] A. Peigney, F. L. Garcia, C. Estounes, et al. Toughening and hardening in double-walled carbon nanotube/nanostructured magnesia composites. *Carbon*. 48(7), 1952-1960, 2010.

[100] Z. Xia, L. Riester, W. A. Curtin, et al. Direct observation of toughening mechanisms in carbon nanotube ceramic matrix composites. *Acta Mater*. 52, (4), 931-944, 2004.

[101] Z. Xia, W. A. Curtin, B. W. Sheldon. Fracture toughness of highly ordered carbon nanotube/alumina nanocomposites. *J. Eng. Mater. Technol*. 126(3), 238-244, 2004.

[102] Z. Xia, J. Lou, W. A. Curtin. A multiscale experiment on the tribological behavior of aligned carbon nanotube/ceramic composites. *Scripta Mater*. 58, (3), 233-226, 2008.

[103] Z. Gu, Y. Yang, K. Li, et al. Aligned carbon nanotube-reinforced silicon carbide composites produced by chemical vapor infiltration. *Carbon*. 49, 2475-2482, 2011.

[104] S. Abrate. Modelling of impact on composite structures. *Compos. Struct*. 51, 129-166, 2001.

[105] R. Olsson. Analytical prediction of large mass impact damage in composite laminates. *Compos. Part A: Appl. Sci. Manufact*. 32, 1207-1221, 2001.

[106] R. Olsson, M. V. Donadon, B. G. Falzon. Delamination threshold load for dynamic impact on plates. *Int. J. Solids Struct*. 43, 3124-3164, 2006.

[107] M. V. Donadon, L. Lannucci, B. G. Falzon, et al. A progressive failure model for composite laminates subjected to low velocity impact damage. *Comput. Struct*. 86, 1232-1252, 2008.

[108] M. Nguyen, D. Elder, J. Bayandor, et al. A review of explicit finite element software for composite impact analysis. *J. Compos. Mater*. 39(4), 375-386, 2005.

[109] F. K. Chang, K. Y. Chang. A progressive damage model for laminated composites containing stress concertrations. *J. Compos. Mater*. 21(9), 834-855, 1987.

[110] A. V. Krishnamurty, J. N. Reddy. Compressive failure of laminates and delamination bucking: A review. *Shock Vib. Digest*. 25(3), 3-12, 1993.

[111] E. J. Barbero, P. Lonetti. An inelastic damage model for fiber reinforced laminates. *J. Compos. Mater.* 36(8), 941-962, 2002.

[112] S. W. Tsai, E. W. Wu. A general theory of strength for composite anisotropic materials. *J. Compos. Mater*. 5, 58-80, 1971.

[113] Z. Hashin. Failure criteria for unidirectional fiber composites. *ASME J. Appl. Mech*. 47(2), 329-334, 1980.

[114] S. P. Engelstad, J. N. Eddy, N. F. Night. Postbuckling response and failure prediction of graphite-epoxy plates loaded in compression. *AIAA J.* 30(8), 2106-2113, 1992.

[115] S. B. Singh, A. Kumar, N. G. R. Lyengar. Progressive failure of symmetrically laminated plates under uni-axial compression. *Struct. Eng. Mech*. 5(4), 433-450, 1997.

[116] N. F. Knight Jr., C. C. Rankin, F. A. Brogan. STAGS computational procedure for progressive failure analysis of laminated composite structures. *Int. J of Non-Linear Mech*. 37(4-5), 833-849, 2002.

[117] R. Talreja. Modeling of damage development in composites using internal variable concepts. Damage Mechanics in Composites. *ASME AD*. 12, 11-16, 1987.

[118] P. Ladeveze, E. Le. Dantec. Damage modeling of the elementary ply for laminated composites. *Compos. Sci. Technol*. 43, 257-267, 1992.

[119] A. F. Johnson. Modelling of fabric reinforced composites under impact loads. *Compos*. 32, 1197-1206, 2001.

[120] K. V. Williams, R. Vaziri, A. Poursartip. A physically based continunm damage mechanics model for thin laminated composite structures. *Int. J. Solids Struct*. 40, 2267-2300, 2003.

[121] L. Iannucci. Progressive failure modeling of woven carbon composite under impact. *Int. J. Impact Eng.* 32(6), 1013-1043, 2006.

[122] L. Iannucci, J. Ankersen. An energy based damage model for thin laminated composites. *Compos. Sci. Technol*. 66, 934-951, 2006.

[123] S. A. Silling. Reformulation of elasticity theory for discontinuities and long-range forces. *J. Mech. Phys. Solids*. 48(1), 175-209, 2000.

[124] E. Askari, J. Xu, S. Silling. Peridynamic analysis of damage and failure in composites. *In 44th AIAA Aerospace Science Meeting and Exhibit, Reno, Nevada, number AIAA*. 2006.

[125] J. Xu, A. Askari, O. Weckner, et al. Peridynamic analysis of impact damage in composite laminates. *J. Aerospace Eng*. 21, 187-194, 2008.

[126] E. Askari, K. Nelson, O. Weckner, et al. The design of a hybrid materials for multifunctional performance using advanced analysis techniques and testing. *In Proc. 40th ISTC, Memphis, Tennessee, USA. Soc. Adv. Mater. Proc. Eng*. 2008.

[127] G. Fantozzi, J. Chevalier, C. Olagnon, et al. Creep of ceramic matrix composites. *Compr. compos. Mater. Oxford: Pergamon*. 115-162, 2000.

[128] M. Mazaheri, D. Mari, Z. R. Hesabi, et al. Multi-walled carbon nanotube/nanostructured zirconia composites: Outstanding mechanical properties in a wide range of temperature. *Compos. Sci. Technol.* 71(7), 939-945, 2011.

[129] R. Schaller, A. Lakki. Grain boundary relaxations in ceramics. *Mater. Sci. Forum.* 366-368, 315-337, 2001.

[130] S. Rul, F. Lefevre-schlick, E. Capria, et al. Percolation of single-walled carbon nanotubes in ceramic matrix nanocomposites. *Acta Mater.* 52(4), 1061-1067, 2004.

[131] A. Peigney, Ch. Laurent, E. Flahaut, et al. Carbon nanotubes in novel ceramic matrix nanocomposites. *Ceram. Int.* 26(6), 667-683, 2000.

[132] E. Flahaut, A. Peigney, Ch. Laurent, et al. Carbon Nanotube-metal-oxide nanocomposites: microstructure, electr ical conductivity and mechanical properties. *Acta. Mater.* 48, 3803-3812, 2000.

[133] Z. A. Munir, U. A. Tamburini, M. Ohyanagi. The effect of electric field and pressure on the synthesis and consolidation of materials: A review of the spark plasma sintering method. *J. Mater. Sci.* 41, 763-777, 2006.

[134] M. Tokita. Mechanism of spark plasma sintering. *Proceedings of NEDO International Symposium on Functional Graded Materials, Tokyo, Japan*. 23-33, 1999.

[135] J. E. Garay. Current-activated, pressure-assisted densification of materials. *Annu. Rev. Mater. Res*. 40, 445-468, 2010.

[136] S. Prochazka. The role of Boron and Carbon in sintering of Silicon Carbide. *Special Ceramics, 6, Edited by P. Popper, The British Ceramic Research Association, Stroke-on Trent*, UK, 171-181, 1975.

[137] H. Hausner. Energy and ceramics. *Mater. Sci. Monographs, 6, Edited by Vincenzini, Elsevier Scientific Publ. Co., Amsterdam*. 582, 1980.

[138] X. Zhang, G. E. Hilmas, W. G. Fahrenholts, et al. Hot pressing of tantalum carbide with and without sintering additives. *J. Am. Ceram. Soc*. 90(2), 393-401, 2007.

[139] D. Sciti, L. Silvestroni, S. Guicciardi, et al. Processing, mechanical properties and oxidation behavior of TaC and HfC composites containing 15 vol% $TaSi_2$ or $MoSi_2$. *J. Mater. Res*. 26(6), 2056-2065, 2009.

[140] C. X. Liu, J. W. Choi. Improved dispersion of carbon nanotubes in polymers at high concentrations. *Nanomater*. 2, 329-347, 2012.

[141] G. T. Caneba, C. Dutta, V. Agrawal, et al. Novel ultrasonic desertion of carbon nanotube. *J. Minerals & Mater. Charact. & Eng*. 9(3), 165-181, 2010.

[142] http://accuratus.com/silicar.html

[143] S. Prochazka. Proceedings of the Conference on Ceramics for High Performance Applications, Hyanuis, MA, 1973. Burke, J.J.; A.E.; Katz, R.M., eds., *Brook Hill Publishing Co.* 7-13, 1975.

[144] W. Guo, J. Vleugels, G. Zhang, et al. Effect of heating rate on densification, microstructure and strength of spark plasma sintered ZrB_2-based ceramics. *Scr. Mater.* 62, 802-805, 2010.

[145] D. Jain, K. M. Reddy, A. Mukhopadhyay, et al. Achieving uniform microstructure and superior mechanical properties in ultrafine grained TiB_2-$TiSi_2$ composites using innovative multi stage spark plasma sintering. *Mater. Sci. Eng. A*. 528, 200-207, 2010.

[146] K. M. Reddy, N. Kumar, B. Basu. Innovative multi-stage spark plasma sintering to obtain strong and tough ultrafine-grained ceramics. *Scr. Mater*. 62, 435-438, 2010.

[147] W. B. Tian, Y. M. Kan, G. J. Zhang, et al. Effect of carbon nanotubes on the properties of ZrB_2-SiC ceramics. *Mater. Sci. Eng. A*. 487, 568-573, 2008.

[148] P. Klimczyk. SiC-based composites sintered with high pressure method. *Silicon Carbide-Materials, Processing and Applications in Electronic Devices. Dr. Moumita Mukherjee (Ed.)*, *ISBN: 978-953-307-968-4*, 2011.

[149] B. Peng, M. Locascio, P. Zapol, et. al. Measurements of near-ultimate strength for multiwalled carbon nanotubes and irradiation-induced crosslinking improvements. *Nat. Nanotechnol*. 3(10), 626-631, 2008.

[150] S. R. Bakshi, A. Bhargava, S. Mohammadizadeh, et al. Computational estimation of elastic properties of spark plasma sintered TaC by meshfree and finite element methods. *Comp. Mater. Sci*. 50, 2615-2620, 2011.

[151] Z. A. Munir, U. A. Tamburini. The effect of electric field and pressure on the synthesis and consolidation of materials: A review of the spark plasma sintering method. *J. Mater. Sci.* 41, 763-777, 2006.

[152] S. C. Liao, W. E. Mayo, K. D. Pae. Theory of high-pressure low-temperature sintering of bulk nanocrystalline TiO_2. *Acta Mater.* 45(10), 4027-4040, 1997.

[153] X. Yao, H. Li, Y. Zhang, et al. A SiC/ZrB_2-SiC/SiC oxidation resistance multilayer coating for carbon/carbon composites. *Corros. Sci.* 57, 148-153, 2012.

[154] V. V. Rudneva, G. V. Galevskii. Investigation of thermal oxidation resistance of nanopowders of refractory carbides and borides. *J. Non-Ferr. Mater.* 48(2), 143-147, 2007.

[155] P. J. Jorgensen, M. E. Wadsworth, I. B. Culter. Oxidation of Silicon Carbide. *J. Am. Ceram. Soc.* 42, 613-616, 1959.

[156] P. J. Jorgensen, M. E. Wadsworth, I. B. Culter. Effects of Oxygen partial pressure on the oxidation of Silicon Carbide. *J. Am. Ceram. Soc.* 43, 209-212, 1960.

[157] M. Balat, R. Berjoan, G. Pichelin, et al. High-temperature oxidation of sintered silicon carbide under pure CO_2 at low pressure: active-passive transition. *Appl. Surf. Sci.* 133(1-2), 115-123, 1998.

[158] G. Ch. Nayak, R. Rajasekar, C. K. Das. Effect of SiC coated MWCNTs on the thermal and mechanical properties of PEI/LCP blend. *Compos. Part A: Appl. Sci. Manuf.* 41 (11), 1662-1667, 2010.

[159] N. Song, H. Liu, Y. Yuan, et al. Fabrication and corrosion resistance of SiC-coated multi-walled carbon nanotubes. *J. Mater. Sci. Technol.* 29 (12), 1146-1150, 2013.

[160] P. Zeman, J. Musil, R. Daniel. High-temperature oxidation resistance of Ta-Si-N films with a high Si content. *Surf. Coat. Technol.* 200, 4091-4096, 2006.

[161] E. J. Opila, M. C. Halbig. Oxidation of ZrB_2-SiC. *Ceram. Eng. Sci. Proc.* 22(3), 221-228, 2001.

[162] E. J. Opila, S. Levine, J. Lorincz. Oxidation of ZrB_2- and HfB_2-based ultra-high temperature ceramic: Effect of Ta additions. *J. Mater. Sci.* 39 (19), 5969-5977, 2004.

[163] A. Nieto, A. Kumar, D. Lahiri, et al. Oxidation behavior of graphene nanoplatelet reinforced tantalum carbide composites in high temperature plasma flow. *Carbon.* 2013.

[164] D. Eder. Carbon nanotube-inorganic hybrids. *Chem. Rev.* 110(3), 1348-1385, 2010.

[165] S. Aksel, D. Eder. Catalytic effect of metal oxides on the oxidation resistance in carbon nanotube-inorganic hybrids. *J. Mater. Chem*. 20, 9149-9154, 2010.

[166] C-W. Lee, I-H. Kim, W Lee, et al. Formation and analysis of SiC coating layer on carbon short fiber. *Surf. Interface Anal*. 42(6-7), 1231-1234, 2010.

[167] I. S. Gorban, G. N. Mishinova. The bases of luminescence diagnostic of dislocation structure of SiC crystals. *SPIE Proc. Ser.* 3359, 187-196, 1997.

[168] I. S. Gorban, G. N. Mishinova, V. I. Vlaskin, et al. 3C-6H transformation in heated cubic silicon carbide 3C-SiC. *Semicond. Phys. Quantum Electron. Optoelectron.* 12(4) 432-436, 2011.

[169] P. Deshmukh, J. Bhatt, D. Peshwe, et al. Determination of silica activity index and XRD, SEM and EDS studies of amorphous SiO_2 extracted from rive husk ash. *Trans. Indian Inst Met.* 65(1), 63-70, 2012.

[170] E. J. Opila, J. Smith, S. R. Levine, et al. Oxidation of $TaSi_2$-containing ZrB_2-SiC ultra-high temperature materials. *J. Open Aero. Eng.* 3, 41-51, 2010.

[171] L. Bokobza, J. Zhang. Raman spectroscopic characterization of multiwall carbon nanotubes and of composites. *Exp. Polym. Lett.* 6(7), 601-608, 2012.

[172] M. S. Dresselhaus, A. Jorio, M. Hofmann, et al. Perspectives on carbon nanotubes and graphene raman spectroscopy. *Nano Lett.* 10(3), 751-758, 2010.

[173] X. Wang, N. P. Padture, H. Tanaka. Contact-damage-resistant ceramic/single-wall carbon nanotubes and ceramic/graphite composites. *Nat. Mater.* 3(8), 539-544, 2004.

[174] P. M. Ajayan, L. S. Schadler, C. Giannaris, et al. Single-walled carbon nanotube-polymer composites: strength and weakness. *Adv. Mater.* 12(10), 750-753, 2000.

[175] E. L. Corral, H. Wang, J. Garay, et al. Effect of single-walled carbon nanotubes on thermal and electrical properties of silicon nitride processed using spark plasma sintering. *J. Eur. Ceram. Soc.* 31(3), 391-400, 2011.

[176] F. Huang, K. T. Yue, P. Tan, et al. Temperature dependence of the Raman spectra of carbon nanotubes. *J. Appl. Phys.* 84, 4022-4024, 1998.

[177] A. C. Ferrari, J. Robertson. Interpretation of Raman spectra of disordered and amorphous carbon. *Phys. Rev. B.* 61(20), 14095-14107, 2000.

[178] K. N. Kudin, B. Ozbas, H. C. Schniepp, et al. Raman spectra of graphite oxide and functionalized graphene sheets. *Nano Lett.* 8(1), 36-41, 2008.

[179] J. M. Benoit, J. P. Buisson, O. Chauvet, et al. Low-frequency Raman studies of multiwalled carbon nanotubes: Experiments and theory. *Phys. Rev. B.* 66, 073417, 2002.

[180] N. S. Jacobson, D. L. Myers. Active oxidation of SiC. *Oxid. Met.* 75, 1-25, 2011.

[181] G. Li, X. Xiong, K. Huang. Ablation mechanism of TaC coating fabricated by chemical vapor deposition on carbon-carbon composites. *Trans. Nonferr. Met. Soc. China.* 19, 689-695, 2009.

[182] P. H. C. Camargo, K. G. Satyanarayana, F. Wypych. Nanocomposites: synthesis, structure, properties and new application opportunities. *Mat. Res.* 12(1), 1516-1439, 2009.

[183] S. S. Samal, S. Bal. Carbon nanotube reinforced ceramic matrix composites—A review. *J. Mineral. Mater. Charact. Eng.* 7(4), 355-370, 2008.

[184] L. P. Zawada, J. Staehler, S. Steel. Consequence of intermittent exposure to moisture and salt fog on the high-temperature fatigue durability of several ceramic-matrix composites. *J. Am. Ceram. Soc.* 86(8), 1282-1291, 2003.

[185] G. Raiser, R. J. Clifton. High strain rate deformation and damage in ceramic materials. *J. Eng. Mater. Technol.* 115(3), 292-299, 1993.

[186] J. Lankford. High strain rate compression and plastic flow of ceramics. J. *Mater. Sci. Lett.* 15, 745-750, 1996.

[187] M. Futakawa, Y. Tanabe, T. Wakui, et al. Dynamic effect on strength in SiC_f/SiC_m composite. *Int. J. Impact Eng.* 25(1), 29-40, 2001.

[188] J. Lankford. The failure of fiber-reinforced ceramic-matrix composites under dynamic loading. *JOM* 47(5), 64-68, 1995.

[189] K. J. Larochelle, S. Mall. Temperature and moisture effects upon stress rupture life of Syl-iBN/BN/Sic composite*, in 27th Annual Cocoa Beach Conf. Adv. Ceram. Compos. B: Ceram. Eng. Sci. Proc. 24(4), 2003. (eds W. M. Kriven and H.-T. Lin), John Wiley & Sons, Inc.,* Hoboken, NJ, USA.

[190] J. J. Brennan. The environmental durability of fiber reinforced ceramic matrix composites. *R94-970439-2, Annual Report.* 1994.

[191] N. S. Jacobson. Corrosion of silicon-based ceramics in combustion environments. *J. Am. Ceram. Soc.* 76(1), 3-28, 1993.

[192] L. Thomas-Ogbuji. A pervasive model of oxidation degradation in a SiC-SiC composite. *J. Am. Ceram. Soc.* 82(11), 2777-2784, 1998.

[193] S. Sarva, S. Nemat-Nasser. Dynamic compressive strength of Silicon Carbide under uniaxial compression. *Mater. Sci. Eng. A*. 317, 140-144, 2001.

[194] J. Landford, W. W. Predebon, J. M. Staehler, et al. The role of plasticity as limiting factor in the compressive failure of high strength ceramics. *Mech. Mater*. 29, 205-218, 1998.

[195] D. Rittel, H. Mairge, H. D. Bui. A new method for dynamic fracture toughness testing. *Scr. Metall. Mater.* 26(10), 1593-1598, 1992.

[196] C. F. Martins, V. Prakash. Dynamic fracture characterization of LMDPE utilizing a modified split Hopkinson Bar. *Proceedings of 2002 Society of Experimental Mechanics Annual Conference,* Milwaukee, WI, 2002.

[197] R. Pati, Y. Zhang, S. K. Nayak, et al. Effect of H_2O adsorption on electron transport in a carbon nanotube. *Appl. Phys. Lett*. 81(14), 2638-2640, 2002.

[198] S. Mall. Effects of moisture on fatigue behavior of SiC/SiC composite at elevated temperature. *Mater. Sci. Eng. A*. 412, 165-170, 2005.

[199] G. N. Morscher, J. Hurst, D. Brewer. Intermediate-temperature stress rupture of a woven Hi-Nichalon, BN-interface, SiC-matrix composite in air. J. Am. *Ceram. Soc*. 83, 1441-1449, 2000.

[200] R. L. Sierakowski. Strain rate effects in composites. *Appl. Mech. Rev*. 50, 741-761, 1997.

[201] J. A. Zukas, T. Nicholas, H. Swift, et al. Impact dynamics. *Kreiger Publishing Co*., 1992.

[202] L. W. Bickle. An introduction of the use of strain gages for the measurement of propagating strain wave. *Sandia Laboratories*, Albuquerque, NM, 1970.

[203] P. K. Dutta, F. Dannis, J. Kalafut. The CRREL hopkinson bar apparatus. *CRREL Report, Hanover*, New Hampshire, 1987.

[204] M. R. Allazadeh, M. K. Itani, S. N. Wosu. Compression of the material characteristics of steel, aluminum, wood and woven graphite epoxy composites in response to high strain rate load. *Adv. Mater. Sci. Appl*. 1, 13-30, 2012.

[205] J. K. Kim, C. Hu, R. Woo, et al. Moisture barrier characteristics of organoclay-epoxy nanocomposites. *Compos. Sci. Technol*. 65, 805-813, 2005.

[206] T. P. Mohan, K. Kanny. Water barrier properties of nanoclay filled sisal fibre reinforced epoxy composites. *Compos. A: Appl. Sci. Manuf.* 42, 385-393, 2011.

[207] T. D. Rossing, D. A. Russell. Laboratory observation of elastic waves in solids. *Am. J. Phys.* 58, 1153-1162, 1990.

[208] A. Blake. Handbook of mechanics, materials, and structures. New York: Wiley, 1985.

[209] L. E. Malvern. Behavior of materials under dynamic loading. *N.J. Huffingtyon, Jr, ed ASME*, NY, 1965.

[210] K. Hiraga, B. Kim, K. Morita, et al. High-strain-rate superplasticity in oxide ceramics. Sci. Technol. *Adv. Mater.* 8, 578-587, 2007.

[211] A. Haque. Effects of moisture and temperature on high strain rate behavior of S2-Glass-Vinyl ester woven composites. *J. Compos. Mater.* 37, 672-647, 2003.

[212] Z. N. Azwa, B. F. Yousif, A. C. Manalo, et al. A review on the degradation of polymeric composites based on natural fibres. *Mater. Des.* 47, 424-442, 2013.

[213] S. Satapathy. Dynamic spherical cavity expansion in brittle ceramics. *Int. J. Solids Struc.* 38, 5833-5845, 2001.

[214] Y. Zhang, Y. Lu, H. Hao. Analysis of fragment size and ejection velocity at high strain rate. *Int. J. Mech. Sci.* 46, 27-34, 2004.

[215] P. Kim, L. Shi, A. Majumdar, et al. Thermal transport measurements of individual multiwalled nanotubes. *Phys. Rev. Lett.* 87, 215502, 2001.

[216] R. H. Baughman, A. A. Zakhidov, W. A. De Heer. Carbon nanotubes-the route toward applications. *Sci.* 297, 787-792, 2002.

[217] J. Lu, Y. H. Jian, H. H. Zhang, et al. Preparation and properties of Lyocell/multi-walled carbon nanotube composite fibers. *New Carbon Mater.* 22, 159-164, 2007.

[218] T. Weerasooriya, P. Moy, D. Cazem, et al. A four-point bend technique to determine dynamic fracture toughness of ceramics. *J. Am. Ceram. Soc.* 89(3), 990-995, 2006.

[219] W. Geary, J. Dutton, D. M. Shuter. The influence of size effects and dynamic loading on the fracture toughness of commercial GRP materials. *Compos. Sci. Technol.* 60(4), 633-638, 2000.

[220] F. Jiang, R. Liu, S. V. Kenneth, et al. Evaluation of dynamic fracture toughness K_{ID} by Hopkinson pressure bar loaded instrumented Charpy impact test. *Eng. Fract. Mech.* 71(3), 279-287, 2004.

[221] S. Samborski, T. Sadowski. Dynamic fracture toughness of porous ceramics. *J. Am. Ceram. Soc.* 93(11), 3607-3609, 2010.

[222] C. Rubio-Gonzalez, J. A. Gallardo-Gonzalez, G. Mesmacque, et al. Dynamic fracture toughness of pre-fatigued materials. *Inter. J. Fatigue.* 30(6), 1056-1064, 2008.

[223] W. A. Cutrin. Stress-strain response of brittle matrix composites. *In: Kelly A, Zweben C. editors. Encyclopedia of Compos. Holland: Elsevier*, 2000.

[224] M. N. Tamin (ed.). Damage and fracture of composite materials and structures, *Adv. Struct. Mater.* 17, 2012.

[225] A. A. Griffith. The phenomena of rupture and flow in solids. *Phil. Trans. R. Soc.* Lond. 221, 163-198, 1920.

[226] G. R. Irwin. Fracture. *Handbuch der Phy VI* (*Flugg Ed.).* Springer, 551-590, 1958.

[227] S. N. Nwosu. High strain rate perforation and mixed mode delamination of laminated composites. *Wright Laboratory, Final Report*, 1997.

[228] W. Bohme, J. F. Kalthoff. The behavior of notched bend specimens in impact testing. *Int. J. Fract.* 20, 139-143, 1982.

[229] ASTM C1372-99. Standard test method for Vickers indentation hardness of advanced ceramic.

[230] G. R. Anstis, P. Chantikul, B. R. Lawn, et al. A critical evaluation of indentation techniques for measuring fracture toughness: I, Direct crack measurements. *J. Am. Soc.* 64, 533-538, 1981.

[231] D. J. Frew, M. J. Forrestal, W. Wen. Pulse-shaping techniques for testing brittle materials with a split Hopkinson pressure bar. *Exp. Mech*. 42(1), 93-106, 2002.

[232] D. J. Frew, M. J. Forrestal, W. Wen. Pulse shaping techniques for testing elastic-plastic materials with a split Hopkinson pressure bar. *Exp. Mech*. 45, 186-195, 2005.

[233] J. F. Knott. Fundamentals of fracture mechanics. London: Butterworth. 1973.

[234] J. Klepaczko. Application of the split Hopkinson pressure bar to the fracture dynamics. *Inst. Phys. Conf. Ser.* 47, 201-214, 1979.

[235] R. G. Munro. Material properties of a sintered Alpha-SiC. *J. Phys. Chem. Ref. Data.* 26, 1195-1203, 1997.

[236] R. F. Cook, G. M. Pharr. Direct observation and analysis of indentation cracking in glasses and ceramics. *J. Am. Soc*. 73(4), 787-817, 1990.

[237] R. L. Sierakowski, C. A. Ross, L. E. Malvern. Studies on the fracture mechanisms in partially penetrated filment reinforced laminated plate. *US army research office, DAAG 29-79-G-0007*. Dec. 1981.

[238] N. Cristercu, L. E. Malvern, R. L. Sierakowski. Failure mechanisms in composite plates impacted by blunt-ended penetrators. *in: Proceedings of the Symposium, Foreign Object Impact Damage to Composites, ASTM STP 568, Am. Soc. Test. Mater.* Philadelphia, PA, 159-172, 1975.

[239] M. R. Allazadeh, S. N. Wosu. High strain rate compressive tests on woven graphite epoxy composites. *Appl. Compos. Mater.* 1(1), 13-30, 2012.

[240] S. N. Wosu, H. David, K. D. Piyush. Dynamic mixed-mode I/II delamination fracture and energy rate of unidirectional graphite/epoxy composites. *Eng. Fract. Mech.* 72, 1531-1558, 2005.

[241] C. R. Siviour. A measurement of wave propagation in the split Hopkinson pressure bar. *Meas. Sci. Technol.* 20, 065702, 2009.

[242] J. R. Vinson, E. Woldesenbet. Fiber orientation effects on high strain rate properties of graphite/epoxy composites. *J. Compos. Mater.* 35(6), 509-521, 2001.

[243] B. P. Patel, S. K. Bhola, M. Ganapathi, et al. Penetration of projectiles in composite laminates. *Defence Sci. J.* 54(2), 151-159, 2004.

[244] B. Gu. Ballistic penetration of conically cylindrical steel projectile into plain-woven fabric target – A finite element simulation. *J. Compos. Mater.* 38(22), 2049-2074, 2004.

[245] M. Nurhaniza, M. K. Ariffin, A. Ali, et al. Finite element analysis of composites materials for aerospace applications. *9th National Symposium on Polymeric Materials, IOP Conf.: Mater. Sci. Eng.* 11, 012010, 2009.

[246] R. M. Jones. *Mechanics of composite materials (2nd Edition).* Taylor and Francis, Philadelphia, 1998.

[247] X. B. Li, T. S. Lok, J. Zhao. Dynamic characteristics of granite subjected to intermediate loading rate. *Rock Mech. Eng.* 38(1), 21-39, 2005.

[248] M. Tarfaoui, S. Choukri, A. Neme. Effect of fibre orientation on mechanical properties of the laminated polymer composites subjected to out-of-plane high strain rate compressive loadings. *Compos. Sci. Technol.* 68(2), 477-484, 2007.

[249] T. Holmquist, G. Johnson. Characterization and evaluation of silicon carbide for high-velocity impact. *J. Appl. Phys.* 97, 1-12, 2005.

[250] G. Johnson, T. Holmquist. An improved computational constitutive model for brittle materials. *AIP Conf. Proc.* 309, 981-984, 1994.

[251] Simulia. *Abaqus Example Problems Manual.* Providence, RI: Dassault Systemes. 2011.